Rodrigo Fedrizzi Dillenburg

Water desalination by MoS2 nanopores: the role of pore geometry and chemistry on water and ion transport.

Dessalinização da água por membranas nanoporosas de MoS2: o papel de geometria e química dos poros no transporte de água e íons

Brasil

2022

Rodrigo Fedrizzi Dillenburg

Water desalination by MoS2 nanopores: the role of pore geometry and chemistry on water and ion transport.

Dessalinização da água por membranas nanoporosas de MoS2: o papel de geometria e química dos poros no transporte de água e íons

Thesis prepared under the supervision of Profa. Marcia Cristina Barbosa, presented to the Physics Graduation Program of the Instituto de Física at UFRGS, in partial fullfillment of the requirements for obtaining the title of Master of Science.

Universidade Federal do Rio Grande do Sul - UFRGS
Instituto de Física
Programa de Pós-Graduação em Física (PPGFís)

Supervisor: Prof. Dra. Marcia Cristina Barbosa

Brasil

2022

Abstract

Water scarcity is a pressing issue faced by humanity and is predicted to worsen in the near future. The development of more cost-effective water desalination technology can help alleviate these issues. 2D materials, made up of atom-thick membranes with nanoscale pores are a promising candidate to new generation desalination membranes. Among the most promising materials is molybdenum dissulfide, or MoS_2. Using molecular dynamics simulations, we are able to elucidate some of the underlying phenomena regulating its performance as a reverse osmosis membrane applied to water desalination. By varying geometric and chemical properties of single layer MoS_2 nanopores we offer a detailed analysis on the mechanisms governing water and ion transport. We show that both the pore's size and its charge distribution, induced by pore chemistry, play significant roles on transport phenomena across the nanopores. We provide an analysis on properties influencing water flux and salt rejection, and how both quantities are related due to water-ion interactions. We then provide an analysis on the mechanism governing water transport across bilayer nanoporous MoS_2 membranes, where hydrated MoS_2 forms a nanochannel between both layers. We study how charge distribution, pore alignment and layer separation impact water transport across such systems and show that it does not obey classical hydrodynamics equations due to the presence of confinement effects. Our results both confirm previous literature and provide new information on the underlying mechanisms governing the efficiency of MoS_2 as a desalination membrane. Next generation membranes must provide high ion selectivity while maintaining high water fluxes, and our results suggest MoS_2 may be a viable candidate for such. We hope that this work will be helpful in the design of such new technologies.

Resumo

Escassez de água potável é um problema que afeta bilhões de pessoas ao redor do mundo e tende a piorar no futuro próximo. O desenvolvimento de tecnologias mais baratas de desalinização da água do mar pode ajudar a aliviar alguns desses desafios. Materiais 2D, compostos de membranas de espessura atômica adornados de poros de tamanho nanométrico são candidatos promissores para a nova geração de membranas de dessalinização. Entre os materiais mais promissores está o dissulfeto de molibdênio, ou MoS_2. Utilizando simulações de dinâmica molecular nós conseguimos elucidar fenômenos que regulam a performance desse material como uma membrana de osmose reversa aplicada à dessalinização da água do mar. Variando a geometria e a química de nanoporos localizados em membranas monocamada de MoS_2 nós oferecemos uma análise detalhada dos mecanismos que regulam o transporte de água e de íons de sal. Nós mostramos como o tamanho do poro e a distribuição de cargas induzida pela sua composição química têm papel crucial em tais fenômenos de transporte através dos nanoporos. Nós fornecemos uma análise das propriedades que determinam o fluxo de água e a rejeição de íons e como essas quantidades estão relacionadas devido a interações água-íons. Finalmente, foi conduzida uma análise dos mecanismos regulando o fluxo de água através de membranas bicamada de MoS_2 contendo nanoporos, onde uma forma hidratada do MoS_2 forma um nanocanal entre ambas camadas da membrana. Nós mostramos como a distribuição de cargas, alinhamento dos poros e distância entre as camadas da membrana influenciam o transporte de moléculas de água através de tais sistemas e mostramos que ele não é regido pelas leis da hidrodinâmica clássica devido à presença de efeitos de confinamento. Nosso trabalho tanto confirma resultados da literatura como fornece novas informações sobre os mecanismos determinantes para a performance de membranas de dessalinização de MoS_2. A próxima geração de membranas de dessalinização deve exibir altas taxas de seletividade iônica e de fluxo de água e os nosso resultados indicam que MoS_2 é um potencial candidato para tal aplicação. Nós esperamos que esse trabalho possa ser útil no desenvolvimento dessas novas tecnologias.

Contents

1 Introduction

Water scarcity is among humanity's biggest challenges, affecting around 2.7 billion people around the world at varying degrees and this number is expected to grow as high as two thirds of the world population by 2025, mostly due to climate change [1]. Figure 1 represents water availability throughout the world. Despite being one of the most abundant substances on Earth's surface, only 0.3% of the global water supply is made up of fresh water easily accessible to humans, while the majority of it, 97%, is made up of saltwater located in Earth's oceans [2]. Water desalination technologies allow humanity to tap into this vast pool of unexploited resources.

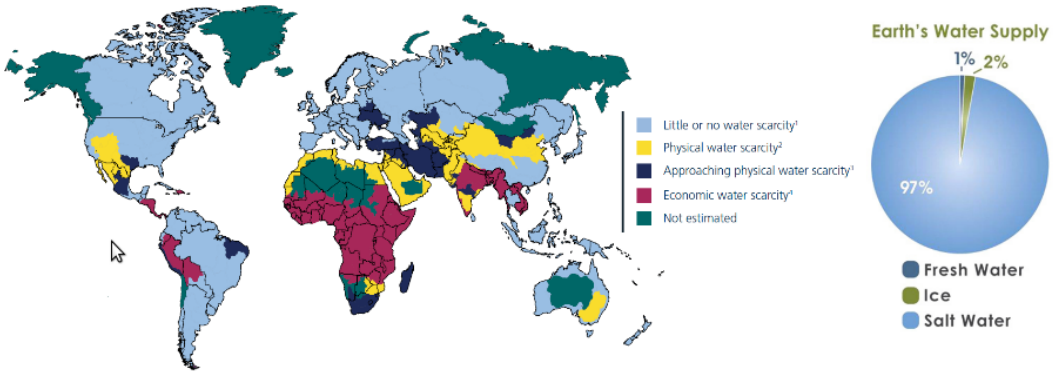

Figure 1: Water scarcity around the world in 2007. [3]

While rudimentary desalination techniques have been reported as far back as the 1600s, the first large scale desalination plant was built in 1928 and it was based on the principle of water distillation, where saltwater is boiled to separate it from salt and then condensates at a separate reservoir producing freshwater. The introduction in the 1960s of the first reverse osmosis (RO) desalination plants brought a great decrease in production costs due to its lower energy consumption [4].

Reverse osmosis remains the most efficient desalination method available today [5] and it is employed in very arid parts of the world to produce freshwater. This technology is based on a membrane separation method and is illustrated in Figure 2. Two reservoirs, one filled with saltwater and the other with freshwater are separated by a semipermeable membrane, which allows for the passage of water but not of salt ions. Due to the difference in concentration on both sides an osmotic pressure arises, causing water to flow from the freshwater reservoir to the saltwater reservoir to balance this difference. However, if a pressure higher than the osmotic pressure is applied to the saltwater side, this process is reversed, making water flow away from the saltwater container into the freshwater one to produce freshwater.

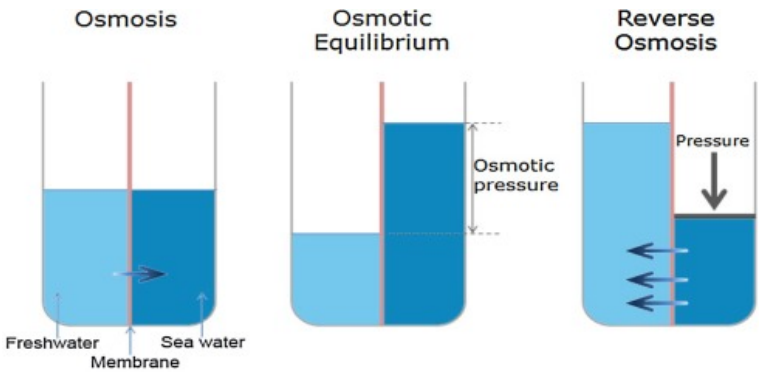

Figure 2: Illustration of the reverse osmosis process. [6]

Reverse osmosis remains, nonetheless, a rather expensive desalination technique, due to its high energy consumption [7]. This prevents it from becoming a widespread source of drinking water to people facing scarcity. In order to make cheap and less resource consuming water desalination available to those who need it the process must be improved.

Current RO membranes are made of thick polymeric materials which allow for the flow of water but reject salt ions. Most membranes in the market today are made of m-phenylenediamine (MPD)

or trimesoyl chloride (TMC) [8]. Due to the high thickness of such membranes, water output is low and it requires high pressures to be applied to the system. Many techniques involving pretreatment of saltwater have been developed to increase efficiency, however, nanoscience can offer a solution that could increase performance by 2-5 orders of magnitude [9, 10].

The first nanostructures that gained a lot of attention in desalination research were carbon nanotubes (CNT). Extensive studies were conducted on it and its possible applications in nanofluidics. The reason for such an interest is the phenomenon of superflux observed in CNTs, in which water flows at speeds up to a thousand times faster than predicted by classical hydrodynamics [11, 12, 13, 14, 15, 16, 17]. This phenomenon arises because water molecules in nanoconfined geometries maximize the number of hydrogen bonds formed, forming organized structures which move, in the case of nanotubes, in a line, as shown in Figures 3(a)-(b). This leads to a near frictionless movements of molecules. The small diameter of the CNTs also makes ion transport very difficult across the tubes as its geometry disturbs the hydration shells, making it a perfect candidate for desalination applications. A few issues may hinder the possible real life applications of CNT based membranes such as it high toxicity [18, 19], the difficulty in fabricating CNTs of diameters small enough to exhibit superflux (< 2nm) [12] and the need for incorporation of the nanotubes into a polymeric matrix which can be a complicated process [20].

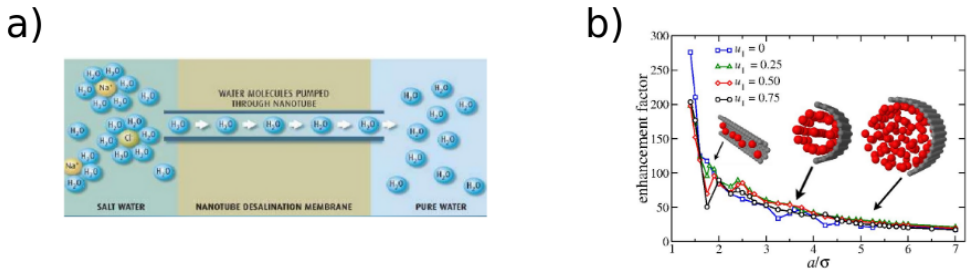

Figure 3: Illustration of superflux and ion exclusion in carbon nanotubes. a) water molecules flowing in a single file inside a CNT [21], b) Enhancement factor of water flow as a function of nanopore diameter [16]

2D materials like graphene have attracted a lot of attention in the past years due to its many uncommon properties, such as extremely high mechanical resistance [22, 23] and electrical mobility [24]. 2D materials such as nanoporous graphene exhibit extremely high values of water permeability compared to thicker commercial polymeric membranes [10, 9]. However, the physical mechanism behind it is still not clear. Its extremely low thickness is likely a main contributing factor. Many works have reported water fluxes of $10 - 10^2 L/cm^2/day/MPa$ for nanoporous graphene while maintaining a salt rejection above 99% [10, 9, 7]. Commercial saltwater desalination membranes currently exhibit water fluxes in the range of $10^{-2} - 10^{-1} L/cm^2/day/MPa$ [25, 7]. Nanoporous graphene-based membranes could, therefore, represent an increase of $10^2 - 10^4$ times in efficiency when compared to current technology.

Another promising candidate for a 2D desalination membrane is molybdenum dissulfide (MoS_2). This material occurs in nature in the form of a mineral called molybdenite, which, just like graphite, is made up of stacked 2D sheets of MoS_2 [26]. Each of these layers is composed of a three-atom thick structure made up of a layer of molybdenum atoms sandwiched between two sulfur layers as shown in Figure 4. By exfoliating it one can produce a 2D membrane composed of a monolayer MoS_2 sheet [27], but MoS_2 monolayers can also be grown by deposition techniques such as chemical vapor deposition (CVD) [28].

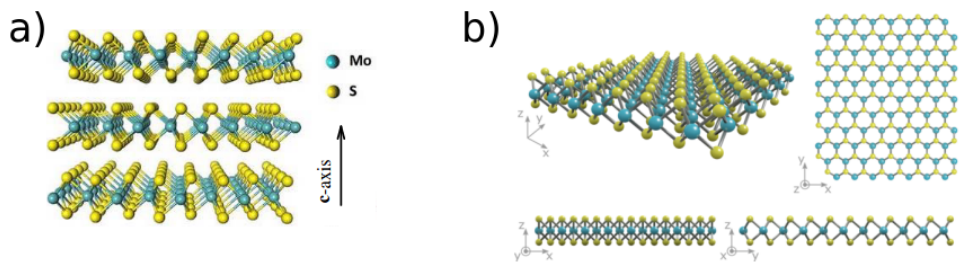

Figure 4: Atomic structure of MoS_2. a) Molybdenite crystal [29] b) monolayer MoS_2 [30]

Monolayer MoS_2 also exhibits remarkable properties such as high mechanical strength [31]

and a wide range of electrical properties [32, 33]. When it comes to its interactions with water molecules and salt ions, one difference between MoS_2 and graphene is very significant: MoS_2 exhibits charge polarization, due to Mo and S atoms' differing electronegativities. As a result, MoS_2 is more hydrophilic than graphene, which is highly hydrophobic and requires pore functionalization with hydrophilic groups in order to achieve high water flows [10, 34]. This indicates that MoS_2 nanopores are a viable candidate for a RO desalination membrane, and its naturally hydrophilic pores can greatly reduce time and costs in the fabrication of nanoporous MoS_2 membranes. In addition to that, the possibility of creating pores with Mo or S terminations allows for an easier tuning of nanopore functionality and does not require complex fabrication techniques like it does for graphene nanopores [35]. This is a very useful feature since pore functionality has been shown to increase water flow and ion selectivity, while at the same time compromising salt rejection [10], meaning a delicate tuning of the pore's charge distribution must be achieved.

The literature on nanoporous MoS_2 as a desalination membrane is still somewhat scarce, but it suggests that it may be more efficient than graphene as a RO desalination membrane. Aluru at al. reported in a computational study [36] that monolayer MoS_2 with Mo-terminated nanopores exhibits complete salt rejection with water flowrates 2-5 orders of magnitude higher than commercial desalination membranes, and a 70% increase with regards to graphene based membranes. The authors attribute this difference to MoS_2's increased hydrophilicity and it hourglass shaped pores. In [37], Farminai et al. carried out simulations for five different kinds of 2D membranes in order to determine the mechanisms regulating water permeation and salt rejection. They showed that MoS_2 nanoporoes maintained over 99% salt rejection, and always exhibited at least 20%-38% higher water permeation than $MoSe_2$, graphene, phosphorene or boron nitride ones. They attributed this difference to MoS_2's higher hydrophilicity, water velocity and diffusion coefficient within the pore.

Multilayer membranes have also been considered for desalination purposes. Grossman et al. provide in [38] a computational study of bilayer graphene's performance as a desalination membrane. They showed that introducing a second layer of graphene within a few angstroms from the first one, allowing for the presence of water inbetween the two plates, strongly improved its salt rejection. For a nanopore of radius 0.45nm, salt rejection improved from $\sim$ 75% to nearly 100% when layer separation was equal to 0.8nm and both pores were highly misaligned. This is caused by the narrow spacing between both graphene sheets, which forms a nanochannel of width narrower than the diameter of hydrated Na^+ and Cl^- ions and acts as an additional energy barrier to the passage of ions. This improvement does, however, come at a cost since a two layered membrane has a water flow around 50% lower than a monolayer one, which is the loss in water flow predicted by classical hydrodynamics [38]. Similar results were also reported by Zhang et al [39].

The trade-off between higher salt rejection and lower water flux may still be advantageous in some cases, as water flow has been shown to increase 5-6 fold between MoS_2 pores of diameters 0.97nm and 1.33nm. However, the smaller pore exhibits a salt rejection of $\sim$ 100%, which is only $\sim$ 60% for the larger one [40]. A flux loss of half for the 1.33nm diameter pore would still represent water flow two to three times higher than for the 0.97nm diameter pore, assuming a 50% flux loss. Therefore, if a second MoS_2 layer with pores of diameter 1.33nm can increase salt rejection to 100% as it did for graphene [38] it would still perform significantly better than a monolayer membrane with 0.97nm pore diameter.

Naturally occurring molybdenite has MoS_2 sheets packed very close together making it impermeable. However, through a combination of exfoliation and re-stacking, a hydrated multilayer MoS_2 membrane can be produced as shown in [27]. In it, Mi et al. showed that this membrane is stable in water for at least 48 hours, and that layer separation increased from 0.62nm to 1.2nm for the hydrated system, allowing for the accomodation of a confined water bilayer in between each pair of MoS_2 sheets. Graphene oxide multilayer membranes on the other hand, were shown to desintegrate pretty rapidly once hydrated. Graphene oxide nanochannels tend to swell when exposed to water which not only leads to its breakup, but also increases the channel's thickness, compromising salt rejection. MoS_2 multilayer membranes, on the other hand, preserve its geometry for long time periods making it a more suitable candidate for a desalination membrane.

Multilayer nanoporous MoS_2 is thus, a promising desalination membrane due to its high stability in water, water flow and mechanical strength. It is also more easily produced than graphene based technologies since it does not need to be functionalized, nor is it necessary to add crosslinkers to it in order to avoid swelling/narrowing of the channels [27], which not only reduces manufacturing costs but also guarantees a high surface smoothness. It is therefore important to study the mechanisms behind water and ion transport across such membranes.

In all of these materials the key challenge is to understand how the properties of the membrane's surface combined with the anomalies of water lead to high water mobility. Water has over 70 anomalous thermodynamic, dynamic and structural behaviors [41]. These anomalies are related to the fact that water molecules form hydrogen bonds with each other [42], up to four per molecule,

thus creating complex geometric structures as seen in Figure 5(a). These bonds appear only when the molecules are at certain angles and distances from its neighbours as illustrated in Figure 5(b). This arrangement decreases the overall energy of the system as significantly more energy is needed to break down hydrogen bonds than it is for Van der Waals interactions at room temperature [43]. Both in nanotube systems and in 2D nanopores the hydrogen bond network that forms is relevant and has to be taken into account when studying water transport.

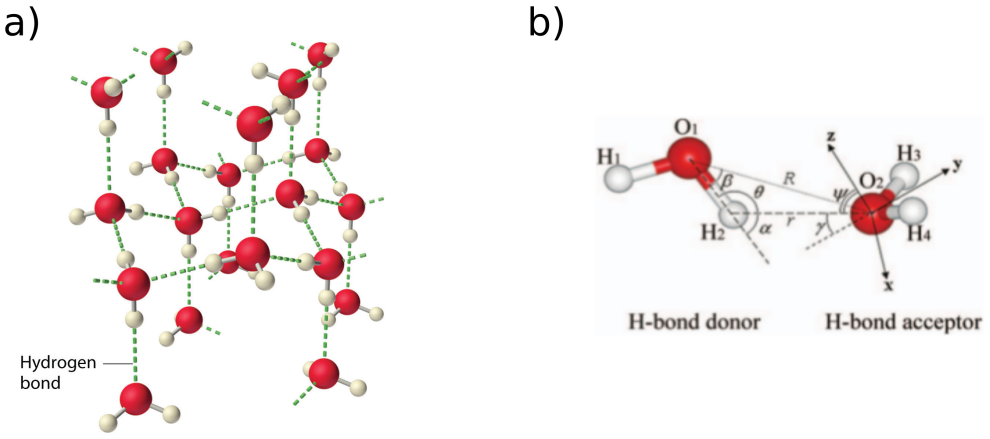

Figure 5: a) Hydrogen bond network of water [44]. b) Hydrogen bond geometry [45]

In this document we attempt to elucidate the mechanisms behind water permeability and salt rejection in MoS_2 nanopores by exploring two complementary ideas. We compare water and ion transport at different MoS_2 charge distributions at fixed geometry in order to explain how electrostatic forces influence these processes. We study water transport in both mono and bilayer MoS_2 and ion transport only for monolayer MoS_2. Then, in the case of bilayer membranes, we also consider membranes with fixed charge distributions and varying geometries in order to understand how pore alignment and the separation between the MoS_2 layers influences water mobility. All of this allows us to understand how charge and shape compete in regulating these processes, and show that it translates into a competition between repulsive/attractive electrostatic forces between MoS_2 and water/salt ions and interactions between particles in the saltwater solution, which include ion-water/ion-ion interactions and water-water forces represented by the hydrogen bond network.

The rest of this document is structured in the following manner. In chapter 2 we provide a detailed explanation of the models and methods used in the implementation and post analysis of our simulations. Chapter 3 offers an analysis on the phenomena governing water and ion transport across monolayer MoS_2 nanopores. Chapter 4 highlights the mechanisms controlling water flow across bilayer MoS_2 membranes. Finally, chapter 5 provides a summary of the obtained results and its potential applications.

2 Methods and Models

2.1 Molecular dynamics simulations

Although it is a computational tool, molecular dynamics operates very similarly to an actual experiment. The simulation starts by defining the system's initial conditions and geometry in what is called a simulation box. After an equilibration step the simulation begins and measurements are made along with it. Just like in a real experiment, if data is too noisy its accuracy can be increased by averaging the results during long periods of time or by repeating the experiment multiple times, assuming the system respects the ergodic hypothesis [46].

A molecular dynamics simulation is composed of the following steps:

Simulation steps

0^{th} step - Defining initial conditions

- Define the size of the system and its boundary conditions in the XYZ dimensions
- Set initial positions and velocities for all particles in the system
- Define the force fields

⇓

Loop:

⇓

1^{st} step - Calculate forces on each particle

- Calculate pair interactions between all particles in the system

⇓

2^{nd} step - Integrate equations of motions

- Use the computed forces to integrate Newton's equations of motion for each particle
- Update particle positions and velocities

⇓

3^{rd} step - Measurements

- Compute and output measured quantities

The simulation starts by setting up the system, particles are added to the simulation box with its initial positions and velocities and the size of the simulation box is defined alongside its boundary conditions. The interactions between each types of particles and chemical bonds are defined forming what is called the simulation's force field.

Then the simulation enters its three step loop, first each pair interaction within a defined cutoff radius is computed in order to determine the total force being exerted on each particle. This force is used to integrate Newton's equations of motion and determine the new positions and velocities of each particle. At last, measured quantities are computed and output to a determined file. The loop then restarts by calculating particle interactions in the next timestep.

Molecular dynamics simulations were employed in this work to study the desalination performance of MoS_2 membranes. This is a very popular method in the study of microscopic phenomena as it generates data on individual trajectories of each individual particle. From this data, thermodynamic quantities such as temperature and pressure can be derived using statistical mechanics, while also allowing for the study of dynamic processes such as water and ion transport across the membrane [46].

These features make molecular dynamics a very powerful tool in the study of nanoscale desalination membranes. There already exists a vast literature on this subject, despite it being a relatively new field of study.

2.2 Computational models

The atomistic water model chosen for our simulations was TIP4P/ϵ [47] and the model chosen for salt was NaCl/ϵ [48]. These two models combined reproduce experimental measurements of the dielectric constant of water + salt solutions. [48] For MoS_2 we used the parameterization proposed by Kadantsev and Hawrylak [49] and for carbon atoms the one defined in [50] by Hummer et al. Interaction parameters are modeled by a sum of Lennard-Jones and coulombic contributions. The cutoff for LJ interactions was set to 1nm. Long-range electrostatic forces were calculated using the pppm K-sapce solver [51]. Non-bonded interactions were defined using the Lorentz-Berthelot rule [52]. The O-H bonds and H-O-H angles were kept fixed using the SHAKE algorithm [53, 54], as it has been shown that molecular vibrations and polarizability play a negligible role in the dynamics of saltwater transport across nanopores [10]. A timestep of 2 femtoseconds was used. The parameters defining the simulation's force field are given in Table 1.

Species	σ_{LJ}	ϵ_{LJ}	**Charge**
O - TIP4P/ϵ [47]	3.165	0.1848	-1.054
H - TIP4P/ϵ [47]	0.0	0.0	+ 0.527
Na/ϵ [48]	2.520	0.0346568	+ 0.885
Cl/ϵ [48]	3.850	0.382437	- 0.885
C [50]	3.40	0.0860	0.0
Mo [49]	4.20	0.0135	+ 0.6
S [49]	3.13	0.4612	- 0.3

Table 1: Lennard-Jones and coulombic interaction parameters for each atom type

2.3 Simulation details

The simulation setup consists on the creation of a simulation box where MoS_2 separates two reservoirs. This is shown in Figures 6 and 7.

For monolayer MoS_2 membranes, illustrated in Figure 6, the simulation box is composed of the following parts. The **feed**, container holding the input solution which, in the case of desalination, corresponds to saltwater. When studying a pure water system (Figure 6(a)) - no salt ions present - this reservoir is initially filled with 2304 water molecules, and when simulating the desalination process (Figure 6(b)) 2224 molecules of water, 40 Na^+ ions and 40 Cl^- ions are initially present in this reservoir, giving the solution a concentration of approximately 1M, slightly higher than that of seawater at 0.6M [55]. Located on the opposite side of the MoS_2 membrane is the **permeate** reservoir, which is filled with 1008 water molecules at the start of the simulation and towards which the filtered water flows to. Each reservoir is delimited MoS_2 on one side and by a graphene sheet on the other. Graphene sheets will be used as pistons through which external pressure is applied to the system. When simulating the reverse osmosis process a pressure of 1atm is applied to the piston on the permeate side and a higher pressure is applied to the feed.

In the case of bilayer membranes, shown in Figure 7, a third reservoir called the **interlayer** reservoir, located between the two MoS_2 sheets, is initially filled with 300 water molecules(Figure 7(b)).

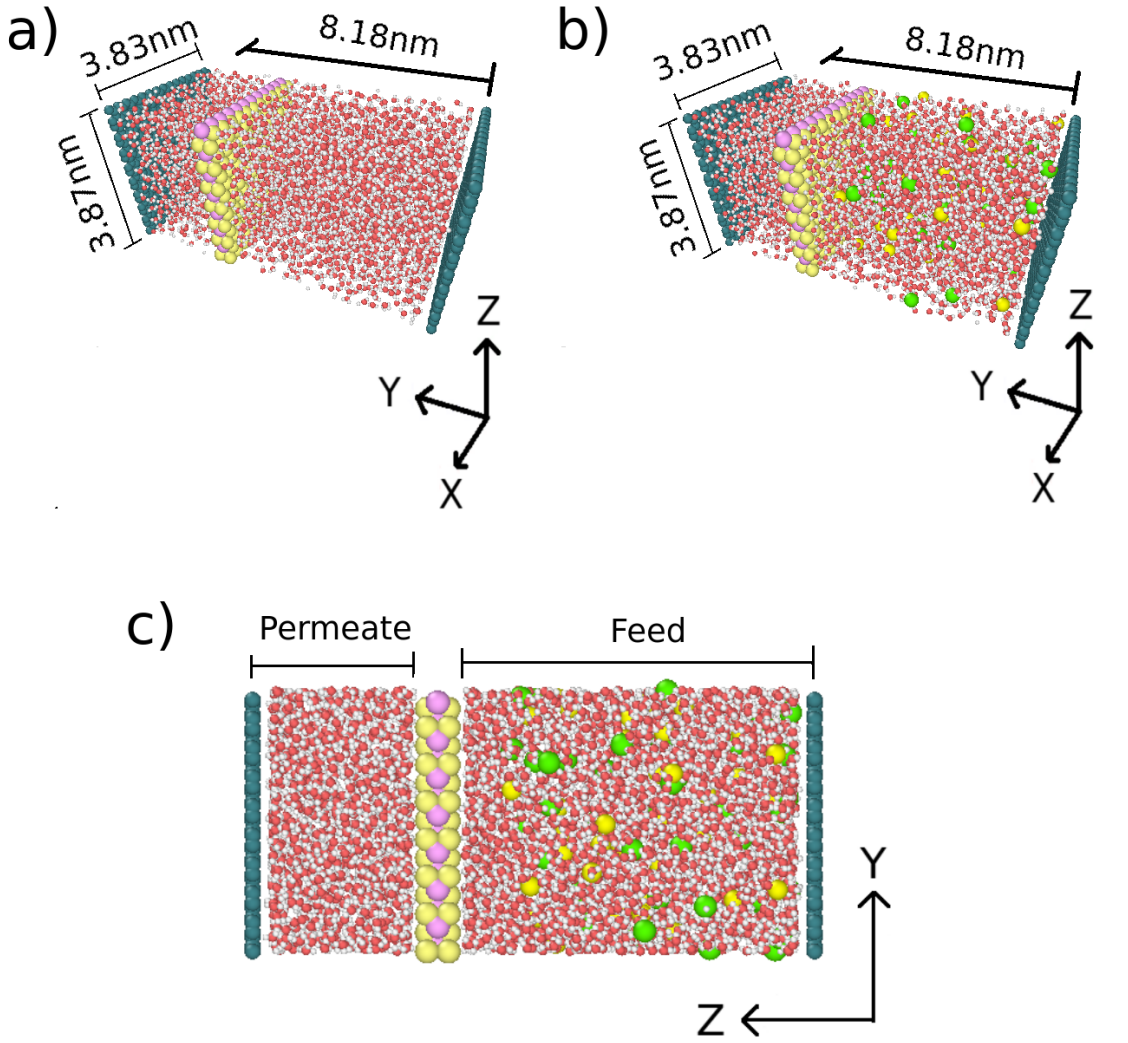

Figure 6: Simulation Box for monolayer MoS_2 for a a)pure water system and a b)saltwater system. c)Side view of the reservoirs. Red, white, bright yellow, green, pink and light yellow spheres represent oxygen, hydrogen, Na^+, Cl^-, molybdenum and sulfur atoms/ions.

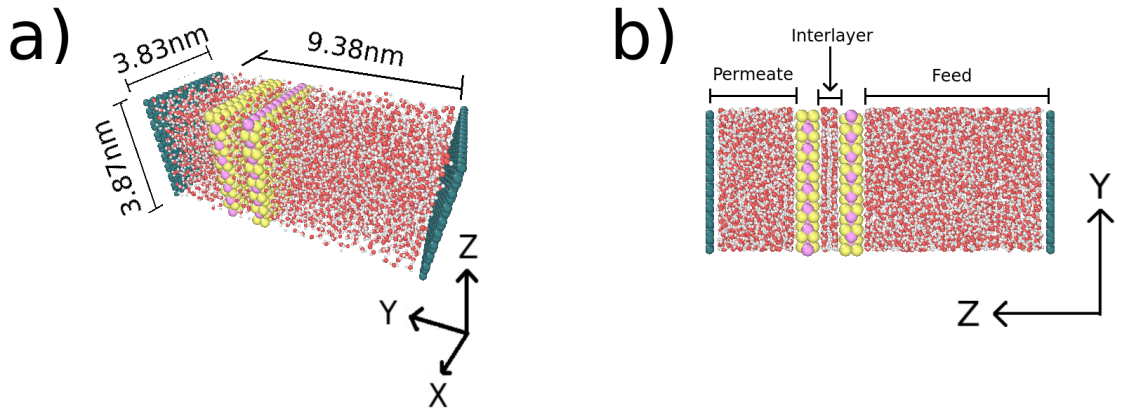

Figure 7: Simulation Box for bilayer MoS_2 for a a)pure water system. b)Side view of the reservoirs. Red, white, pink and light yellow spheres represent oxygen, hydrogen, molybdenum and sulfur atoms.

The simulation box has a fixed size of 3.83x3.87x22.4 nm. Periodic boundary conditions are set in all dimensions to make sure the solution acts as an infinite liquid in the XY dimension, reproducing the behavior of a bulk material. A large empty space is left in the Z direction so that

the graphene pistons can move as the solution is filtered and to make sure that they are far enough apart so as to not interact with each other due to the periodic boundary conditions. The geometry of Mo and S atoms in the membrane were taken from [56]. The graphene pistons were created using VMD [57]. In order to create a graphene sheet with evenly distributed carbon atoms which also fits perfectly into the fixed X and Y dimensions of the box, distances between the carbon atoms had to be slightly dilated. This guarantees that pressure is uniformly applied to all parts of the system. The MoS_2 membrane is kept frozen in place throughout all simulations, as it has been shown that the displacement of the atoms in 2D membranes caused the application of an external pressure has a negligible contribution to its desalination performance [58]. The graphene sheets on the other hand behave as a rigid plane that can only move in the Z direction. All carbon atoms on a single sheet always have the same Z coordinate, ensuring the piston moves as a single entity, while each atom's X and Y coordinates are kept fixed.

2.4 Membrane characteristics

The goal of this work is to determine the role of membrane geometry and charge distribution in RO desalination. Therefore, different MoS_2 membranes were studied. Geometrical parameters like pore size - for monolayer membranes - and layer separation and pore alignment - for bilayer ones - were considered. Different charge distributions were introduced by changing the intensity of the charge polarization in MoS_2.

MoS_2

Two different phases of MoS_2 can occur naturally, the 2H and 3R phases [59]. The most common phase is the 2H phase [60] and most litterature regarding MoS_2's application to water filtration is based on it. An illustration of this phase can be seen in Figure 4 in chapter 1. The parameterization for MoS_2 given in Table 1 refers to the 2H phase.

Charge distribution

In order to create MoS_2 membranes with different charge distributions we introduced a new parameter into the system called the charge multiplier (Q), which modifies the charges attributed to Mo and S atoms in our simulations as follows:

$$\textbf{Mo atom charge} = 0.6 * Q$$
$$\textbf{S atom charge} = -0.3 * Q$$

where 0.6 and -0.3 are the coulombic charges attributed to molybdenum and sulfur atoms in our molecular dynamics simulations as stated in Table 1. By varying the value of Q we can produce MoS_2 membranes with different degrees of charge delocalization in order to tune the strength of the electrostatic forces between MoS_2 and the water molecules and salt ions in the system. A charge multiplier of Q1 represents regular MoS_2, with its characteristic charge distribution. Q0 and Q2 represent fictitious materials with equal geometry to regular MoS_2 but different charge distributions, Q0 representing a system with no charge delocalization and Q2 one with charge polarization two times stronger.

Membranes with charge multipliers Q0, Q1 and Q2 are the subject of our study in this document. It is by studying water and salt transport in such membranes that we can understand the role that electrostatic interactions between MoS_2 and the water/salt ions plays in the desalination process. Eventually Q3 and Q5 system may appear but only as a tool to check previous results. a Q(-1) charge multiplier also appears at one point, representing systems with inverted charge distribution, where Mo is now negatively charged and S is positive. For all values of Q, the sum of all coulombic charges in the membranes is equal to zero, maintaining the membranes charge neutrality.

In monolayer pores, the charge distribution is relevant for in-pore transport of particles. In bilayer membranes however, a few layers of water molecules are confined between two MoS_2 plates - the interlayer region, through which they must travel in order to flow to the permeate container - so we can expect electrostatic interactions with the membrane's surface walls to also play a significant role in water dynamics.

We remind the reader that MoS_2 is a neutral material and that the attribution of coulombic charges to individual Mo and S atoms is an artificial way of reproducing the uneven charge distribution across MoS_2 in our simulations (see section 2.2).

Geometry - monolayer membranes

In monolayer membranes, the only variation in membrane geometry that is considered is **pore size**. Pores in our system were created by chosing a point located at the center of an Mo atom and deleting all atoms within a certain radius from it. Two pore diameters were considered, 0.97nm and 1.33nm. These values of diameter produce pores with equal numbers of Mo and S terminations. Pores of such kind have been analyzed in previous studies regarding RO desalination simulations [61, 62, 63, 64, 65, 66], however, other types of pores with only Mo or S terminations have also been studied [36], as well as less symmetrical pores not created by deleting atoms in an organized manner [36, 37]. It is important to keep these differences in mind as pore chemistry can drastically alter its functionality. The pores considered in this work have been reported to exhibit water flowrates about one order of magnitude lower than those for Mo terminated pores [36, 40, 65].

These diameters were chosen based on previous literature on MoS_2 membranes, which showed that the nanopore with diameter 0.97nm is the largest MoS_2 nanopore which provides salt rejection near 100% [40]. The nanopore of diameter 1.33nm is the smallest MoS_2 pore which does not reject salt ions at levels close to 100% [40]. These two pore sizes were considered in order to study ion rejection and water transport mechanism. Both nanopores are represented in Figure 8.

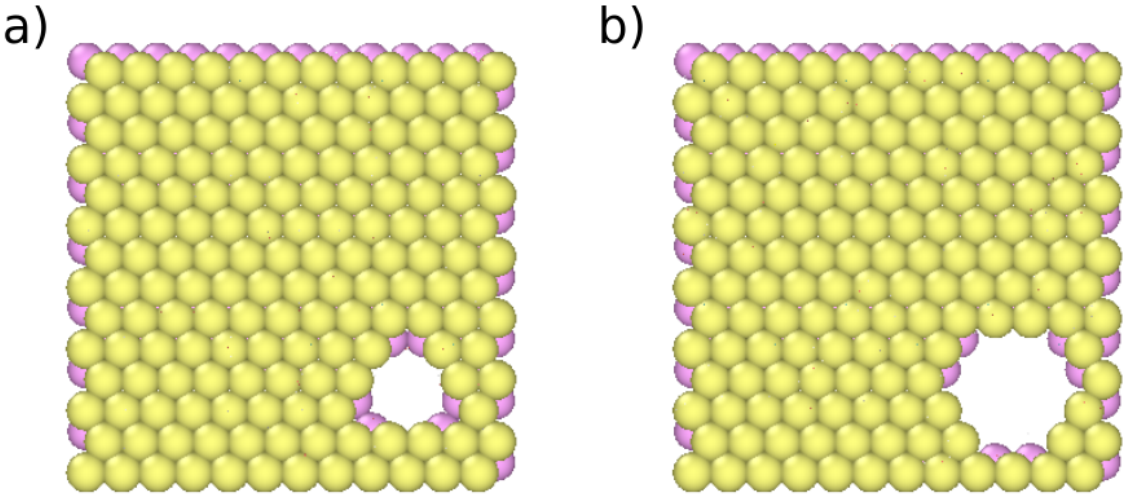

Figure 8: Different pore diameters considered. a)0.97 nm and b)1.33nm.

Geometry - bilayer membranes

In bilayer membranes, a wider range of geometrical variations are possible. In this case we only consider the larger (1.33nm diameter) pores. Monolayer 0.97nm diameter nanopores already exhibit nearly 100% salt rejection [40], therefore, little improvement would be caused by the introduction of a second MoS_2 layer. On top of that, obtaining statistics on ion and water transport for a bilayer membrane with 0.97 nm pores would be too costly computationally as simulation times would be too long. The 1.33nm pores are interesting in this case since they only exhibit around 60% salt rejection for monolayer MoS_2 [40] and the introduction of a second layer could potentially improve its performance.

We will now discuss the two geometric parameters exclusive to bilayer membranes which are analyzed in this work. They are the **pore offset** and the **layer separation**.

Pore Offset

In a bilayer membrane, two nanopores are present. It is then possible that they might be misaligned, which is represented in Figure 9. We name this property **pore offset** and its influence on water transport across the bilayer membrane will be studied for three different values of pore offset: 0nm, 0.96nm and 2.57nm. Offset 0nm represents perfectly aligned pores and 0.96 nm represents slightly misaligned pores, with an offset smaller than the pore diameter, which means some overlap between the pore areas still exists. In such cases it is possible for water molecules to cross the membrane without traveling through the entirety of the interlayer region. Finally, the 2.57nm offset represents a large pore misalignement, meaning water molecules must necessarily travel a great length in the interlayer region in order to reach the permeate reservoir.

Due to the periodic boundary conditions the maximum possible offset that can be created is equal to half the size of the diagonal of the MoS_2 membrane, which equals 2.72nm. The reason the

largest offset considered in this work is slighlty smaller than this value is that offsets were created by displacing one of the MoS_2 sheets by units of the MoS_2 crystal lattice, in order to preserve the stacking of MoS_2's 2H phase.

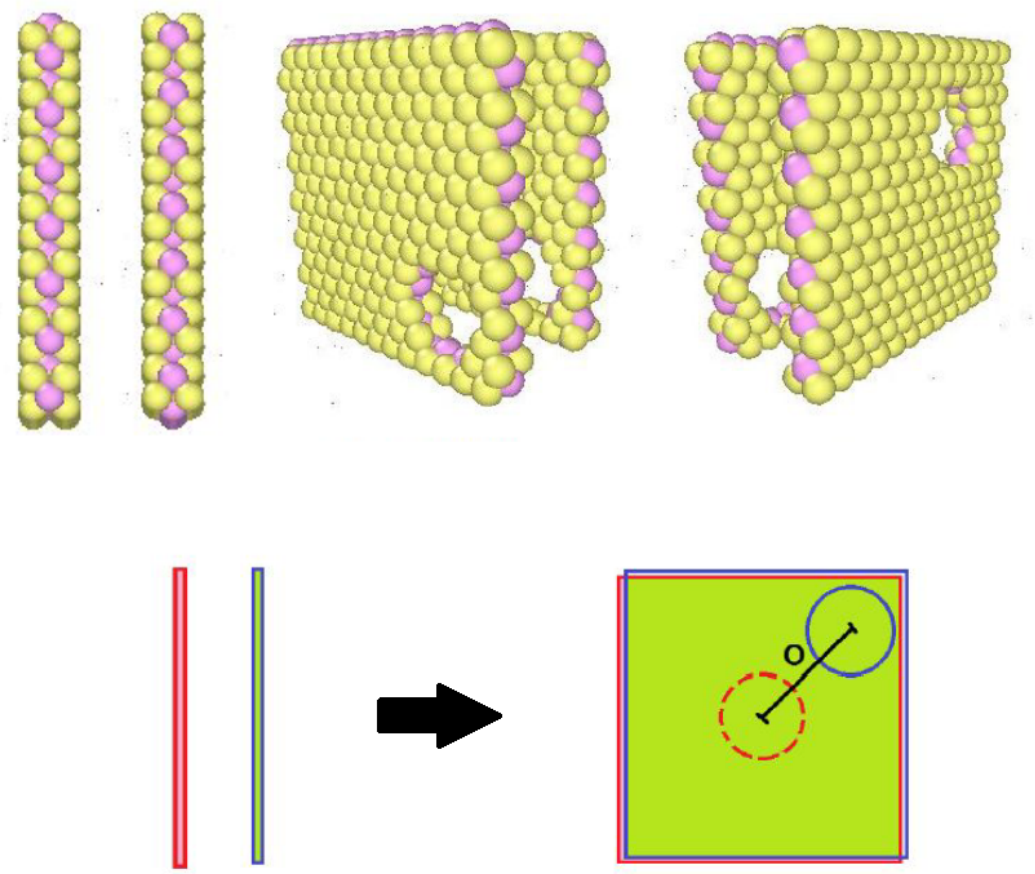

Figure 9: (Top) Side view of MoS_2 sheets with perfectly aligned and misaligned pores. (Bottom) Simplified illustration of the membrane, the distance O measured between the center of both pores on the XY plane is defined as the pore offset.

Layer Separation

The distance between the two MoS_2 sheets was set to 1.2nm, measured from the center of molybdenum atoms on both sides. This was taken from [27], where it was shown experimentally that MoS_2 presents a stable hydrated state when in an aqueous environment where layer separation is equal to 1.2nm. It is possible to produce membranes with different separations [67, 68, 69, 70, 71], but we focus on this particular case as it appears to be the most easily produced for real world application. In one of our analysis in chapter 4 we briefly discuss the influence of layer separation on water flow across the membranes. We chose the letter H to represent layer separation.

2.5 Running the simulation

Once the simulation box and all necessary parameters have been defined the simulation can start running. To run our simulations we used the LAMMPS package [72]. Before applying the pressure gradient the system needs to be equilibrated. Every simulation conducted in this work went through the exact same multi-step equilibration process, which is detailed below.

Simulation steps

First step
- Duration: 0.05 ns
- Graphene pistons are frozen in place
- NVT ensemble brings system from 0K to 300K.

⇓

Second step
- Duration: 0.5 ns
- Graphene Pistons frozen
- NVE + langevin thermostat keeps T = 300K

⇓

Third step
- Duration: 0.4 ns
- Graphene pistons frozen
- NVT ensemble keeps T = 300K

⇓

Fourth step
- Duration: 1 ns
- Pistons released, 1 bar pressure applied to each side
- NVT ensemble keeps T = 300K

⇓

Fifth step
- Duration: 2 ns
- Graphene pistons frozen
- NVT ensemble keeps T = 300K

⇓

Pore is opened

⇓

Sixth step
- Duration: 0.4 ns
- Pistons released, 1 bar pressure applied to each side
- NVT ensemble keeps T = 300K

⇓

Seventh step
- Duration: 0.4 ns
- Graphene pistons frozen
- NVT ensemble keeps T = 300K

⇓

Production run
- Duration: > 10 ns
- Pistons released, pressure gradient applied
- NVT ensemble keeps T = 300K
- Predetermined quantities are computed and collected

The first step is the heating step, which brings the water molecules and salt ions from 0K to 300K while the graphene sheets are kept frozen in place. The temperature is controlled using the NVT ensemble with a damping factor of 0.2 timesteps. This step lasts for only 0.05ns.

On the second step the NVT ensemble is replaced by an NVE ensemble and the temperature of the system is maintained at 300K by a langevin thermostat with the same damping parameter as before. This step lasts for 0.5ns. The NVE + langevin thermostat scheme was used instead of the NVT ensemble in this step as it brings the system close to equilibrium faster.

The third step replaces the NVE + langevin thermostat scheme by the NVT ensemble once again, with damping factor 0.2 timesteps. A drag of value 0.2 is used to reduce temperature and pressure oscillations. This step lasts for 0.4ns.

On step four the graphene pistons are unfrozen for the first time and a pressure of 1bar is applied to each of them in order to mimic the atmospheric pressure and bring the concentration close to the value of $1 g/cm^3$. This goes on for 1ns.

Step five goes on for 2 ns and consists of freezing the graphene sheets once more. After step five the necessary atoms in the MoS_2 membrane are deleted to create the nanopore. The system

is already equilibrated and two short equilibration steps are added to allow for equilibration of the system near the newly generated pore and inside the interlayer region in the case of bilayer MoS_2 membranes .

Step six sees the application of atmospheric pressure to the pistons once more, while on step seven they are once again frozen. They last for 0.4 ns each.

The seemingly excessive amount of equilibration steps is due to the difficulty in equilibrating the water molecules in the interlayer region for bilayer membranes.

Once the equilibration is completed the pressure gradient necessary for the reverse osmosis process is applied. This is done by applying a 1bar pressure to the piston on the permeate side and a higher pressure to the feed side, as illustrated in Figure 10. In order to apply a certain pressure to a graphene piston, equal forces in the Z direction are applied to each of its carbon atoms which add up to a value F such that the applied pressure is equal to F/A, where A represents the system's area in the XY plane. This pressure gradient causes a flow of particles from the feed to the permeate reservoir. Real RO desalination plants use pressures in the range of 5-10MPa [58], however, in order to obtain the necessary amount of statistical data, pressures in the range of 100-250MPa were used. This is a common scheme in molecular dynamics simulations [10, 36, 38, 61, 63] due to the high computational cost of the simulations, it has nonetheless been shown to produce correct results, from which behavior at lower pressure gradients can be extrapolated.

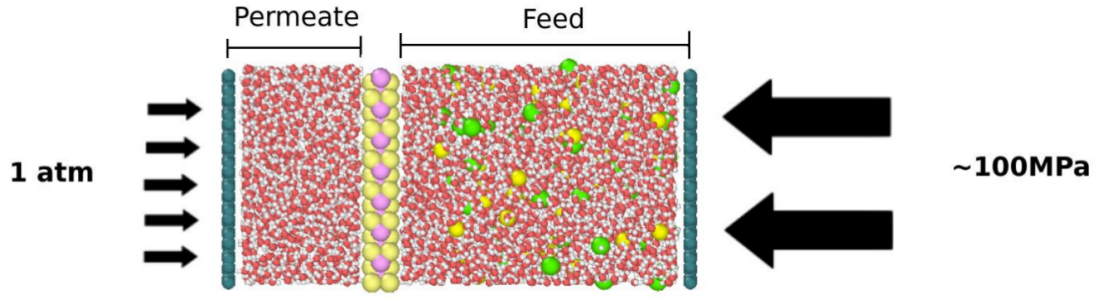

Figure 10: Side view of the system. A higher pressure is applied to the Feed reservoir, creating a pressure gradient. Red, white, bright yellow, green, pink and light yellow spheres represent oxygen, hydrogen, Na^+, Cl^-, molybdenum and sulfur atoms/ions.

2.6 Measured quantities

During the production run of the simulations, data regarding thermodynamic properties of the systems and individual properties of the atoms is collected. They are used to calculate a vast range of measurements which aid us in understanding the underlying phenomena governing the RO desalination process. The rest of this chapter is dedicated to defining and giving brief details on the nature of these measurements and how they are obtained.

Two kinds of data files are output by our simulations. The first one we call the **flux files**, where data regarding the number of water molecules and salt ions in each of the defined regions is computed every 100 timesteps (0.2 picoseconds). The second kind are the **trajectory files** where the individual positions, velocities and exerted forces on a defined set of particles is printed at a constant rate of $\sim$ 1 picosecond.

Water flowrate and Salt rejection

The two most important quantites when evaluating the desalination performance of a reverse osmosis membrane are the **water flowrate** and the **salt rejection**. As their names suggest, the first one indicates the amount of water that crosses the membrane in a given time and the second one its capacity to block the passage of salt ions. Both quantities are measured from the flux files generated during the simulations.

In order to guarantee that the quantities obtained at different values of applied pressure, charge multiplier or pore offset can be compared with eachother, we define a range of analysis for the data. This assures that all systems are being considered under the same conditions.

This process is illustrated in Figure 11 where the example given is the calculation of the water flowrate. The black curve represents the amount of water molecules in the permeate reservoir (Y

axis) at a given time (X-axis). The red line represent the line obtained by the linear fit of the data. The dashed lines represent values relevant for the definition of the range of analysis of the data.

In defining our range of analysis we naturally ignore the data corresponding to the equilibration steps, which ends at 4.75 ns, represented by the black dashed line in Figure 11. When pressure is first applied to the system there is a non linear increase of water molecules crossing the membranes, however the system quickly reaches a steady state of linear water flow. To reduce the error caused by this transient state we also ignore the data between times 4.75-5.0 ns. We define a time $t_0 = 5.0ns$, represented as the first blue dashed line in Figure 11, as the starting time of our analysis. Salt rejection in particular, is very sensitive to the salt concentration in the feed, which tends to increase with time. We, therefore, must establish a reference time for the analysis of the data. We set a final time t_f, represented by the second blue dashed line in Figure 11, which corresponds to a certain fixed amount of filtered water molecules, or water threshold (W_f), represented by the green dashed line in Figure 11.

For monolayer MoS_2 membranes we chose the values $W_f = 1600$ for pores with diameter 0.97nm and $W_f = 2100$ for pores with a diameter of 1.33nm. For the bilayer membrane only pore diameters o 1.33nm were considered and W_f was chosen as 2100 as well. The difference in values is due to the very low water flow in the 0.97nm pores and makes comparison between salt rejection in both pore sizes tricky, however, this is not the main goal of our work. Each individual simulation had its time t_f determined by the instant the number of water molecules in the permeate first achieved the value of W_f.

By fitting the data within the range of analysis with a linear function of the form:

$$y(t) = at + b \tag{1}$$

we obtain the slope of the curve, given by the coefficient a. This coefficient is given in units of water molecules per nanosecond and we will represent the water flowrate with such units towards the rest of this work, except at the final chapter when comparing our data to other results in literature.

The salt rejection is obtained by a simpler process. At time t_f we calculate the following quantity:

$$SR = \frac{N - N_p(t_f)}{N} \tag{2}$$

where N represents the total amount of salt ions in the system and $N_p(t_f)$ represents the total amount of ions in the permeate at time t_f. The salt rejection is expressed as a percentage, a value of 100% means no ions crossed the membrane and a value of 0% means all of them did.

Values obtained for both quantities in independent simulation runs are averaged to yield a mean value and a standard deviation.

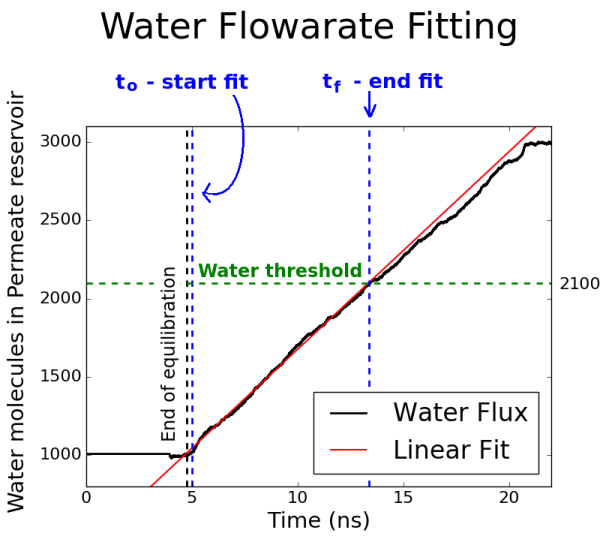

Figure 11: Graphical representation of the fitting procedure for the obtention of the water flowrate in a monolayer MoS_2 membrane with a 1.33nm diameter pore. The black curve represents the number of water molecules in the permeate at a given instant and the red line represents the line obtained by the linear fit. Dashed lines indicate parameters used to define the range of analysis interval. The dasehd line in black represents the end of the simulation's equilibration procedure, the two blue dashed lines the starting and ending instants, t_0 and t_f, and the green dashed line the water threshold (W_f) for the system.

Pore contents

Throughout this document we will refer in many occasions the the average number of water molecules or salt ions inside nanopores or the interlayer region. These quantities are also calculated from the flux files. Each flux file provides the quantity of water molecules and each species of salt ion, Na^+ and Cl^-, present in each region of the simulation box at certain timesteps. We calculate the mean value of these quantities in the range of analysis interval defined by t_0 and t_f and average them with the results obtained in independent simulation runs to obtain a mean value and a standard deviation.

Density Maps

Oxygen density maps are heatmaps that indicate the local density of either water molecules or ions in a defined 2D region in space. They are calculated from the trajectory files which store the positions of particles in the system at given instants in time. The first step in computing it is defining the region in space to be analyzed, for example a nanopore. The XY coordinates limiting the region corresponding to the nanopore are then determined and each dimension divided in N equal sized bins, creating an NxN grid. A certain width for the bins is defined as well, which corresponds to two limiting values in the Z direction, giving each bin a volume.

Once the grid is fully defined in all dimensions, the position of the particles are assigned to a certain bin, one by one. This is performed for all timesteps within a defined interval. For ion density maps the time interval is always the one defined by t_0 and t_f. For water molecules the interval is shorter since less statistical averaging is needed and it corresponds to 2.5ns intervals. The obtained histograms are then divided by the number of timesteps and normalized by the volume of the bins to yield a value expressed in units of g/cm^3 for water and $ions/cm^3$ for salt ions.

Water molecules' orientation

The orientation of water molecules inside the nanopores and in the interlayer region is analyzed in order to highlight the role of electrostatic forces in rotating them. The orientation is only measured with respect to the Z axis as is represented in Figure 12. The system is divided in bins of length ΔZ along the Z axis and the angle between each water molecule's dipole vector and the Z axis is calculated. These values are averaged inside each bin and a standard deviation is calculated. The results are represented by a line corresponding to the mean value in each bin and a shaded region above and below it indicating its standard deviation.

This quantity highlights the angular constraint imposed on water molecules by electrostatic forces between water and MoS_2 which can impede water flow and break down hydrogen bonds when it becomes too intense in a certain region. A high angular constraint translates into a small standard deviation in the measurements.

This method was employed in molecular dynamics studies in order to characterize the spatial distribution of water confined in nanopores and nanoslits [62, 73] and how it is affected by spatial and electrostatic characteristics of the confining medium..

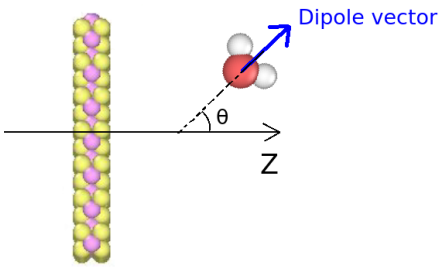

Figure 12: Calculation of the orientation angle of water molecules.

Potential of mean force

The **potential of mean force** (PMF) is calculated for water molecules in pure water systems in order to determine the potential energy profile of the water molecules in and around the nanopores. The PMF is calculated in simulations with no applied pressure, where only 1 atm is applied to each graphene piston - to simulate atmospheric pressure - during the production run. The usual equilibration scheme described in section 2.5 is performed, and a subsequent production run of 5 ns is then performed.

Position data for water molecules is taken from the trajectory files. The system is divided in bins of length ΔZ along the Z axis and the number of oxygen atoms in each bin is computed. We then determine the local density in each bin, $\rho(z)$, and divide it by the density of bulk water ρ_0. The PMF can then be obtained by the following equation:

$$PMF(z) = -k_b T log(\frac{\rho(z)}{\rho_0}) \ . \tag{3}$$

where k_b is the boltzmann constant and T is the system's temperature in Kelvin. The PMF is expressed in the unit kcal/mol.

The potential energy profiles obtained through PMF calculations indicate the amount of energy necessary for a water molecule to cross a certain region, like a nanopore for example which presents as a peak in the PMF. Water molecules will tend to accomodate around energy minima of the PMF. Regions with a high potential energy value, on the other hand, will have lower values of water density.

Hydrogen bond network

The hydrogen bond network represents the complex geometrical structures formed by water molecules interacting via by hydrogen bonds. Hydrogen bonds in our simulation are determined by a simple geometric criterium [74] represented below:

$$R_{O_1O_2} < 0.35nm \tag{4}$$

$$\beta_{H_2O_1O_2} < 30° \tag{5}$$

where $R_{O_1O_2}$ represents the distance between both oxygen atoms and $\beta_{H_2O_1O_2}$ the angle between the line segment crossing O_1 and H_2 and the one crossing H_2 and O_2. All quantities are illustrated in Figure 13(a).

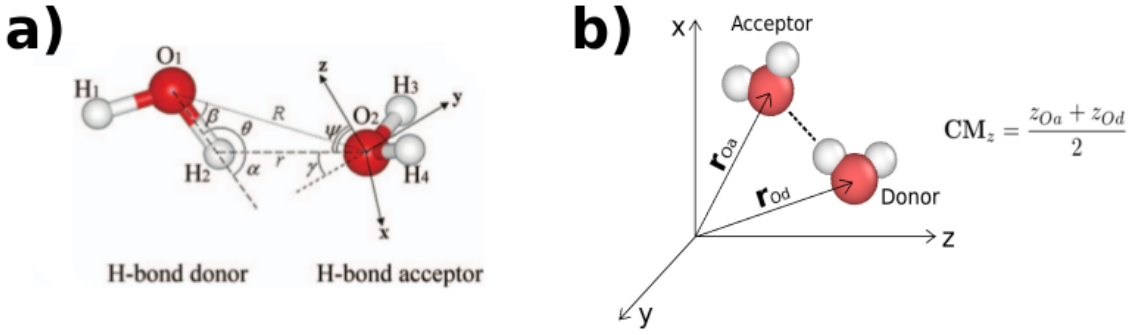

Figure 13: a) Hydrogen bond geometric parameters [45]. b) Hydrogen bond's center of mass.

Three quantities regarding the hydrogen bond network are utilized in this work. The first one is the **average number of hydrogen bonds formed by water molecules in a given region**. After defining a region in space we create a list of all the water molecules contained in this region. We then count the number of hydrogen bonds formed by each one of them and calculate its mean value and standard deviation.

The next property calculated is the **hydrogen bond profile**, which indicates the mean number of hydrogen bonds per molecules in a given point in the Z axis. After dividing the Z axis in bins of length ΔZ we determine the number of hydrogen bonds formed by each molecule in the bin and calculate its mean. This is calculated near and inside the MoS_2 nanopores and allows for a comparison between the number of hydrogen bonds per water molecule formed in bulk water (far from MoS_2) and inside the nanopores or interlayer region.

The final quantity is the **hydrogen bond center of mass** and it is calculated in the interlayer region of bilayer MoS_2 membranes. To obtain this quantity we define a region in space, in this case the interlayer region of bilayer MoS_2, and then calculate the coordinates of the center of mass of all pairs of oxygen atoms forming hydrogen bonds, as shown in Figure 13(b). We then calculate a histogram of the distribution of the Z component of the center of mass. The resulting quantity allows for an understanding of the orientation of the hydrogen bonds in highly confined spaces such as the inside of the bilayer MoS_2 membrane. The shape of the obtained histogram gives an idea

of the degree of organization in the region, which is represented by sharp peaks in the histograms, in contrast to bulk water where there is no anisotropy and the histogram is completely flat.

Radial distribution function

The **radial distribution function** provides information on the spatial correlation between particles of a certain kind. In this work we computed radial distribution functions between oxygen atoms and molybdenum and sulfur atoms of the membrane in the interlayer region of bilayer MoS_2. The calculations are all made at zero applied pressure. The radial distribution function between two atoms (O, α) of different kinds is given by the equation:

$$g_{O\alpha}(r) = \frac{V}{N_O N_\alpha} \sum_{i=1}^{N_O} \sum_{j=1}^{N_\alpha} \left\langle \delta(\boldsymbol{r} - |\boldsymbol{r}_i^O - \boldsymbol{r}_i^\alpha|) \right\rangle \tag{6}$$

where V is the volume of the region being analyzed, N_O represents the number of Oxygen atoms in the region, N_α the number of atoms of type α (Mo or S) and $\boldsymbol{r}^O$ and $\boldsymbol{r}^{\boldsymbol{\alpha}}$ the position vectors of individual oxygen and α atoms. For improved accuracy the $g(r)$ is calculated for various timesteps, in 2000 intervals of 0.5ps for 1ns, and then averaged.

Besides the regular radial distribution function we also calculate a **2D radial distribution function**, in order to better understand how water molecules are distributed along the surface of MoS_2 in the interlayer region. The same procedure employed for the regular radial distribution function is used, however, the Z dimension is ignored, and the calculation only takes place in the XY plane, the plane parallel to the MoS_2 plates. Only one of the two water layers formed in the interlayer region and the MoS_2 sheet closest to it is considered, as illustrated in Figure 14. This quantity allows for a visualization of which sites in the MoS_2 sheets have a higher affinity for water molecules.

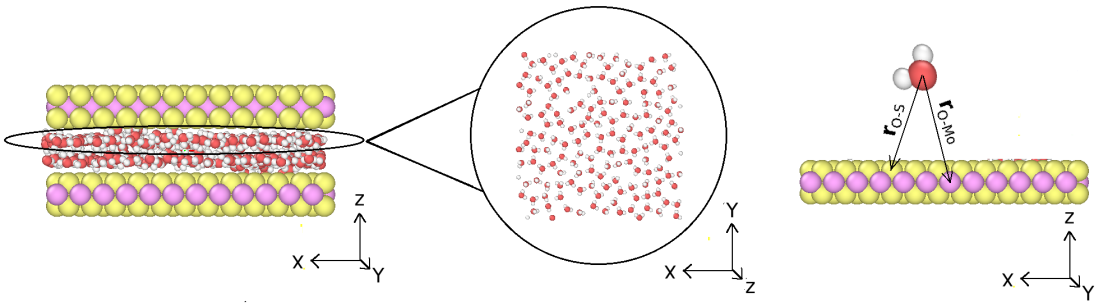

Figure 14: Representation of the procedure employed in the calculation of the 2D radial distribution functions.

Water flux loss

The **water flux loss** ($\Delta\Phi$) is a quantity used to compare water flowrates between different kinds of membranes and quantify the amount of water flow that is lost as the system is modified in any given way. It is defined by the following equation:

$$\Delta\Phi = 1 - \frac{\Phi_m}{\Phi_n} \tag{7}$$

where $\Delta\Phi$ represents the water flux loss and Φ_m and Φ_n represent the water flowrates in two different systems. They are chosen in a way to yield values of water flux loss between 0 and 1. A value of zero represents no flux loss as the system is modified, while a value of 1 means total halting of water flow across the membrane.

There are two situations where this quantity is employed. The first one is in Figures 21(c)-(d) in section 3.2 where we compare the water flowrates for monolayer MoS_2 membranes between pure water systems and systems containing water and salt ions. The presence of salt ions reduces water flow and yields water flux losses in the range $0 < \Delta\Phi < 1$.

The second time we encounter this quantity is in section 4.1 in Figures 29(d)-(f), where the water flowrates for monolayer and bilayer MoS_2 membranes are compared. This quantity is now referred to as the **bilayer flux loss**. Introducing a second layer of MoS_2 significantly lowers water flow and computing the ratio in equation 7 allows us to quantify this loss.

Water Exclusion Coefficient

The **water exclusion coefficient** is employed in section 3.2. It is defined by the following equation:

$$\Delta V = 1 - \frac{N_W^{SW}}{N_W^{PW}} \tag{8}$$

where N_W^{PW} and N_W^{SW} correspond to the average number of water molecules present within the nanopore in pure water systems and saltwater systems respectively.

This quantity is always calculated within the interval defined by t_0 and t_f and is derived from the flux files for all values of applied pressure. It represents the loss in inner pore volume which is occupied by water molecules. This is caused by the presence of ions which reduce the number of water molecules that can occupy the pore and greatly affects water transport.

Ion density profile

The **ion density profile** is calculated from the trajectory files and represents the distribution of ions along the Z axis, which is divided in bins of length ΔZ. The number of ions of a given species - Na^+ or Cl^- - in each bin is calculated at timesteps contained in the interval defined by t_0 and t_f and then averaged to yield the average ion density in each bin. The results are given in the unit $ions/nm^3$.

The results used in this work were produced from simlations performed at an applied pressure of 100MPa. They allow us to identify which type of nanopores contain more Na^+ or Cl^- ions and in what regions of the pore they have a higher probability of being found. They also provide information on ion retention near the MoS_2 walls.

The ion density profile is a measurement of ion density along the Z axis, just like the PMF. It can therefore be interpreted as the inverse of a pseudo-PMF for the ions, where minima in the potential energy profile yield higher ion densities and maxima yield lower densities. The reason it does not correspond to a real PMF is that it is calculated at a non zero value of pressure gradient, and therefore does not correlate exactly with the potential energy profile as the system is not in equilibrium. This quantity can, nonetheless, provide an approximate form for the PMF of both ionic species across the system.

Passing times

Passing times quantify the amount of time a certain particle takes to travel across a certain region of the system. They appear in two occasions in this work, the first one being in section 3.3 where we calculate the passing times for Na^+ and Cl^- ions across monolayer MoS_2 nanopores to help explain ion rejection in these systems. The second time this quantity is used is in section 4.1 where we compute histograms of passing times for water molecules across the interlayer region of the bilayer MoS_2 membrane to show that both a slow and a fast mode of water transport across the membrane are present.

3 Results - Monolayer membrane

In this chapter we discuss the behavior of pure water and water + salt solutions through individual nanopores, built on an MoS_2 single-layer membrane (Q1), or in an equivalent structure with no charge distribution (Q0) or with a charge polarization two times stronger than the one usually present in MoS_2 sheets (Q2). Our aim is to evaluate the impact of charge distribution on water and ion dynamics in a system with fixed geometry. We evaluate the mobility of water through the pore at first in the absence of salt, then we provide an analysis of the effect the presence of salt ions has on water transport across the nanopores. Finally, we conclude the chapter providing an analysis of the mechanisms governing ion transport across the membrane and how they are affected by the charge polarization of MoS_2. All our analysis are carried out for nanopores of two different diameters: 0.97nm and 1.33nm. These are diameters of interest since the efective diameters of hydrated Na^+ and Cl^- ions are around 1.1-1.2nm.

3.1 Pure water system

First, we conducted simulations for the systems shown in Figure 6(a), a pure water system. We explored the contribution of charge polarization for three values of charge multiplies: no charge, Q0, the actual charge distribution of the MoS_2, Q1, and double the charge polarization of MoS_2, Q2. We also study two different pore diameters, 0.97 nm and 1.33nm. In our work we expand preliminary analysis of this system performed by Abal and Barbosa [62] by adding additional pressures and carrying out more simulation runs in order to obtain higher statistical accuracy. For each value of charge multiplier and pore diameter three values of applied pressure - 100MPa, 175MPa and 250MPa - were simulated, and for each of them four independent simulations were conducted.

The values obtained for the water flowrate in each system are displayed in Figure 15. We observe that water flux grows linearly with applied pressure. For 0.97nm pore diameter, shown in Figure 15(a), there is no water flow for Q2. This result is consistent with the findings in [62]. We also see similar flowrates for Q1 and Q0, with Q1 showing slightly higher values at higher pressures. For a 1.33nm pore diameter we find flowrates that are close in value for all charge distributions. Q0 and Q1 nanopores show equal flowrates at 100MPa, however, water flow through Q1 becomes higher as the applied pressure increases. Q2 has the lowest values of water flowrate regardless of applied pressure. Results for P=100MPa are also in accordance with [62]. It is worth noting that the 1.33nm nanopore exhibits a flowrate about 5-6 times higher than the smaller one, as has been observed in [40, 62].

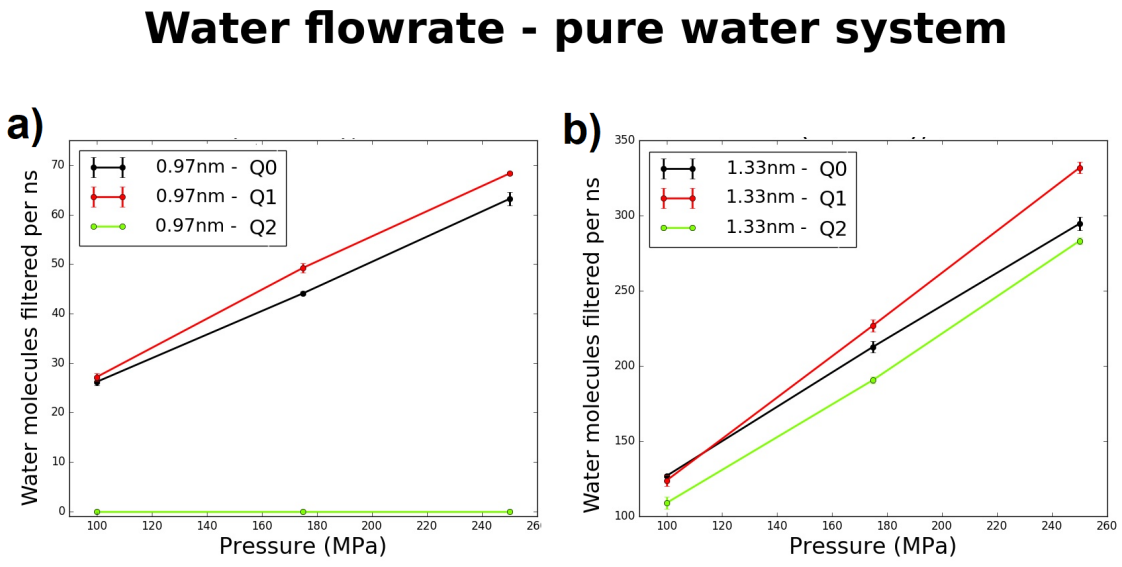

Figure 15: Water flowrate - expressed here in water molecules filtered per ns - as a function of applied pressure for pore diameters of a)0.97nm and b)1.33nm. Black, red and green lines represent charge multipliers of Q0, Q1 and Q2.

At first, we analyze the nanopores' affinity for water molecules. Figure 16 shows the average number of water molecules inside each nanopore, for different charge distributions during the simulations at an applied pressure of 100MPa. The amount of water molecules inside the pore is

a measure of the nanopore's hydrophilicity. The increase in the amount of water molecules inside the pore as the charge multiplier increases indicates that higher charge polarizations create a more hydrophilic environment. The smaller pore naturally contains a lower number of water molecules when compared with the larger pore. Once again, the overall trend of our results is in agreement with those reported in [62], however the number of water molecules contained inside the pore differs due to a different geometric criteria being used to define the inner pore region.

A comparison between Figure 15 and Figure 16 indicates that there is not a direct correlation between pore hydrophilicity and water flowrate. Although pore hydrophilicity has been shown to increase water permeation across nanopores [37, 10], additional mechanisms appear to govern water transport across them.

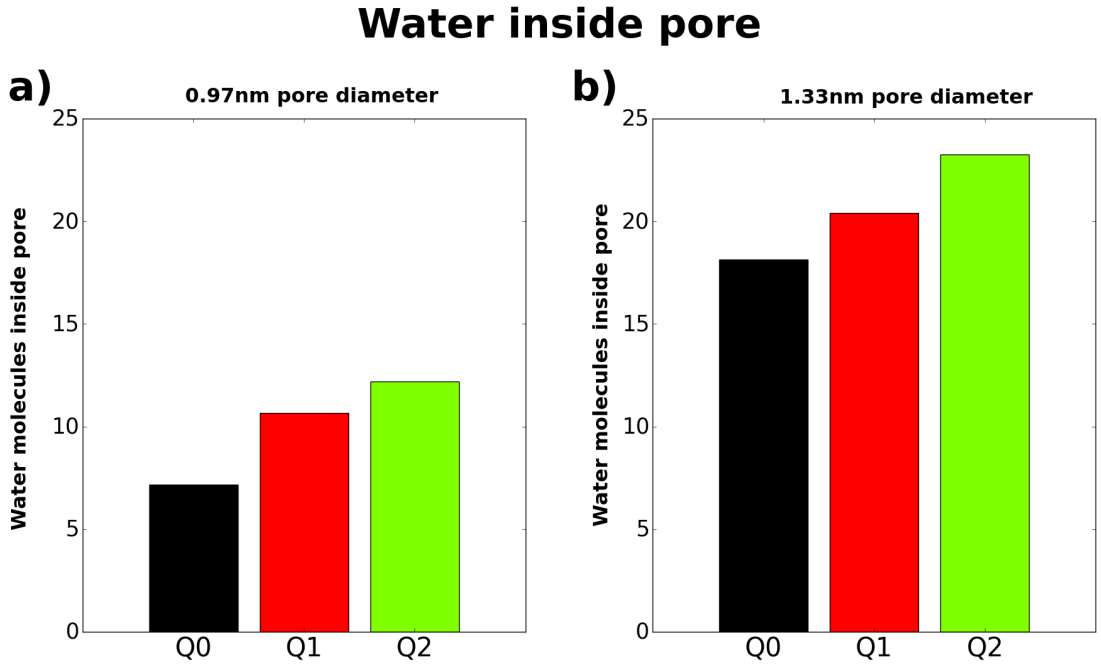

Figure 16: Mean number of water molecules inside each nanopore during production run at 100MPa for different charge distributions and for nanopores of diameter a)0.97nm and b)1.33nm.

To better understand how water molecules are distributed inside the pores we computed the oxygen density maps for each nanopore, which are shown in Figure 17. They provide the local water density across the pore's area in the plane parallel to the MoS_2 layer. The densities are computed in the inner region of the pores (between the two layers o sulfur atoms as shown in the illustration in Figure 17). Lighter colors indicate a high density of the oxygen atoms, while darker regions exhibit low oxygen density. Figures 17(a)-(c) represent color maps of the 0.97nm pores and Figures 17(d)-(f) represent the color maps of the 1.33nm pores with charge multipliers Q0, Q1 and Q2 respectively. Yellow and pink dots represent sulfur and molybdenum atoms respectively and equal range color bars were used for all pores. The obtained maps are similar to those obtained in [62].

There is a similar trend being followed by both the 0.97nm and 1.33nm diameter pores, where water molecules are located primarily in the central region of the pore for Q0, but as charge polarization increases, higher and higher amounts of waters are accommodated near Mo atoms. This is caused by coulombic attraction between Mo and oxygen atoms, which exhibit positive and negative partial charges respectively.

We can now see clearly what happens to water inside the 0.97nm/Q2 pore, where oxygen atoms are highly concentrated around Mo atoms. The water inside the pore is so rigidly confined to the Mo-terminated edges of the nanopore that the molecules become stuck to it, which compromises the formation of hydrogen bonds, as they are too far apart and have limited movement. In the 1.33nm pore we can see that charge polarization still plays a crucial role in the structuring of water within it and leads to layered organizational patterns of molecules, especially for Q2. However, even for Q2 electrostatic forces are incapable of significantly breaking down the hydrogen bond network, which explains the proximity of water flowrate values of 1.33nm pores for all three charge multipliers.

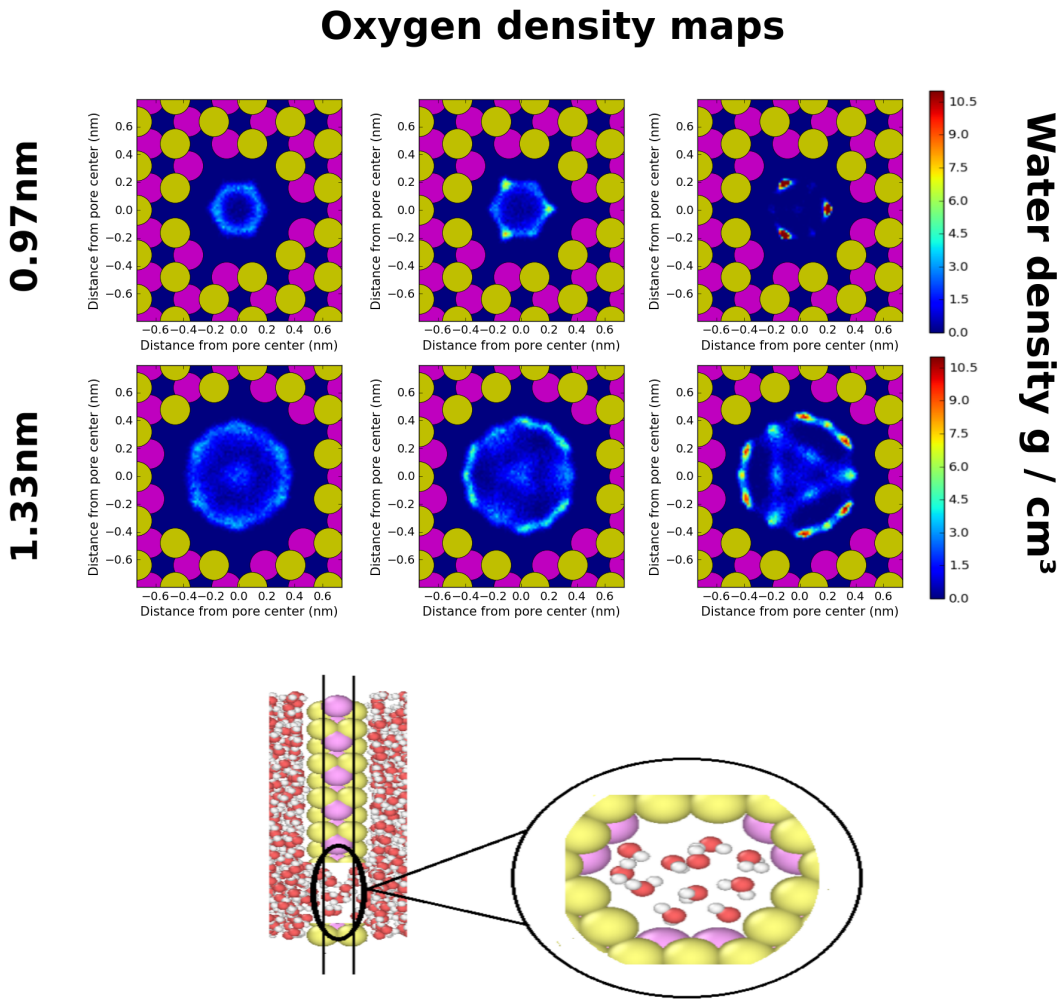

Figure 17: Oxygen density maps inside the pores. 0.97nm diameter pores are represented in the top section with charge multipliers of a) Q0, b) Q1 and c) Q2 and 1.33nm diameter pores are shown in the lower section with charge multipliers of d) Q0, e) Q1 and f) Q2. Sulfur and molybdenum atoms are represented by yellow and pink circles respectively.

The water distribution patterns shown in Figure 17 imply the existence of interconnected water structures inside the pores, and in order to better understand this phenomenon we computed the orientation of water molecules within it. Strong electrostatic interactions between MoS_2 and water molecules inside the pores can limit the possible orientations of water molecules. We conducted an analysis of the angle of the water dipole vectors with respect to the Z axis. Details on this measurement are given in section 2.6. Results are given in Figure 18(a)-(b) for the 0.97nm and 1.33nm nanopores respectively. The dotted lines represent the mean angle of orientation of water molecules in relation to the Z axis, while the shaded regions above and below it represent one standard deviation from the mean value. We can see that adding a charge distribution to the nanopore adds a constraint to the orientation of the water molecules, which is proportional to the magnitude of the charge polarization. For both nanopores it can be seen that the Q0 pores show little restriction to the allowed orientations of water molecules. That allows water molecules to flow through the pore more easily, increasing the flowrate. As charge polarization is introduced to the system there is a smaller pool of permitted orientations for water molecules, which causes them to have to rotate to cross the pore. This angular constraint will certainly impose resistance to the passage of water and reduce flowrate through the nanopore.

The effect of charge polarization in the 0.97nm diameter pore is more pronounced than for the 1.33nm diameter one. This happens because in the samller pore most water molecules are located near Mo and S atoms where electrostatic interactions are more intense. We see that the 0.97nm/Q2 limits the orientation of water molecules in such an extreme way that it impedes its movement to other parts of the nanopore, as large rotations become necessary for very small displacements, which reflects the freezing of water molecules inside it seen in Figure 15(a) and 17(c). For the 1.33nm pore we can see that even though Q1 and Q2 limit the allowed orientations of water

molecules its effect is much more mild. This indicates that the angular constraint still plays a role in the flowrate, partially explaining its reduction for the Q2 pore, it is, however, not strong enough to compromise water flow through the Q1 pore, which exhibits equal or slightly larger flowrate than Q0 depending on the applied pressure. A similar conclusion can be drawn for the 0.97nm diameter pore, as the Q1 pore exhibits higher flowrate than Q0 despite its higher restriction in water molecule orientation. Our results are also in accordance with those in [62].

The orientation of water molecules in the nanopore region is determined by the liquid charge of molybdenum atoms. This is evident in Figures 18(c)-(d) where we calculated the orientation of water molecules for a charge polarization of intensity -1 (Q(-1)). This MoS_2 membrane has negatively charged molybdenum atoms and positively charged sulfur atoms, while still mantaining overall charge neutrality. The inversion in the partial charge of Mo atoms led to an equivalent inversion in the angular distribution of water inside the pore. This can be easily understood by the way in which partial charges are distributed in MoS_2. Individual molybdenum atoms have partial charges that are twice as high in absolute value as those of sulfur atoms. That in turn leads to oxygen atoms experiencing high attractive forces to the Mo atoms once they approach the entrance or exit of the pore and also while traveling inside of it. Sulfur atoms do not attract the hydrogen atoms of water or repel oxygen atoms as strongly, leading to the profiles obtained in Figure 18. Water molecules will thus enter the pore with oxygen atoms first and hydrogen atoms afterwards. Once charge polarization is reversed, the now negative Mo atoms attract water molecules hydrogen-first, explaining the inversion in the water dipole orientation curves.

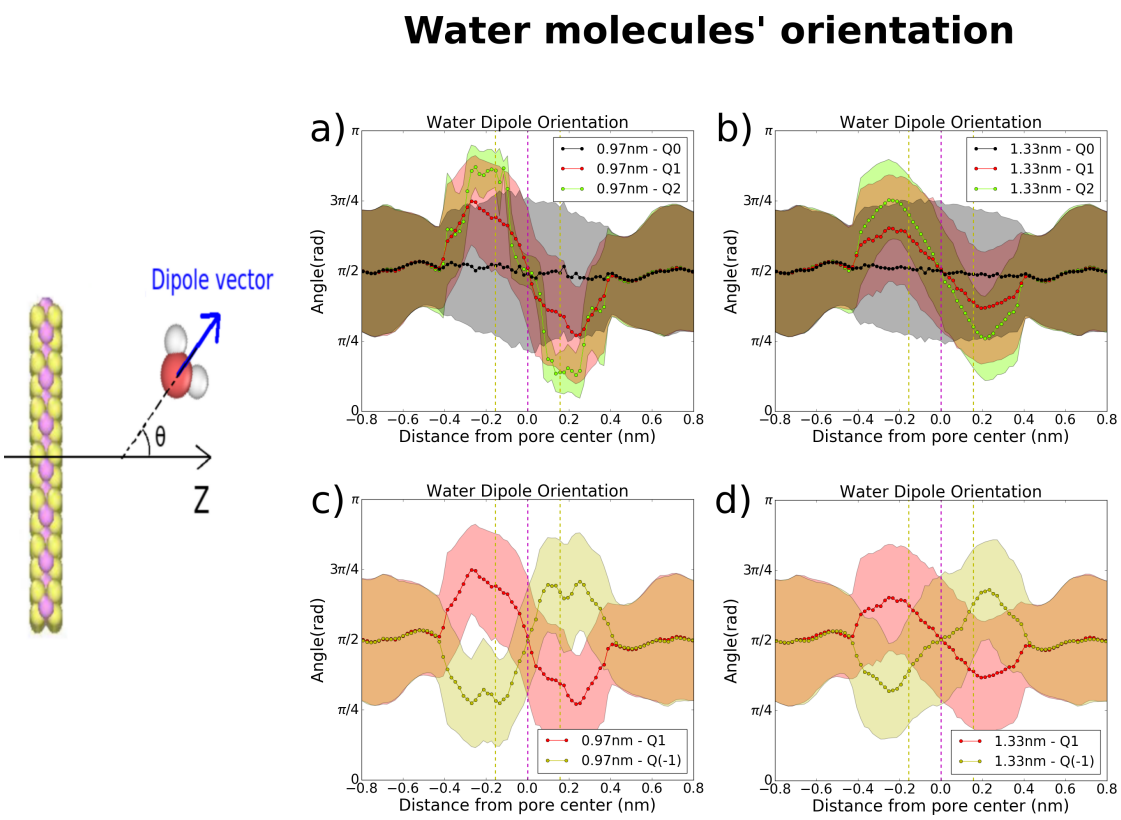

Figure 18: Top: Water molecules' orientations at different charge multipliers near nanopores of diameter a) 0.97nm and b) 1.33nm. Bottom: Water molecules' orentations at charge multipliers Q1 (red) and Q(-1) (yellow) for nanopores of diameter c) 0.97nm and d) 1.33nm. The vertical dashed lines represent the positions of sulfur (yellow) and molybdenum (purple) atoms.

We showed that water molecules are attracted to the pore by the partial charges of Mo, which should increase water transport, however, an excess of it causes a decrease in the flowrate due to the strong attraction of water molecules towards the Mo terminated edges of the pores.. Next, we analyzed the potential energy barriers and the distribution of hydrogen bonds along the direction of water flow (Z axis) which, alongside water molecules' orientation (see the Figure 18) influence how water molecules travel across MoS_2 nanopores.

In order to understand water mobility through the nanopores we analyzed the local density of water molecules in and around the pores in the absence of applied pressure, with only 1atm

applied to both pistons. We then computed the potential of mean force (PMF) for water molecules in the direction of water flow (Z direction), which is shown in Figures 19(a)-(b) for the 0.97nm and 1.33nm pores respectively, using the equation:

$$PMF(z) = -k_b T log(\frac{\rho(z)}{\rho_0}) \ . \tag{9}$$

where k_b is the boltzmann constant and T is the system's temperature in Kelvin. The PMF is expressed in the unit kcal/mol.

We can see in Figures 19(a)-(b) that the disturbances in the system caused by charge polarization of the membrane are highly localized and become negligible at distances over 0.4nm away from the center of the nanopore. The potential energy barrier for the 0.97nm diameter pore is higher than that of 1.33nm diameter ones, regardless of charge multiplier. This is caused by the smaller volume within the 0.97nm pore, which leads to a lower amount of water molecules accommodated within it (see Figure 16).

In Figure 19(a) we display the PMF for the 0.97nm nanopore. We can see that a charge multiplier of Q2 yields a PMF with very pronounced peaks, reflecting the highly localized distribution of water, exhibiting lower potential energy near molybdenum and extremely high values near sulfur atoms. The potential energy barrier is also too high to allow for the flow of water molecules through the pore, which leads to the formation of a frozen-like water structure inside the pore. It is also noticeable that the potential energy barriers for Q0 and Q1 have similar heights, which explains the similar values of water flowrate in both cases, with that of Q0 being slightly higher, which contributes to its slightly lower flowrate.

Figure 19(b) gives the PMFs for the 1.33nm diameter nanopore. It indicates that all three charge multipliers lead to pores with potential energy barriers of similar heights, which is consistent with the findings in Figure 15(b) which shows flowrates that are closer in value regardless of the charge multiplier. The difference between flowrates is small but not negligible, and it can not be explained by the PMF in this case.

One last important observation to be taken from the PMFs is that a decrease in charge polarization inside the pore from Q2 to Q1 flattens the PMF. This can only be explained by the presence of a competing force that counteracts the hydrogen bond network of water molecules. This competing force comes from the water-MoS_2 electrostatic interactions and will be discussed next in more detail. The smoother profile for Q0 in both pores is due to the lack of these electrostatic interactions with the molybdenum and sulfur atoms located at the pore's edges. That leads to a more uniform distribution of water molecules within it, since they are now only subjected to geometric constraints related to the nanopore's shape.

Since charge polarization inside the nanopore strongly influences the spatial distribution of water molecules, we can expect it to cause disturbances in the hydrogen bond network, given that hydrogen bonds are highly directional, and only form if two water molecules are positioned within a restricted subset of spatial configurations from each other (see section 2.6). We plotted in Figures 19(c)-(d) curves that represent the average number of hydrogen bonds per water molecule form inside or in the vicinity of the pores. They give us an idea on how the hydrogen bond network varies as it travels across the pores.

We can see in Figure 19(c) that for the 0.97nm pore there is a decrease in the mean number of hydrogen bonds formed by water molecules located around the central layer of the pore. This effect is visible even for the Q0 pore, indicating that there is a geometric constraint caused by the narrowing of the nanopore's cross section which limits hydrogen bond formation. For Q1 we see a higher reduction in the number of hydrogen bonds per molecule throughout most of the pore's length and for Q2 we observe an extreme distortion in the hydrogen bond network, which is more dramatic near the center of the pore. This is what causes the total blockage of the 0.97nm/Q2 pore, as water molecules are now strongly attached to Mo terminations inside the pore and are incapable of forming enough hydrogen bonds to be released.

In the 1.33nm diameter pore we see more subtle changes to the hydrogen bond network, which can be seen in Figure 19(d). The Q0 pore now indicates only a very slight decrease in the number of hydrogen bonds near the central layer, reflecting the pores larger volume. As charge polarization is introduced, the curves follow the same pattern seen in the 0.97nm diameter pore of breaking up hydrogen bonds due to water-MoS_2 electrostatic forces. We do not see the dramatic rearangement of the hydrogen bond network for Q2 that we saw it in the 0.97nm pore. This happens because the pore is now big enough that water molecules near the center of the pore are far enough from the pore's edges that electrostatic forces can not breakdown their hydrogen bonds. These central waters in turn help pull away the water molecules that may become "glued" to the Mo-terminated edges due to coulombic attraction.

It is also worth noting that minima and maxima of the hydrogen bond profiles in Figures 19(c)-(d) correlate fairly well with the extrema in Figures 19(a)-(b). That indicates that the electrostatic

forces attracting water molecules towards the nanopore are the same forces breaking up hydrogen bonds within the nanopore. This suggests the existence of a correlation between hydrophilicity and hydrogen bond breakdown within the pore, with more hydrophilic regions of the pore exhibiting water molecules forming less hydrogen bonds. This can be easily explained by the aforementioned competition between water-MoS_2 electrostatic forces and the cooperative forces between water molecules represented by the hydrogen bond network.

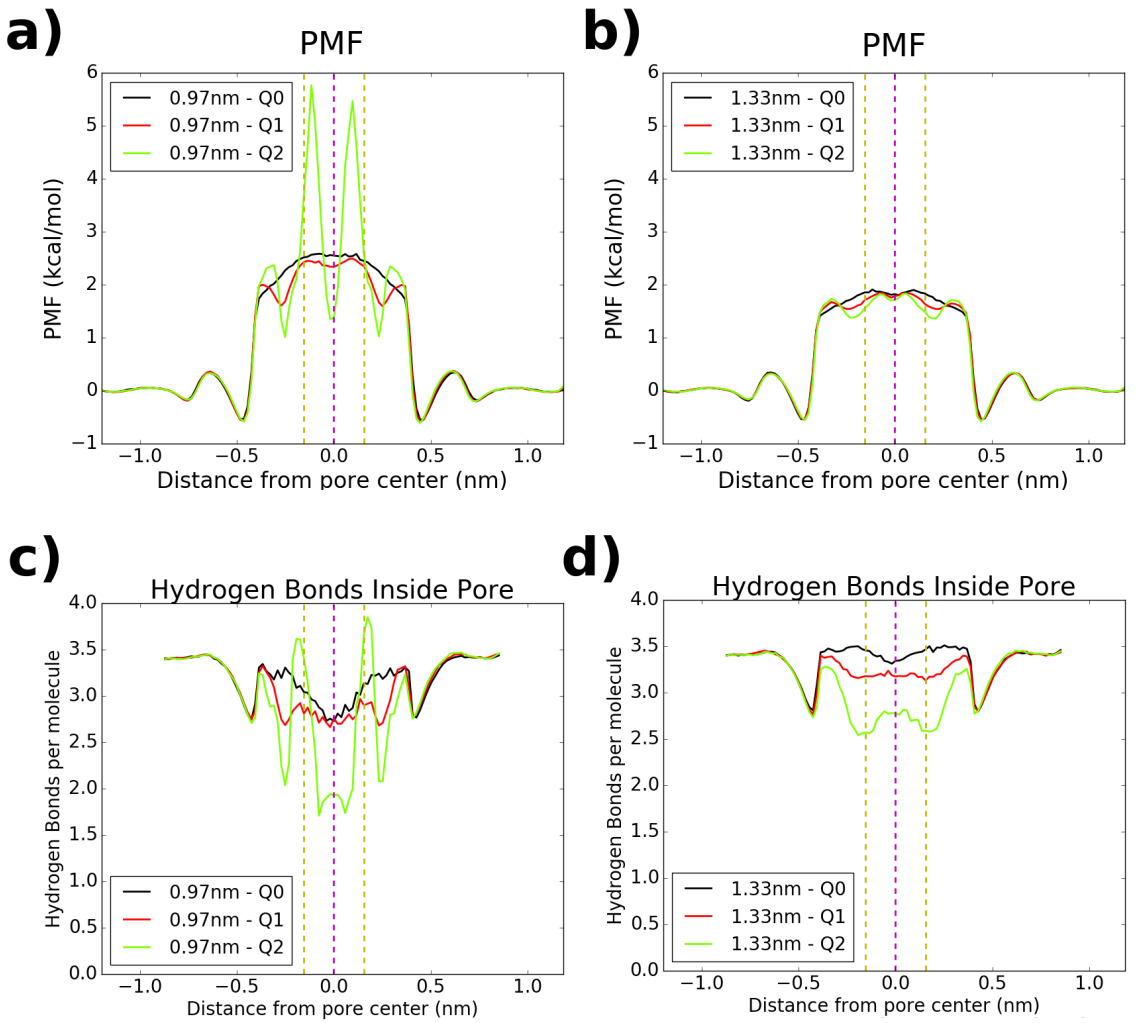

Figure 19: Top: Potential of mean force for nanopores of diameter a) 0.97nm and b) 1.33nm. Bottom: hydrogen bonds per water molecule along the Z direction for c) 0.97nm and d) 1.33nm pore diameters.

The water transport mechanism in the nanopores involves competition between water-MoS_2 electrostatic forces between and cooperative forces coming from hydrogen bonds between water molecules. The same electrostatic forces which attract water molecules towards the pore and increase its hydrophilicity also pull water molecules towards the edges of the pores and its attractive nature can cause a slowdown in the flow of water molecules. Beyond that, charge polarization inside the nanopore can also limit water flow by introducing an angular constraint to the orientation of water molecules, which forces them to rotate in order to travel through the pore, hindering water flux. Water molecules inside smaller pores are more strongly affected by electrostatic forces as most molecules are close to the pore edges and less molecules can enter the pore to form hydrogen bonds and counter act such forces.

All these factors compete with each other to determine the water flowrate of each nanopore. The most efficient nanopore will be that which optimizes the tradeoff between higher hydrophilicity and increased destructive electrostatic forces with the pore edges. Results in Figure 15 indicate that the best choice is likely the Q0 or Q1 pore. While they show nearly identical water flowrates for P=100MPa, Q1 has a slight edge over Q0 as applied pressure increases. It could be that pressures above 100MPa are high enough to push the water molecules near the pore edges away from the pore region by beating the water-MoS_2 electrostatic forces, or it could be the case that

hydrophobic pores behave differently in relation to applied pressure. The fact is that the water flowrate curve as a function of applied pressure for Q0 has a different slope than that of Q1 and Q2. This is, however, beyond the scope of this work and further analysis would be necessary to better understand this.

To further validate our proposed mechanism we performed simulations of a hypothetical nanopore Q3 with a diameter of 1.33nm. As the identifier suggests, Q3 refers to the case where the charge polarization of a regular MoS_2 membrane is tripled. We performed three simulations for said pore, only for an applied pressure of 250 MPa, and the obtained value for the water flowrate is shown in Figure 20(a). There is a drastic decrease in the water flowrate, which is caused by the electrostatic forces becoming strong enough to break down a large number of hydrogen bonds. That is shown in Figure 20(f), where the average number of hydrogen bonds per molecule along the Z axis is now greatly affected by charge polarization, exhibiting an oscillating behavior with high amplitude similar to that observed for the 0.97nm/Q2 pore in Figure 19(c). We can also see very clearly in Figure 20(d) that a large fraction of water molecules are now highly concentrated around Mo atoms, just like what happened for the 0.97nm/Q2 pore in Figure 17(c). The breakdown of hydrogen bonds is also reflected in Figure 20(e), where it becomes clear that increasing the charge multiplier from Q2 to Q3 significantly restricts the allowed orientations of water molecules inside the pore. The reason water flow isn't completely halted for the 1.33nm/Q3 pore is that water molecules can still pass through the center of the pore somewhat unimpeded due to the pore's larger diameter. This is an extreme case, and, just as was seen for the 0.97nm pore, the contribution coming from the high hydrophilicity of the 1.33nm/Q3 pore, demonstrated by Figure 20(b), is surpassed by that of the increased strength of the electrostatic forces which break down the hydrogen bond network and lead to a very low water flowrate.

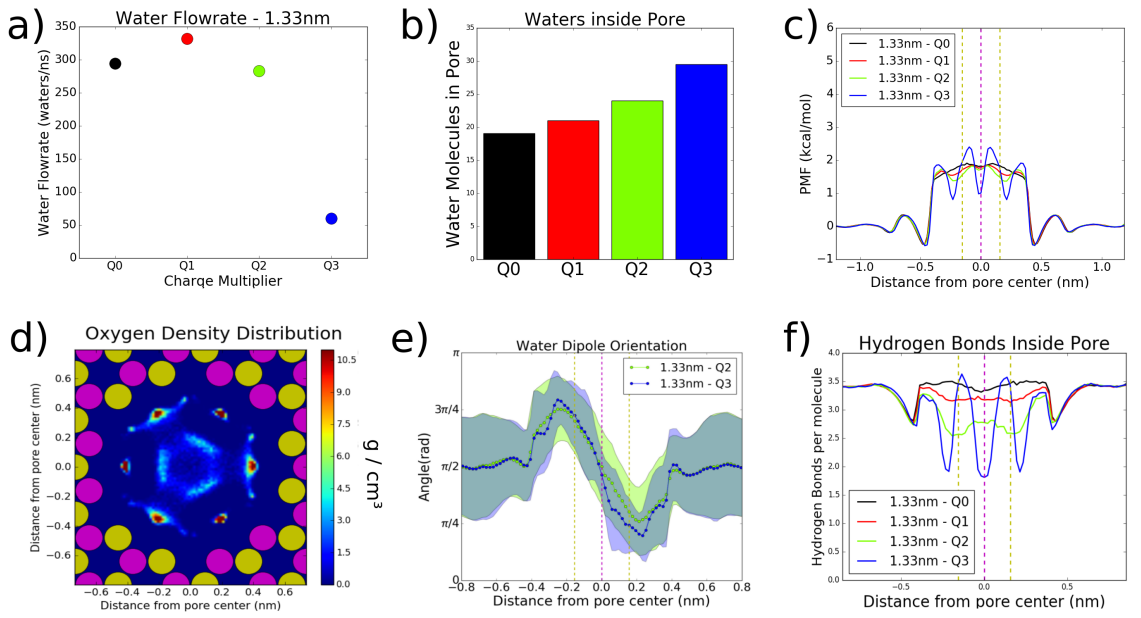

Figure 20: Analysis of the 1.33nm/Q3 nanopore. a) Comparison between water flowrates for 1.33nm diameter pores with charge multipliers Q0, Q1, Q2 and Q3 obtained at P=250MPa. b) Comparison between average number of water molecules contained within 1.33nm nanopores with charge multipliers Q0, Q1, Q2 and Q3. c) PMF of 1.33nm pores with charge multipliers of Q0, Q1, Q2 and Q3. d) Oxygen density map for the 1.33nm/Q3 pore, yellow and pink circles represent Sulfur and Molybdenum atoms. e) Angular orientation distribution of water molecules along the nanopore for 1.33nm/Q2 and 1.33nm/Q3 pores. f) Hydrogen bonds per molecule along the Z axis in the 1.33nm diameter nanopore for charge multipliers Q0, Q1, Q2 and Q3. Dashed yellow and purple lines in c), e) and f) represent the position of sulfur and molybdenum atoms respectively.

3.2 Water transport in MoS_2 nanopores in the presence of salt ions

In the previous section we provided a detailed analysis on the mechanisms regulating water transport across the nanopores. We now introduce salt ions into the system to simulate an actual desalination process. Before determining the mechanisms behind salt rejection we will focus, in this section, on understanding how the presence of ions in the system impacts the water flowrate.

Figure 21(a)-(b) shows the water flowrate as a function of applied pressure obtained during the

simulations for the 0.97nm and 1.33nm diameter pores. For all systems at all values of applied pressure there has been a reduction in the water flowrate caused by the presence of salt ions. The Q0 nanopores now have a water flowrate higher than the Q1 nanopores for both pore sizes, unlike in Figure 15 where Q1 had a slightly higher flowrate in pure water simulations, particularly at higher pressures. Something odd happens for the 1.33nm/Q1 nanopore, where its water flowrate is considerably lower than that of 1.33nm/Q0 for pressures of values 100MPa and 175MPa, however at P = 250MPa both pores exhibit nearly identical flowrates, deviating from the linear dependence of flowrate on applied pressure.

To better visualize the changes in flowrate caused by the presence of salt in the system we plotted in Figures 21(c)-(d) a quantity we called water flux loss ($\Delta\Phi$), which is defined by the formula:

$$\Delta\Phi = 1 - \frac{\Phi_{SW}}{\Phi_{PW}} \tag{10}$$

where $\Delta\Phi$ represents the water flux loss, Φ_{SW} the water flowrate in salt + water systems and Φ_{PW} for pure water systems. A water flux loss of zero represents no loss in water flow as ions are introduced into the system and a water flux loss of 1 represents complete halting of the flow of water through the nanopore. It can be seen in Figures 21(c)-(d) that the water flux loss increases as we increase the charge polarization inside the nanopores. It is also worth noticing that the water flux loss for the 1.33nm/Q1 stands out as an outlier among the other values. While the quantity appears to be more or less constant for the 1.33nm pore, regardless of applied pressure, we see that for P=250MPa there is a drop in the value of water flux loss for Q1, indicating that something unexpected is happening.

Figures 21(e)-(f) show the average number of ions inside the nanopores during the simulations as a function of applied pressure. We can see that as charge polarization inside the pore increases, so does the average number of ions inside it. An increase in the applied pressure also leads to a higher amount of ions being present in the nanopores. The one exception to this trend is the point corresponding to the 1.33nm/Q1 pore at 250MPa, where an increase in pressure leads to a decrease in the average number of ions inside the pore. Figures 21(e)-(f) follow a nearly identical pattern as that of Figures 21(c)-(d), suggesting a strong correlation between ion obstruction of the pore and water flux loss.

This correlation can be explained by a simple geometric argument: as more ions occupy the inside of the pore, less of the pore's volume can be occupied by water. As less water can enter the pore, the water flowrate will tend to decrease. To quantify this phenomenon we defined a quantity called the water exclusion coefficient. This quantity is defined by the formula:

$$\Delta V = 1 - \frac{N_W^{SW}}{N_W^{PW}} \tag{11}$$

where ΔV represents the water exclusion coefficient, N_W^{SW} represents the average number of water molecules inside the nanopores in a salt + water system and N_W^{PW} the same thing but in a pure water system.

This coefficient allows us to measure the fraction of water molecules on average that must leave the nanopore due to the entrance of salt ions. It also allows us to compare results for both the 0.97nm and 1.33nm diameter pores which have different inner pore volumes. The results for the coefficients are given as a function of applied pressure in Figures 21(g)-(h). We can see that the coefficient increases with the intensity of the charge polarization of MoS_2. The coefficient is negative for 0.97nm/Q0 at 250MPa, but that does not necessarily mean that more water is present inside the pore when salt ions are present, as the error bar covers the value of zero. We can also see that the results look very similar to those obtained in Figures 21(e)-(f), indicating that the decrease in the average number of water molecules inside the pores is indeed caused by the presence of ions. Some points present particularly large error bars, this is caused by statistical variation in the mean number of ions present inside the pores at each independent simulation run, which therefore impacts the mean number of water molecules present inside it.

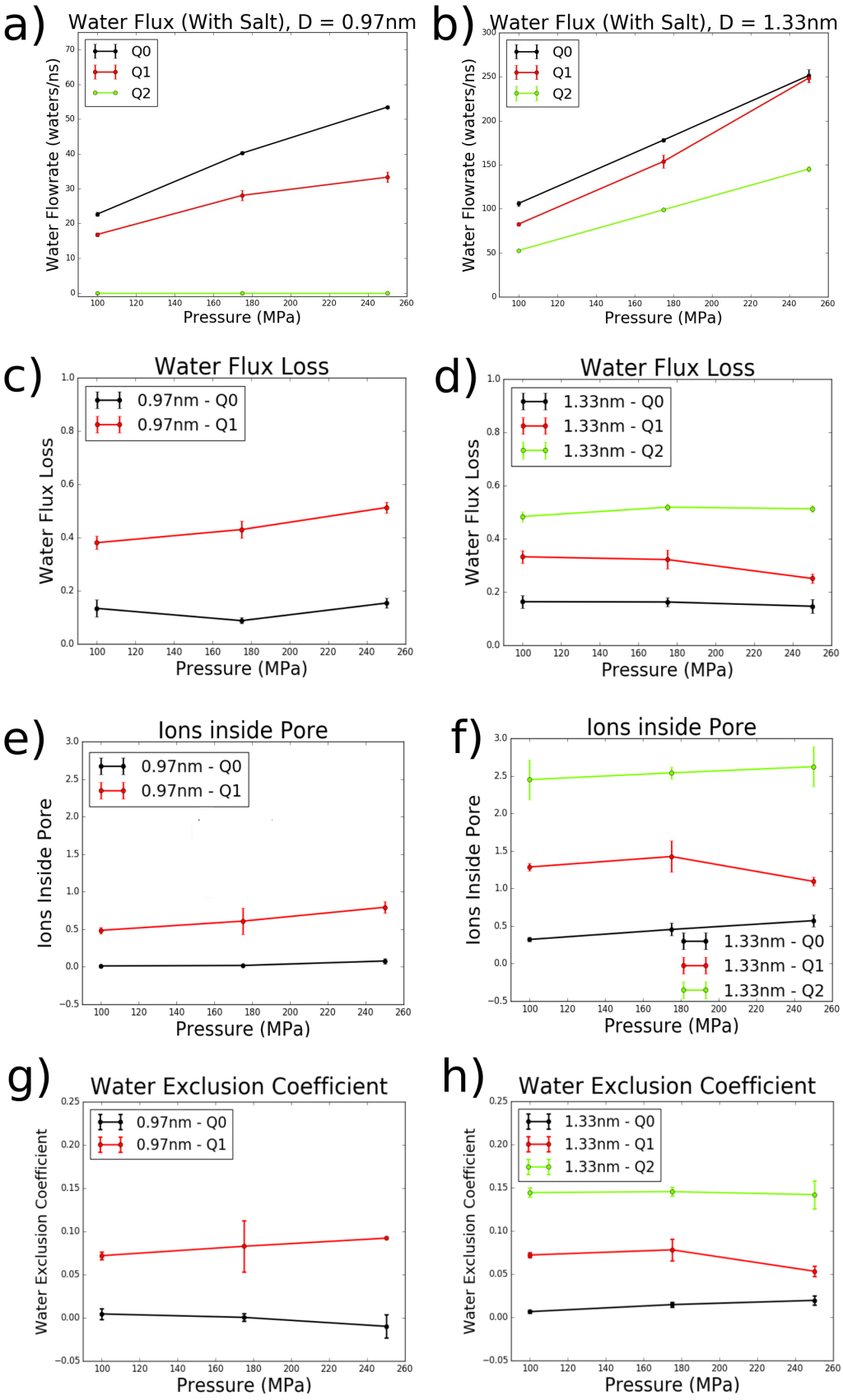

Figure 21: Water flowrate expressed in molecules filtered per ns for differente charge distributions and pore diameters of a) 0.97nm and b)1.33nm when salt ions are present in the system. Water flux loss as a function of applied pressure for c) 0.97nm and d) 1.33nm diameter pores. Average number of ions inside each nanopore as a function of applied pressure for e) 0.97nm and f) 1.33nm diameter pores. Water exclusion coefficient as a function of applied pressure for all values of charge multiplier and pore diameters of g) 0.97nm and h) 1.33nm.

Figure 21 indicates the existence of a strong correlation between the reduction in water flowrates

and the average number of ions inside the pore. We can therefore expect there to be a correlation between the water flux loss and the water exclusion coefficient. This assumption is confirmed by Figure 22, where we plotted the water flux loss as a function of the water exclusion coefficient and a very clear linear correlation can be seen.

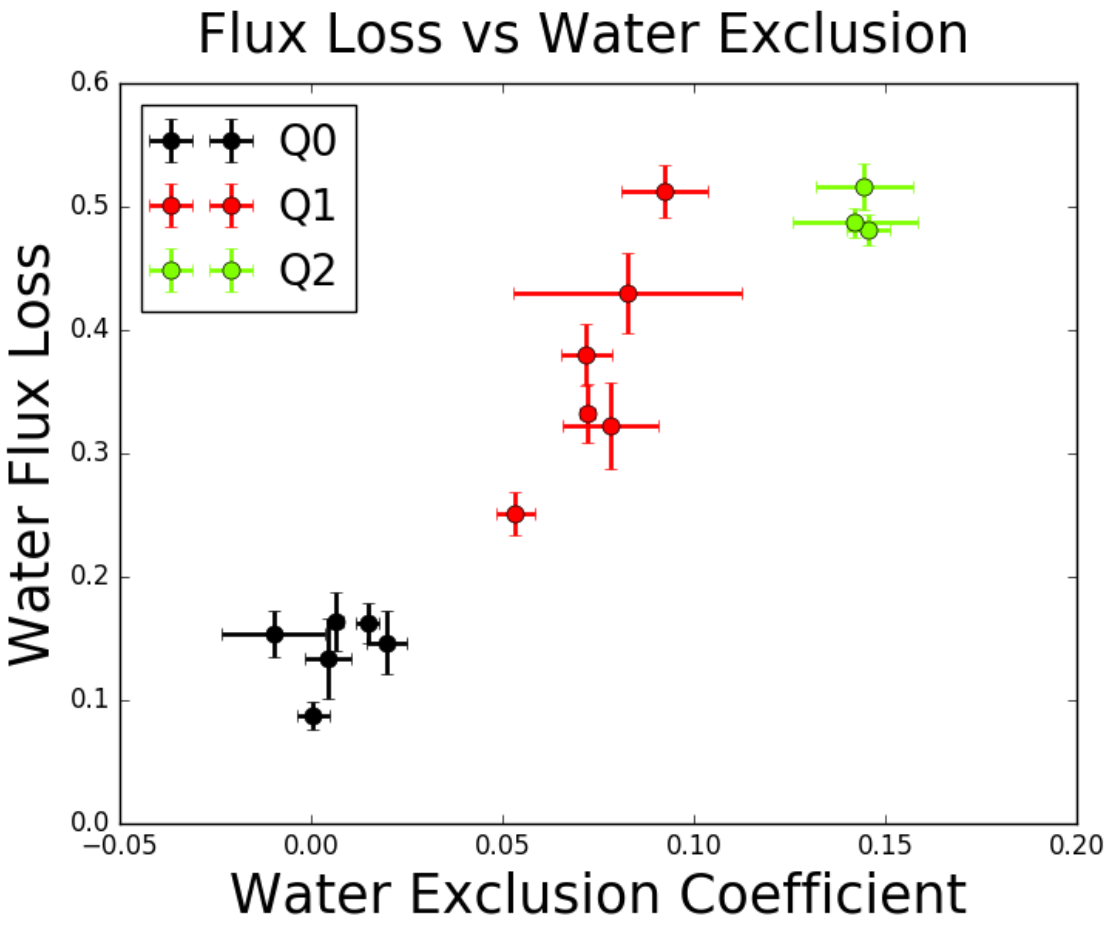

Figure 22: Water flux loss as a function of the water exclusion coefficient.

We have demonstrated that a reduction in the available volume within the nanopore that can be filled by water is caused by the presence of salt ions. This is a main contributor to the lowering of water flowrates observed as we move from a pure water system to a salt + water one. It is, however important to highlight the complexity of this process: due to the charge polarization present at the pore edges, water molecules and salt ions will not be homogeneously distributed within the pore. This was shown for the case of water in Figure 17 in section 3.1.

In order to visualize the spatial distribution of ions inside the nanopore we plot the ion density maps for Cl^- and Na^+ ions. The results are given in Figure 23 for both pore sizes and ionic species. Different colorbars had to be used for the maps to assure proper visualization of the results, due to the high discrepancy in the amount of ions of each type that enter each nanopore.

For the 0.97nm diameter pores we see that when charge polarization is not present (Figures 23(a) and (c)), both Cl^- and Na^+ ions are distributed smoothly across the pore's cross section. When we move to the Q1 pore (Figures 23(b) and (d)) we see a sharp change in behavior due to the presence of electrostatic forces between MoS_2 and salt ions. The Na^+ ions are now concentrated around the center of the pore, and the Cl^- ions are confined to very narrow regions in the neighborhood of molybdenum atoms. The distribution of Cl^- ions appears to be more sensitive to the value of the charge multiplier than that of the Na^+. A side by side comparison of Cl^- ion density and oxygen density for the 0.97nm/Q1 pore is given in Figures 23(k) and (m). It becomes evident that the sites containing a higher density of Cl^- ions coincide with sites containing high water densities. This is not surprising when we consider that both oxygen atoms in water and Cl^- ions are negatively charged.

For the 1.33nm pore we once again see ions more smoothly distributed inside the pore for Q0 (Figures 23(e) and (h)). As charge polarization is increased their distributions tend to become more localized. The Cl^- ion maps show a much higher sensitivity to charge polarization than

Na^+, something that was also observed for the 0.97nm diameter pore. As the charge multiplier increases, Cl^- ions move closer to the Mo terminations of the pore (Figures 23(i)). Once the charge polarization of regular MoS_2 is doubled (Q2), Cl^- ions show an extreme degree of spatial localization (Figure 23(j)), indicating very strong electrostatic interactions with the pore's edge. We once again, in Figures 23(l) and (n), encounter a situation where Cl^- ions are occupying sites within the pore that are usually occupied by water molecules.

The ion density maps indicate that the reduction in the amount of water molecules inside the pores that is caused by the presence of ions is not purely determined by a reduction in the effective inner volume of the pores as more ions become present within it. Cl^- ions tend to occupy sites that are more energetically favorable for water molecules. Therefore, Cl^- ions inside the pores not only decrease the overall available pore volume that can be occupied by water molecules, they also compete for the regions of the pore that can pack the highest water densities.

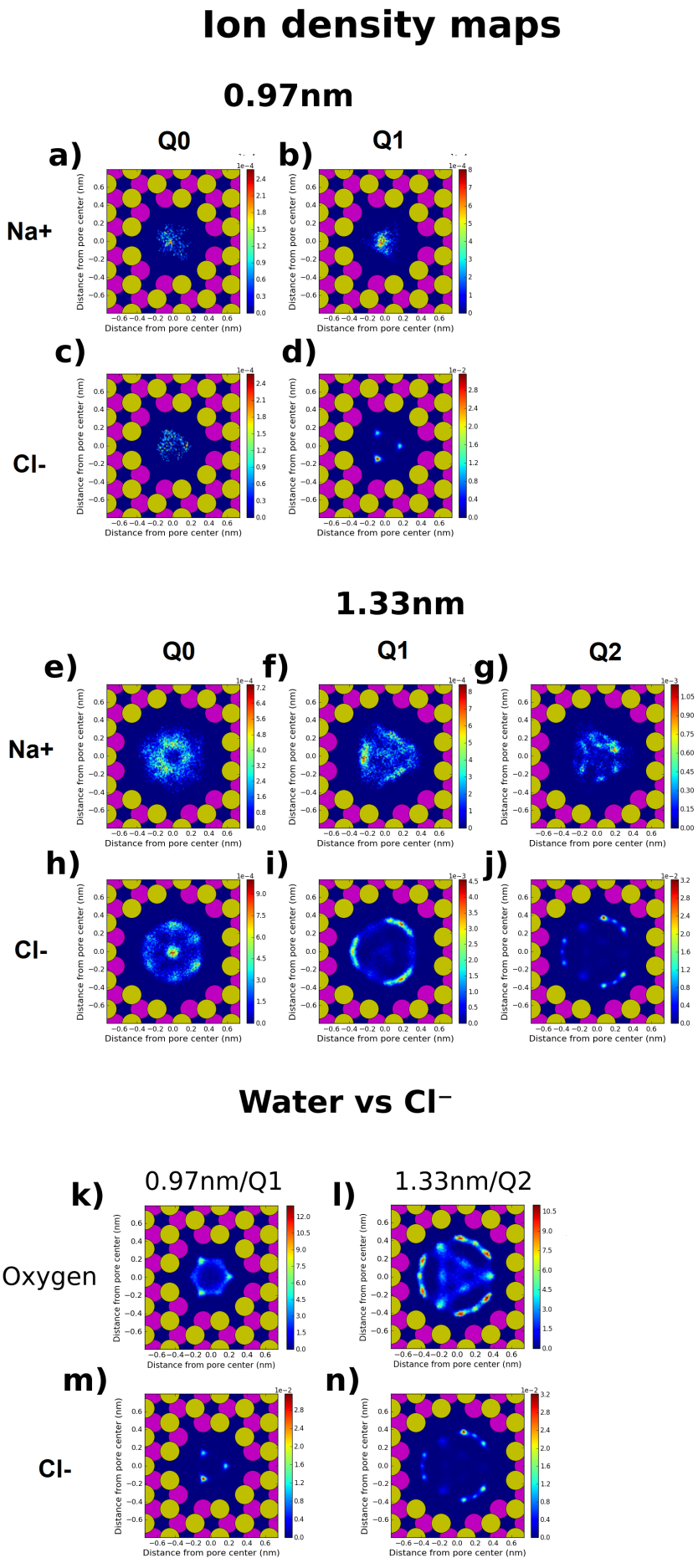

Figure 23: Ion density maps for ions traveling across the nanopores. (a)-(d) refer to 0.97nm pores, (e)-(j) to 1.33nm pores. Subplots (k)-(n) provide a comparison between (k)-(l) oxygen and (m)-(n) Cl^- density maps for two selected pores. Pink circles represent Mo atoms, while yellow ones represent S atoms.

Before we conclude this section, we present one last refinement that can be made to our understanding of how the presence of salt ions slows down the flow of water across MoS_2 nanopores. The ion density maps in Figure 23 showed that Cl^- ions tend to occupy regions of the nanopore that exhibit the highest water concentrations, especially when charge polarization is present, while Na^+ ions, althought still affected by electrostatic interactions with MoS_2, are more smoothly distributed across the cross section of the pore. It becomes therefore important to quantify the ratio between both ionic species present in the nanopores.

This ratio is given in Figures 24(a)-(b), plotted as a function of the charge multiplier, where blue bars represent the fraction of Na^+ ions present in each nanopore, while yellow bars represent the fraction of Cl^- ions. These ratios were calculated from simulations conducted at 100MPa of applied pressure, since the value of applied pressure showed little impact on the obtained values. We observe similar behavior for both the 0.97nm and 1.33nm diameter pores. When no charge polarization is present, there is a roughly equal probability of finding either a Cl^- or Na^+ ion within the pore. However, as charge polarization is introduced we observe a much higher concentration of Cl^- ions.

This result is very significant, since we just demonstrated that Cl^- ions compete with water for energetically favourable sites within the nanopore. Therefore, higher concentrations of Cl^- ions will lead to a higher water exclusion coefficient, not only due the increased presence of ions inside the pore, but also as a consequence of increased competition between water molecules and Cl^- ions for the ocupation of energetically favourable sites within the pore.

The phenomenon behind the apparent affinity of electrically polarized nanopores for Cl^- can be easily understood by analyzing Figures 24(c)-(d), which present the same ionic ratio measurements for Q1 pores given in 24(a)-(b), but now measured at 250MPa. We also display the same quantity for invertly polarized pores Q(-1), which were already mentioned in the previous section in Figures 18(c)-(d), and present negatively charged Mo and positively charged S atoms. We observe that the sets of bars for Q1 and Q(-1) pores are almost mirror imeages of each other, with inverted fractions of Cl^- and Na^+ ions. In the same way the partial charges of molybdenum atoms determined the orientation of water molecules entering the pore in Figure 18, they also determine the pore's preference for cations or anions. This can be equally explained by the fact that the partial charge of Mo atoms is twice that, in modulus, of sulfur atoms. Therefore, electrostatic forces between molybdenum atoms and ions dominate over those with sulfur, favouring the entrance of ions of charge opposite to that of Mo atoms.

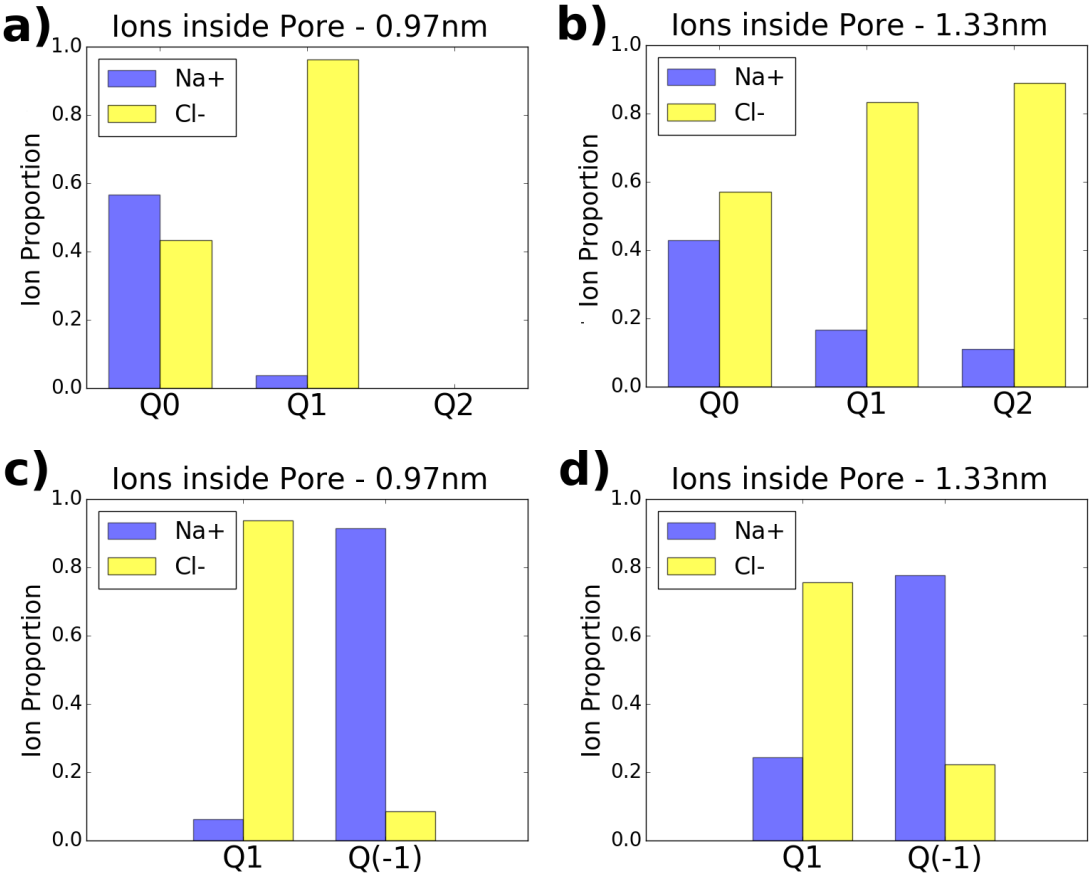

Figure 24: Top: ratio between Na^+ and Cl^- ions inside the a) 0.97nm and b) 1.33nm diameter pores, measured at P = 100MPa for Q0, Q1 and Q2. Bottom: same measurements but for Q1 and Q(-1) - inverted charge polarization - charge multipliers for c) 0.97nm and d) 1.33nm diameter pores, both measured at 250MPa. Yellow and blue bars represent Cl^- and Na^+ ions.

We showed in this section that systems containing salt + water solutions exhibit different values of water flowrate than pure water systems. Pores of all sizes and charge multipliers showed a reduction in water flux, but not at the same rate. We computed the water flux loss to show that, the more polarized the charge distribution of MoS_2 is, the higher will be the reduction in the water flowrate. We demonstrated that, as a rough approximation, this can be understood as a simple geometric phenomenon caused by an increased presence of ions inside the pore, accompanied by a decreased available volume that can be filled by water molecules, which in turn leads to lower water fluxes. By studying the distribution of each ionic species inside the pores we offered a refinement of the proposed mechanism, showing that Cl^- ions tend to compete with water for the same high density occupancy sites within polarized nanopores. Finally, we demonstrated that this phenomenon is exacerbated by the increased number of Cl^- atoms located inside the pores once charge polarization is present. Our analysis is by no means exhaustive, as we ignored many other phenomena, such as the effects of salt ions in the hydrogen bond network, the PMF or to the orientation of water molecules within the nanopores. The anomalous behavior observed in the 1.33nm/Q1 pore at P=250MPa is yet to be explained and will be explored in the next section. We will now move on to the study of ionic transport across the pores.

3.3 Ion transport across MoS_2 nanopores

We will now discuss another important feature of the MoS_2 nanopores for desalination processes, which is its salt rejection (SR). Figure 25 shows the results obtained for each nanopore and charge multiplier as a function of applied pressures. We notice an overall trend of decrease in SR as the value of the applied pressure grows, which is an expected result overwhelmingly supported by literature [36, 38, 63]. There is also a significant loss in SR as the pore diameter increases which is also expected, seen as the diameters of the second hydration shells of Na^+ and Cl^- fall in between 0.97nm and 1.33nm. Perhaps the most significant result is the role of charge polarization on salt rejection. It has been extensively reported in literature that functionalization of nanopores by charged particles increases ion selectivity while also compromising salt rejection [10, 36]. However,

this result is not always that straight forward and depends on contributions from other factors.

We can see in Figure 25(a) that for the 0.97nm pore salt is almost completely rejected, regardless of charge polarization inside the pore, and although SR drops slightly for higher pressures it still remains at $\sim$ 95% or higher. This is an unexpected result considering it was just shown that salt ions behave in very different ways inside 0.97nm/Q0 and 0.97nm/Q1 nanopores. Few ions ever enter the Q0 nanopore, while for Q1 there were on average 0.5-1.0 salt ions inside of it depending on applied pressure (Figure 21(e)-(f)). The data does suggest that the 0.97nm/Q1 pore may exhibit slightly lower salt rejection than 0.97nm/Q0, however that difference is minimal and could simply be caused by statistical errors. In order to confirm this assumption longer simulations and more statistical repetions would be necessary. Such nanopores are expected to exhibit complete salt rejection at realistic RO pressures of 5-10MPa.

For the 1.33nm pore we otain a more intricate result. First of all, we can see in Figure 25(b) that none of the pores exhibit salt rejection near 100%, which is consistent with previous literature [63, 40, 65]. We now see that the Q0 and Q2 nanopores present similar SR values, while Q1 exhibits the lowest values among all charge multipliers. This implies the existence of competition between two or more phenomena influencing ion transport across the pores.

As a final remark, the SR for the 1.33nm/Q1 pore is roughly equal at applied pressures of 175MPa and 250MPa. That is an exception to the overall trend of SR being inversely proportional to pressure. This is also the system for which abnormal trends appeared in the previous section for quantities such as water flux loss (Figure 21(d)), ion concentration inside the pores (Figure 21(f)). We will look closely at this system in our next analysis to try to understand what is happening.

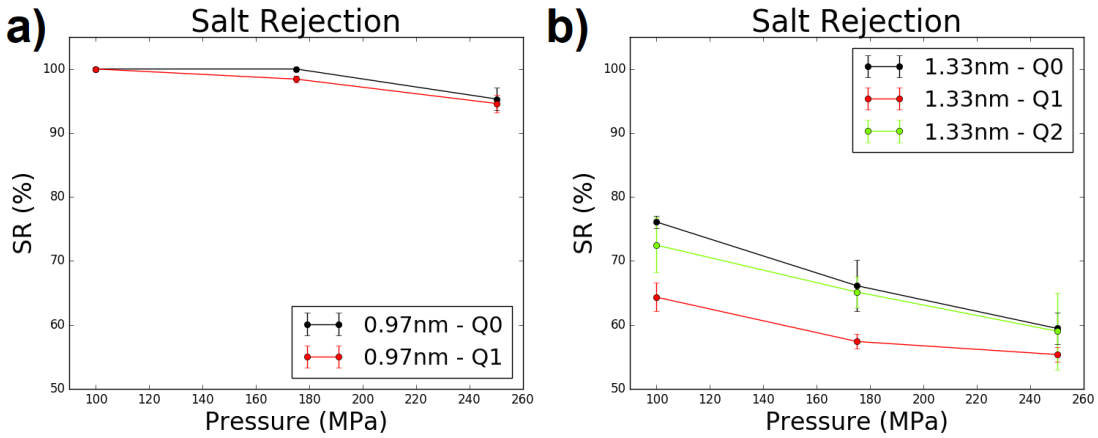

Figure 25: Salt rejection as a function of applied pressure for different values of charge multiplier (Q) and pores of diameters a) 0.97nm and b) 1.33nm

In the previous section we showed that increasing the charge multiplier of MoS_2 leads to a higher amount of ions being present inside the nanopores (Figure 21(e)-(f)). It was also established that pores exhibiting charge polarization have a strong affinity for Cl^- ions (Figure 24(a)-(b)), which tend to accumulate near the Mo-terminated edges inside the pores (Figure 23). To better understand the ion distribution near and inside the pores we plot in Figure 26 the ion density profiles for Cl^- and Na^+ ions along the Z direction. This quantity is measured by calculating the average ion density - expressed in number of ions per nm^3 - at different points in the Z axis. The results given in Figure 26 were obtained for an applied pressure of 100MPa. Each graph displays the density profile of either Na^+ or Cl^- ions for all values of charge multiplier. Figures 26(a)-(b) correspond to the 0.97nm pore and Figures 26(c)-(d) to 1.33nm.

These distributions can be roughly interpreted as the inverse of the PMF of the ions (this approximation has limitations, due to it being calculated outside equilibrium). As a general trend, we see that there is an acumulation of ions of both types near the MoS_2 membrane. This is represented by the peaks in ion density located at around 0.5-1nm to the left of the membrane's center. We can see that two sets of peaks form near the membrane, a taller one at $\sim$ 1nm away from the central Mo-layer and a shorter one at roughly 0.5-0.7nm. The first peak is mostly comprised of ions accumulated near the walls of the membrane. These are ions that would normally flow further right but are being blocked by the MoS_2 wall. The peak closer to the pore represents ions accumulated near the entrance of the nanopore. Both of these situations represent ions that could potentially enter the nanopores but do not because they can not overcome its potential energy barrier. We can see that an increase in ion density within the pores - or, equivalently, a decrease

in the potential energy barrier - is usually accompanied by a reduction in the height of at least one of the two peaks outside the pore. This means that the potential energy barrier imposed on the ions by the membrane and the nanopore leads to the accumulation of ions near the MoS_2 sheet.

There are, however, other differences in the ion density profiles, dependent on both the species of ion considered, the pore's size and the value of the charge multiplier. We notice a significantly lower amount of Na^+ ions inside the Q1 and Q2 pores when compared to Cl^-, regardless of its diameter. That indicates that the potential energy barrier imposed by the nanopore on Na^+ ions is higher than that for Cl^- ions when charge polarization is present. This is consistent with the results of Figure 24 which reveal a strong affinity of Q1 and Q2 MoS_2 nanopores for Cl^- ions over Na^+.

For the 0.97nm pores we observe near zero ion densities within the pore for Q0, indicating a very high potential energy barrier for the entrance of ions. As we move to 0.97nm/Q1 pores, we encounter slighlty higher ion densities in the pore region, particularly for Cl^-, indicating a lowering of the potential energy barrier caused by the presence of partial charges in the pore's edges.

For 1.33nm pores the situation is different, now, regardless of the value of the charge multiplier, the ion density inside the pores is always non zero, indicating that the increased pore geometry allows for the easier entrance of ions due to an overall lowering in the potential energy barrier. This same phenomenon was observed for the PMF of water as nanopore size increased (see Figures 19(a)-(b)). We also observe for 1.33nm pores that charge polarization still plays a crucial role in the distribution of ions along the Z direction. Just as we saw for the 0.97nm pore, increasing the value of the charge multiplier lowers the potential energy barrier for ions, particularly Cl^-. This is reflected in the higher concentration of ions inside more strongly polarized pores.

The ion density profiles in Figure 26 indicate that charge polarization lowers the potential energy barrier for the entrance of ions inside the pores. This leads to an increasing number of ions present inside them as charge polarization grows, explaining the results in Figures 21(e)-(f). This does not, however, explain the results obtained for salt rejection in Figure 25. There must be, as previously stated, at least one more phenomenon affecting ion transport across the pores to compete with the changes in the potential energy barrier.

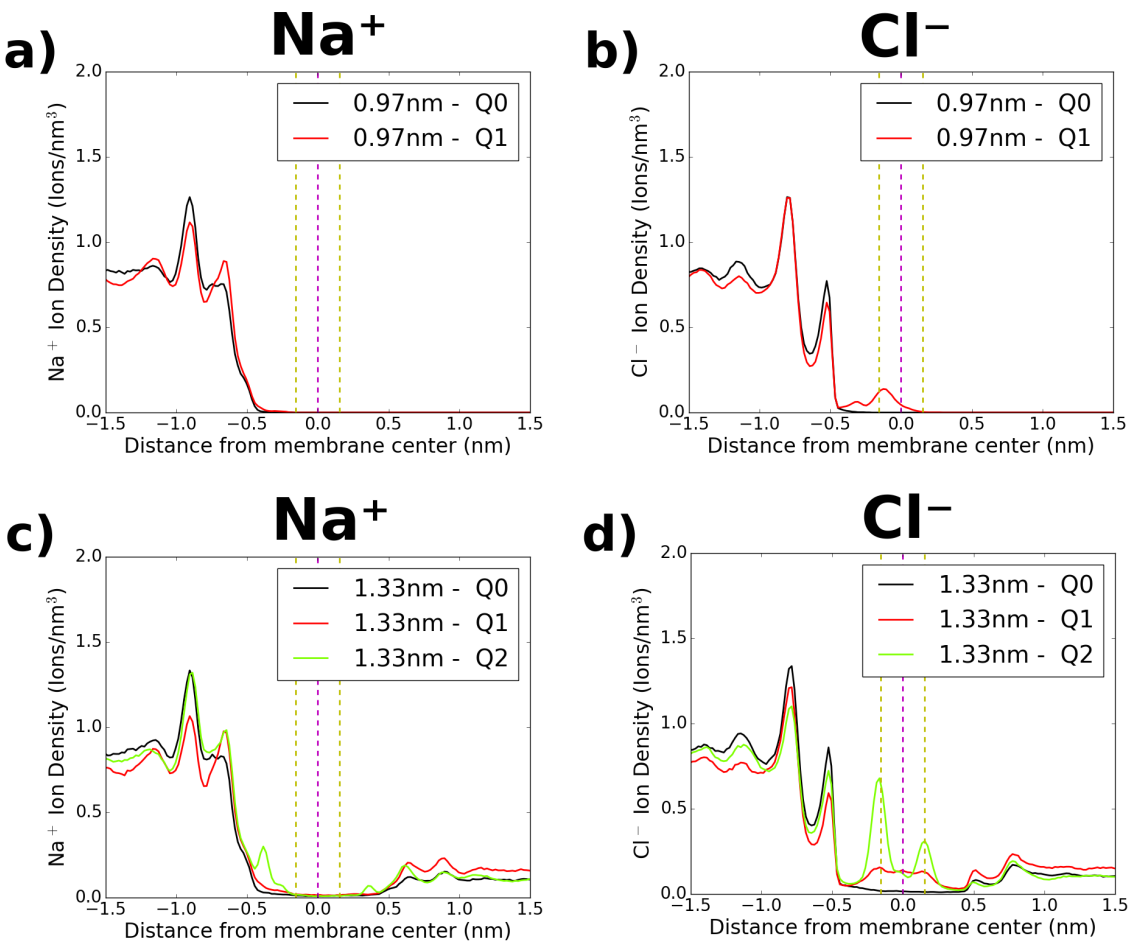

Figure 26: Ion density profile for left) Na^+ and right) Cl^- ions for pores of diameter a)-b) 0.97nm and c)-d) 1.33nm. Black, red and green lines represent Q0, Q1 and Q2 charge multipliers and yellow and purple dashed lines the position of sulfur and molybdenum atoms.

Figure 26 actually provides a clue towards determining this second factor governing ion transport inside the nanopores. One may notice that, while Q0 pores present a flat ion density profile inside the pore, pores exhibiting charge polarizations lead to profiles that oscillate in value, showing higher values in some regions of the pore and lower values at others. This phenomenon becomes very apparent in Q2 pores, displaying very pronounced peaks and valleys for both Cl^- and Na^+ ions. These oscillations may lead to the trapping of ions inside the nanopores. An analogous situation happened for the pure water system in 0.97nm/Q2 pores in Figure 19(a). A highly oscilating PMF was obtained for that system, and the value of the maxima are so high that water molecules became permanently trapped near the minima, extinguishing water flow. Such extreme cases don't appear to be happening for ions in the pores being considered here, however, we may expect significant ion trapping to happen.

Temporary trapping of ions inside the pores can be quantified by measuring the ion passing times [40, 63], displayed in Figure 27 in the form of histograms. This is a calculation of the amount of time it takes for an ion entering the nanopore from the feed side to exit it at the permeate side. A more detailed explanation of the calculation of said quantity is given in section 2.6. Each one of the four subplots represents one pore size at one value of applied pressure. For the 0.97nm diameter pore, only the 250MPa pressure (Figure 27(a)) is considered due to the very low amount of ions crossing the membrane at lower pressures. For the 1.33nm pore the three values of applied pressure, 100MPa, 175MPa and 250MPa, are represented in Figures 27(b),(c) and (d) respectively. Within each subplot, different values of charge multiplier are represented by different colors. The Y axis gives the probability density of finding an ion with an ion passing time value located within one of the bins in the X axis. We chose to express the passing times in picoseconds, rather than

nanoseconds, to make the results more clear. The X axis is represented in log scale to allow for better visualization of both the distribution's peak and its heavy tail.

As an overall trend, pores with higher charge polarizations exhibit lower peaks and heavier tails. That indicates that electrostatic forces between ions and MoS_2 atoms are responsible for ion trapping. This correlates well with the observation made regarding Figure 26 about the presence of increasing oscilations in the ion density profile caused by the strengthening of charge polarization in MoS_2. The heavier tails represent ions becoming trapped at local energy minima within the nanopore. The Q0 pores exhibit a very short tail compared to Q1 and Q2 due to the smoother profile of its potential energy barrier and less frequent ion trapping episodes.

It can also be concluded by looking at Figures 27(b)-(d) for the 1.33nm diameter pore that higher values of applied pressure lead to an increase in the peak's height and to less heavy tails. This is caused by the fact that increased applied pressures will transfer more energy to particles inside the nanopores, allowing for the compensation of electrostatic forces trapping ions inside it, causing a faster release of said ions from the pore. We see that for the highest pressure, the peak for the 1.33nm/Q1 pore undergoes a change in its shape that the other pores do not go through. This is the anomalous point described in the previous section where the number of ions inside the pore actually decreases as pressure increases (Figure 21(f)). Passing times seem to shift to much lower values, suggesting that 250MPa of applied pressure gives ions enough energy to beat the electrostatic attraction towards MoS_2 atoms 1.33nm/Q1 pores, therefore avoiding most occurrences of ion trapping. However, we have no conclusive explanation for why the 1.33nm/Q1 pore behaves differently from the others and further analysis would be necessary.

Ions with longer passing times will remain inside the pore for longer periods of time. This will, in turn, reduce the amount of ions that leave the pore towards the permeate reservoir. This is a remarkable result, we first showed that stronger charge polarizations inside the pores may lead to a decrease in salt rejection due to the lowering of the pore's potential energy barrier for salt ions. However, we have just demonstrated that increased charge polarization also contributes to a higher occurrence of ion trapping within the pores, potentially increasing salt rejection. We have thus demonstrated the existence of a competition between two mechanisms that influence the value of salt rejection in different directions as charge polarization increases.

This potentially explains why 1.33nm/Q1 pores exhibit lower values of salt rejection than 1.33nm/Q0 and 1.33nm/Q2 pores. The 1.33nm/Q0 pores have a higher salt rejection due to its high potential energy barrier for the entrance of ions into the nanopore, 1.33nm/Q2 pores on the other hand attract large amounts of ions to its inside, however, electrostatic interactions between the pore and the ions are so strong that they become heavily trapped, once again increasing salt rejection. The 1.33nm/Q1 system exists in between these two cases, and the competition between both phenomena balances itself in a way that leads to its reduced salt rejection.

For the anomalous point (1.33nm/Q1 at P = 250MPa), a shift of the passing times towards lower values should have led to a significant lowering of salt rejection. What we observe in Figure 25(b), however, is the opposite, as salt rejection appears to be unchanged as we move from 175MPa to 250MPa of applied pressure. This result is puzzling and can not be explained by the proposed mechanism. This indicates that additional phenomena are likely responsible for the regulation of ion transport across the nanopores.

Ion Passing Times

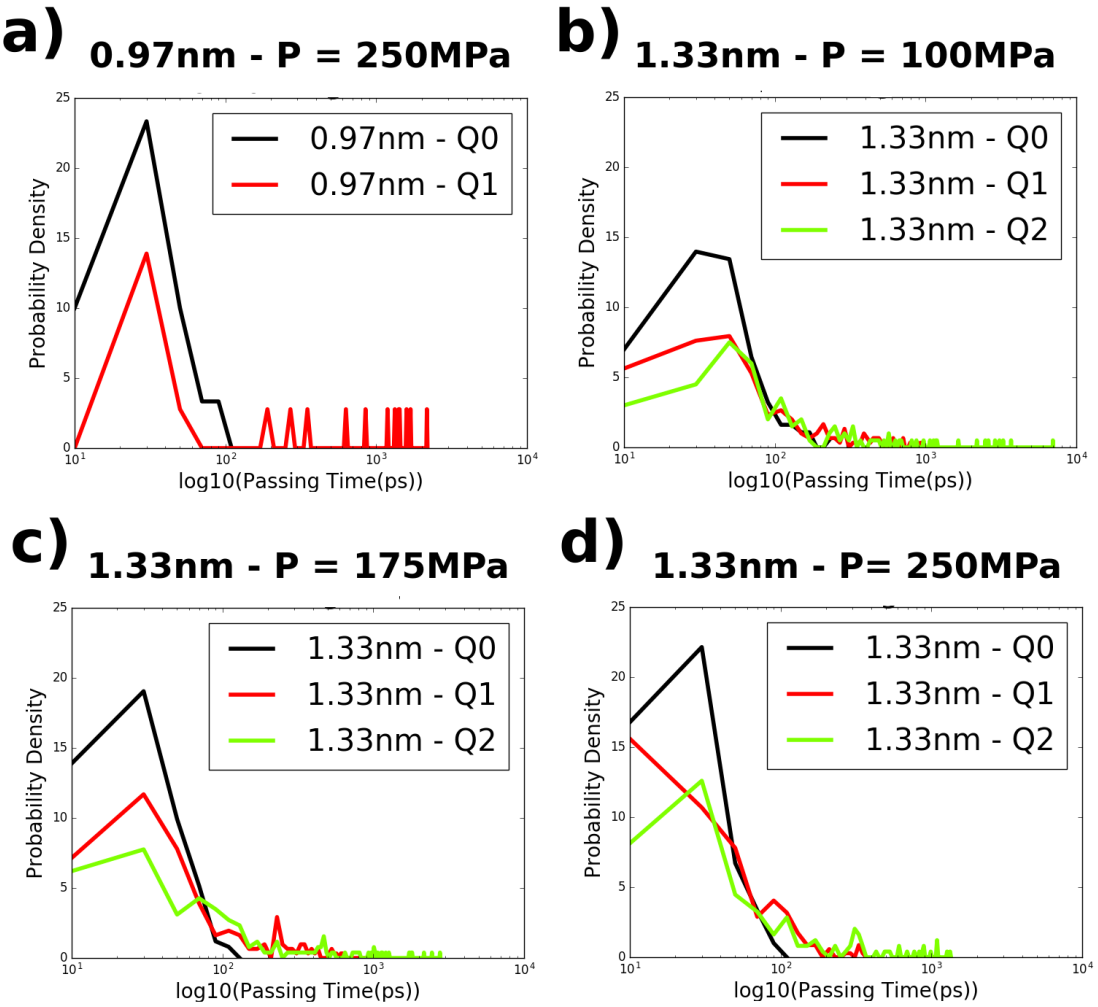

Figure 27: Ion passing time histograms for 0.97nm pores at a)250MPa and for 1.33nm pores at b) 100MPa, c) 175MPa and d) 250MPa of applied pressure. Black, red, and green lines represent charge polarizations of Q0, Q1 and Q2.

Before concluding this section, there are a few more intricate aspects regarding the proposed mechanism governing ion transport that will be explored. We would first like to differentiate the behavior of Na^+ and Cl^- ions traversing the pores. As has been stated beforehand, Q0 pores do not show a strong affinity for one specific ionic species, however, Q1 and Q2 show a considerable preference for Cl^- ions, leading to the presence of high quantities of said ions inside the pores, in contrast with the minute concentrations of Na^+ found within it (see Figures 21(e)-(f)). On top of that, Cl^- ions exhibited ion density profiles that were more heavily dependent on the value of the charge multiplier and which featured higher peaks and valleys than for Na^+ (Figure 26). That suggests Cl^- ions are more suceptible to ion trapping than Na^+ when charge polarization is present. In order to corroborate this hypothesis we plotted in Figure 28 the mean ion passing times for Na^+ and Cl^- ions separately. The calculations were made for the same four systems displayed in Figure 27. What we observe is precisely a confirmation of the hypothesis: pores possessing charge polarization show much higher ion passing times for Cl^- than for Na^+, however when no charge polarization exists they both exhibit similar values of ion passing times.

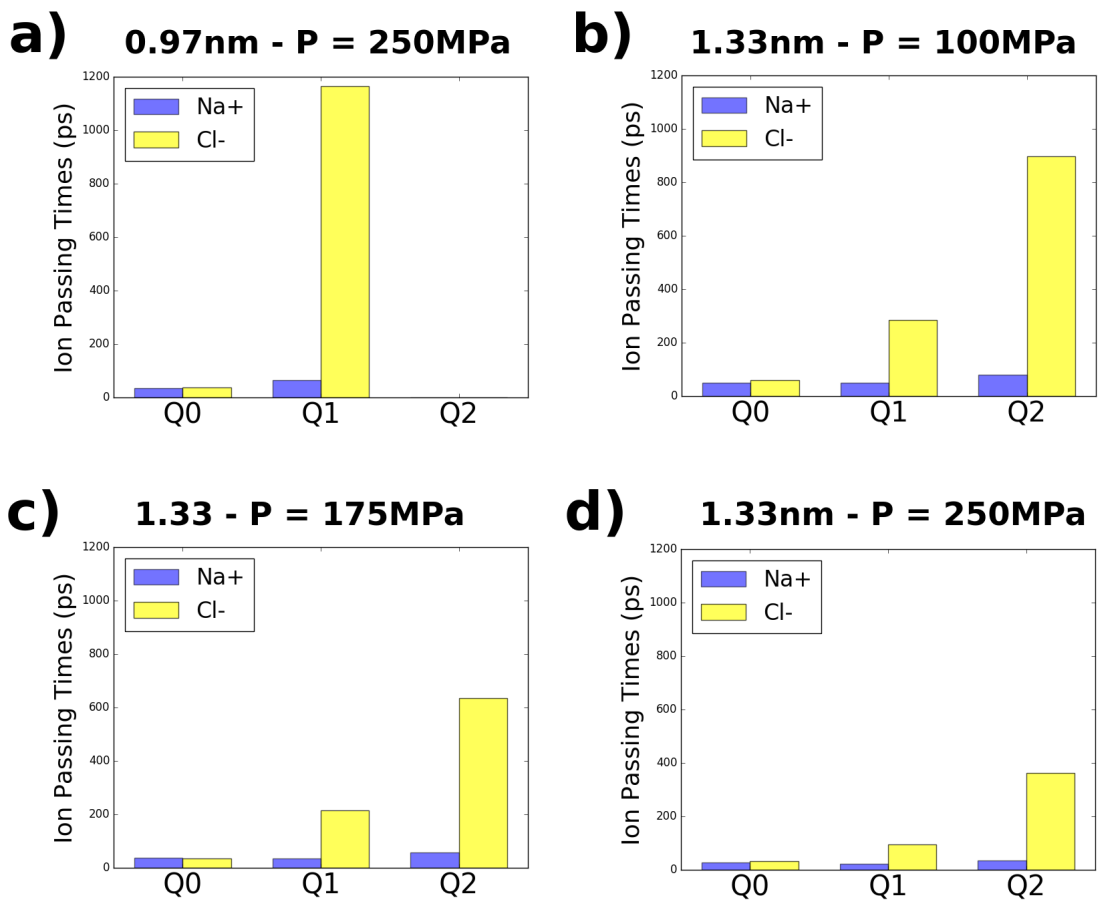

Figure 28: Mean ion passing times as a function of the charge multiplier (Q) for 0.97nm pores at a)250MPa and for 1.33nm pores at b) 100MPa, c) 175MPa and d) 250MPa of applied pressure. Yellow bars represeent Cl^- ions and blue bars Na^+.

We have shown in this section that the values obtained for salt rejection of the pores depend on an intricate balance between different ion transport phenomena. We demonstrated the existence of competition between the lowering of the pore's potential energy barrier for ions and the increased ion tapping, both brought about by an increase in charge polarization. The balance between these two factors regulates the salt rejection of each nanopore and leads to a remarkable result: salt rejection for 1.33nm/Q0 and 1.33nm/Q2 pores are nearly identical, while it was shown to be lower for 1.33nm/Q1. That means that for pores with very weak charge polarizations (Q0 $<$ Q $<$ Q1) the dominating factor governing ion transport is the high potential energy barrier keeping ions from entering the nanopore. For pores with strong charge polarizations (Q $>$ Q1), the dominant contributor is now the increase in ion trapping within the pores. The charge polarization of regular MoS_2 (Q1) is an intermediate value between these two situations where both phenomena balance each other out to produce a nanopore with lower salt rejection. Besides that. We also highlighted the more significant contribution of Cl^- over Na^+ ions to ion trapping episodes in Figure 28.

An outlier to our proposed mechanism for ion transport across MoS_2 pores is the 1.33nm/Q1 pore at 250MPa of applied pressure. This configuration exhibited a lower concentration of ions inside the pore than expected, which led to suspicion that 250MPa was a high enough pressure to significantly reduce ion trapping. This assumption was confirmed by Figure 27(d) as it exhibited uncharacteristically low ion passing times. However, this should lead to a strong decrease in salt rejection, but the opposite is observed in Figure 25(b), where salt rejection appears to be unchanged between 175MPa to 250MPa. We have no explanation for this and other factors are likely regulating ion transport across the pore in these circumstances.

In this section, we entirely skipped the discussion on the role of ion-ion interactions in regulating ion transport across the pores. This should definitely be a contributing phenomenon, particulary

for pores with charge polarization where pores hold, on average, more than one ion at a time (see Figure 21(e)-(f)).

3.4 Summary

In this chapter we provided a detailed analysis on water and salt ion transport across monolayer MoS_2 pores of diameters 0.97nm and 1.33nm. In our simulations we altered the charge distribution of MoS_2 in order to generate hypothetical membranes with no charge polarization (Q0) or double the charge polarization (Q2) of regular MoS_2 (Q1). From our results we propose mechanisms that explain transport phenomena across such pores.

We started by analyzing pure water systems in order to understand how water flows through the nanopores in the absence of salt. We showed in Figure 15 that charge polarization influences the value of the water flowrates obtained for the nanopores. For the 0.97nm pore we found slightly higher flowrates for Q1 pores over Q0 ones, while Q2 pores exhibited no water flow whatsoever. For the larger pores with 1.33nm diameter Q1 and Q0 pores exhibit similar flowrates at 100MPa applied pressure, however, as pressure increases flowrates for Q1 become higher. 1.33nm/Q2 pores always exhibit lower flowrates than its Q0/Q1 counterparts, however flowrate across it is only moderately lower. Water flowrates for 1.33nm pores were roughly 5 times higher than for 0.97nm.

We computed, in Figure 16, the average number of water molecules contained within the pores for different charge polarizations. We showed that higher charge polarizations make the nanopores more hydrophilic, which should contribute to higher water flowrates. Hydrophilicity does not, however, explain the results obtained for water flowrates, indicating other factors must be considered. We then computed the oxygen density maps inside the pores in Figure 17 to better visualize how water structures itself in such an environment. For both pore sizes we observe a shift from a smoother to a more localized water distribution within the pore as charge polarization increases. The stronger electrostatic forces attract water towards the pore edges near its Mo terminations, forming intricate patterns. For the 0.97nm/Q2 nanopore an extremely localized distribution is observed, with oxygen atoms strongly confined to the vicinity of Mo atoms, indicating a potentially frozen-like structure leading to the absence of water flow.

The orientation of water molecules' dipole vector with respect to the Z axis was computed to generate the curves in Figure 18. We showed that Q0 pores allow for near random orientations inside the pores, while stronger charge polarizations led to rotations of molecules as they travel across the pores, as well as constraints to the possible orientations of water molecules due to the presence of electrostatic forces between MoS_2 and water. The 0.97nm/Q2 pore exhibits extremely limited possible water molecules' orientations within the pore, forcing molecules to perform large rotations to travel very small distances, effectively impeding its flow. We propose that such angular constraints are responsible for a slow down in water flow across MoS_2 pores. We also computed the orientation of water molecules in a Q(-1) MoS_2 nanopore, where Mo atoms are negatively charged and S atoms positively charged to show that water orientation inside the pore is governed by the charge of molybdenum atoms.

PMF curves were calculated in Figures 19(a)-(b) to visualize the effects of coulombic forces on the distribution of water molecules inside the pores. 0.97nm pores naturally had higher potential energy barries than 1.33nm ones. Q0 pores exhibited a smoother potential energy barrier, whereas Q1 and Q2 exhibited peaks with similar shapes and oscillations along the pore length that increased in amplitude as charge polarization went up. For the 0.97nm/Q2 pores the height of the energy barrier more than doubled, creating maxima and minima separated by very high energy barriers, leading to the freezing of water molecules inside the pore and a flowrate of zero. The average number of hydrogen bonds per water molecule along the Z direction was given in Figures 19(c)-(d) in order to show how electrostatic forces disturb the hydrogen bond network. We see a progressive reduction in the number of hydrogen bonds per molecule at the center of the pore as charge polarization increases. This is significant because hydrogen bonds are needed in order to pull water molecules away from the Mo terminations of the pore, otherwise they may become stuck. This is precisely what happens to the 0.97nm/Q2 pore, where almost half the hydrogen bonds are destroyed around the center of the pore due to the strong coulombic attraction between Mo and oxygen atoms, causing water molecules to become permanently stuck to the pore edge, stoping water flow. This phenomenon also manifests in Figure 18(a) as a strong angular constraint imposed on water molecules.

For a pure water system, we show that the mechanism regulating water transport across MoS_2 pores consist of a competition between hydrophilicity, angular constraints and disturbances to the hydrogen bond network. This translates into a competition between water-MoS_2 electrostatic forces and water-water forces represented by hydrogen bonds. Electrostatic forces can increase water flow by making the pore more hydrophilic but can also slow it down by breaking up hydrogen bonds, limiting the possible orientation of water molecules within the pore and pulling water

molecules towards the pore's edge. These contributions balance each other to determine water flowrate across the pores, Q1 pores of both diameters appear to sit at a sweet spot where they are hydrophilic enough but electrostatic forces are not strong enough to significantly slow down water molecules. They therefore exhibit a high water flowrate, higher than the hypothetical Q0 and Q2 pores.

We then showed that water flowrate is reduced by the addition of salt ions to the system (Figures 21(a)-(b)). We defined a quantity called water flux loss which quantifies the loss in water flow when ions are added to the system and is represented in Figures 21(c)-(d). This quantity increases with charge polarization leading to a situation where now Q0 pores have higher water flowrates than Q1 pores, unlike what was observed in pure water systems. We showed in Figures 21(e)-(f) that there appears to be a correlation between water flux loss and the mean number of ions present inside pores, which also increases with charge polarization.

We propose that the reduction in water flow is caused by the reduction in the number of water molecules inside the pore as more ions are present within it. In order to quantify this phenomenon we define the water exclusion coefficient which represents the loss in the average number of water molecules that are present in the pore as salt ions are introduced into the system. This quantity is given in Figures 21(g)-(h) and also exhibits strong correlation with water flux loss in Figures 21(c)-(d). To better visualize this correlation we plot in Figure 22 the water flux loss as a function of the water exclusion coefficient for all pores studied so far, which indicates a strong linear correlation between both quantities. This indicates that a reduction in the water flowrate of the pores is caused by the increased presence of salt ions inside them as charge polarization grows.

In Figure 23 we plot the ion density maps for Na^+ and Cl^- ions inside the pore. We notice that ion distribution is highly dependent on charge polarization of the pore, and that Cl^- appears to be more affected by changes in the charge multiplier of MoS_2 than Na^+ ions. We also show that, as charge polarization becomes present, Cl^- ions and water molecules tend to compete for the same sites inside the pore, which exacerbates the exclusion of water molecules. We showed in Figures 24(a)-(b) that Q0 pores exhibit similar amounts of both ion types inside it, but as charge polarization becomes present the pores show a very strong affinity to Cl^- ions. This is significant because Cl^- ions compete with water molecules for the same sites in the pore, so a larger amount of Cl^- ions in the pore will further intensify the exclusion of water molecules and lead to even lower water flowrates.

Finally, we studied ion transport across the pores in order to understand its salt rejection performance. Our simulations indicated in Figures 25(a)-(b) that salt rejection is dependent on charge polarization, pore size and applied pressure. 0.97nm pores exhibit near 100% salt rejection for both Q0 and Q1 pores. At 100MPa both display complete salt rejection, however at higher pressures it drops a tiny bit. For 1.33nm pores salt rejection never exceeds 80%, which was expected as pore diameter is now larger than the diameter of the ions' hydration shells. Salt rejection appears to decrease linearly with applied pressure and Q0 and Q2 pores exhibit nearly identical values of salt rejection, while Q1 displays the lowest values for all applied pressures. A highly unexpected result like this suggests the presence of competition between different phenomena governing ion transport across MoS_2 pores.

In order to estimate how the pore's potential energy barrier for the entrance of ions behaves for different charge distributions we plotted in Figure 26 the ion density profiles in the Z direction for both ion types and pore diameters. For 0.97nm pores very few ions enter the pores, however Q1 pores exhibit a modest concentration of Cl^- ions, which is nonetheless much higher than that for Q0, indicating a lowering in the potential energy barrier for Cl^- ions as the charge multiplier goes from Q0 to Q1. 1.33nm pores naturally exhibit higher ion densities inside it due to its larger diameter, allowing ions to maintain most of its hydration shell inside the pore. Ion density inside the pores increases with charge polarization as well for both ion types, but in a more pronounced way for Cl^-, also indicating a lowering in the potential energy barrier caused by electrostatic interactions. The changes in the potential energy barrier do not explain the values of salt rejection obtained in Figure 25. We have looked at how ions enter the pore, we shall then look at how they exit it.

Ion densities for Q1 and particularly for Q2 exhibit a non smooth profile inside the pores, forming peaks and valleys. This causes increased episodes of ion trapping inside the pores, which can slow down ion flow across the pores. In order to check the validity of this claim we computed the ion passing times for individual ions in the system during our simulations and plotted the equivalent histograms in Figure 27. We showed that ions tend to stay for very short periods of time inside Q0 pores, since it is more energetically favorable for them to flow to the permeate reservoir where they can restore their hydration shell. However as charge polarization increases a heavy tail appears in the histograms, corresponding to ions that become trapped inside the pores due to electrostatic forces, which compensate the energy cost caused by the partial destruction of the hydration shell. Ion trapping causes an increase in salt rejection as it makes it hard for ions

the leave the pore and enter the permeate reservoir. We also showed in Figure 28 that ion trapping predominantly affects Cl^- ions due to its strong coulombic attraction towards Mo atoms.

Based on our results we propose the following mechanism for ion transport across MoS_2 nanopores: hydrophobic pores (Q0) exhibit a high potential energy barrier for the entrance of ions, leading to high salt rejection, strong charge polarizations (Q2) also increase salt rejection by keeping ions inside the nanopores for longer periods of time. However, both phenomena compete between them, causing regular MoS_2 nanopores (Q1) to exist in between these two situations where both factors interact in such a way to decrease the salt rejection of the pore. This mechanism is obviously incomplete since it only considers ion-MoS_2 and ion-water contributions, represented by electrostatic interactions and the hydration shell respectively. We did not carry out any analysis on ion-ion interactions, which will certainly play a role on ion transport across the pores, especially at higher charge polarizations where multiple ions are found inside the pores simultaneously.

We were unable to explain what happens to the 1.33nm/Q1 pore at P = 250MPa and why its water flux loss and salt rejection exhibit different values than it would have been expected. Other phenomena are likely behind this behavior.

We have thus concluded the study of water and ion transport across MoS_2 pores. The next chapter will be dedicated to the study of water transport across bilayer MoS_2 nanoporous membranes.

4 Results - Bilayer membrane

In this chapter we study the flow of water through two nanopores in a bilayer MoS_2 membrane. In particular we analyze the effects that the charge distribution of MoS_2 has on the transport of water molecules. We perform simulations for bilayer MoS_2 membranes with a layer separation of 1.2nm, and we consider not only the regular MoS_2 charge distribution (Q1), but also an MoS_2 membrane with no charge polarization (Q0) and with double the charge polarization (Q2). The purpose of these simulations is to elucidate the role of electrostatic interactions with the membranes inner walls on the transport of water molecules through a bilayer membrane with fixed geometry. Only pores of diameter 1.33nm were considered this time, and we also analyzed the impact that misalignement between both pores has on water transport by introducing three different values of pore offset: 0.0nm, 0.96nm and 2.57nm, as well as a brief discussion on the role played of layer separation.

4.1 Pure water system

We performed simulations of the system depicted in Figure 7 for a fixed layer separation of 1.2nm between both MoS_2 sheets, measured from the center of the Mo layers in each side, as this configuration has been shown to be stable in water [27]. Our aim is to provide a picture of how water flows through such a system. We expect new mechanisms to contribute to water dynamics, adding to those described in section 3.1 related to in-pore phenomena as particles now also interact with the inner walls of the MoS_2 bilayer as they flow from the feed to the permeate.

Figure 29 summarizes the results obtained for the water flowrate of all bilayer systems simulated. In Figures 29(a)-(c) we show results obtained for the water flowrate (Y axis) as a function of applied pressure (X axis). Each subplot features the three values of charge multipliers, Q0, Q1 and Q2 at a fixed value of pore offset, 0nm, 0.96nm and 2.57nm in Figures 29(a), (b) and (c) respectively. The flowrate increases linearly with applied pressure, as was observed for the monolayer membrane in Figure 15. We can also see that a larger pore offset causes a reduction in water flow, indicating that interaction with the MoS_2 walls may reduce the flow of water molecules.

Comparing the flowrates in the system with a monolayer membrane, illustrated in Figure 15, with the system composed of bilayer MoS_2, shown in Figures 29(a)-(c), we observe that both exhibit the highest flowrate for Q1, regular MoS_2. However, more water passes through the monolayer membrane for Q0 than for Q2, while in the bilayer system more water flows across the membrane for Q2 than for Q0.

According to classical hydrodynamics the addition of a second membrane with an equal sized pore should reduce water flow by half [38]. This, however, is only valid for macroscopic systems and disregards any of the confinement effects we observe in nanopores and 2D materials. We see in Figures 29(a)-(c) that the system responds differently to the introduction of a second MoS_2 sheet depending on its charge multiplier and pore offset. In order to quantify the changes in water transport brought about by the addition of the second layer we plot in Figures 29(d)-(f) the bilayer flux loss, which is defined by:

$$\Delta\Phi = 1 - \frac{\Phi_{bilayer}}{\Phi_{monolayer}} \tag{12}$$

where $\Delta\Phi$ represents the bilayer flux loss and $\Phi_{monolayer}$ and $\Phi_{bilayer}$ represent the water flowrates across mono and bilayer MoS_2 membranes. They are chosen in a way that yields values of bilayer flux loss between 0 and 1. A value of zero represents no flux loss as the second layer is introduced, while a value of 1 means total halting of water flow across the membrane.

This quantity is a ratio between water flowrates of bilayer and monolayer membranes in pure water systems. By normalizing the results with respect to monolayer MoS_2 it removes the single-pore contributions analyzed in chapter 3, assuming the second layer does not interfere with usual in-pore phenomena. It, therefore, allows us to isolate the contribution that interactions with the membrane's inner walls have on the water flowrate.

The Y axis in Figures 29(d)-(f) represent the values of bilayer flux loss as a function of the charge multiplier. Dots colored blue, orange and green represent pore offset values of 0nm, 0.96nm and 2.57nm respectively and subplots (d), (e) and (f) show measurements taken at applied pressure values of 100MPa, 175MPa and 250MPa respectively. We spot a clear trend of decrease in the bilayer flux loss as charge polarization in the membrane increases. This is a remarkable result, as it shows electrostatic interactions with the MoS_2 walls become relevant in bilayer membranes, something that was not true about monolayer MoS_2 in chapter 3. Values of bilayer flux loss for Q0 stay at around 0.6, while for Q2 they approach 0.5 for a pore offset of 0.0nm. This is an interesting result, as the system almost reaches the value of 0.5 predicted by classical hydrodynamics. We can

conclude, however, that nanoscale phenomena seem to cause a further decrease in water flow for all considered systems, leading to bilayer flux losses over 0.5.

Figures 29(d)-(f) also highlight the impact of pore offset on water flow. All considered systems follow a pattern of decreased water flow for larger pore offsets. This effect, however, seems to manifest differently for the Q0 system, where both non zero offsets lead to similar values of water flow, unlike Q1 and Q2 pores.

It is also important to note that Figures 29(d)-(f) show that the value of bilayer flux loss is dependent on pressure, and at higher pressures Q0 and Q1 exhibit similar results for some values of pore offset, while Q2 has a lower value in all cases.

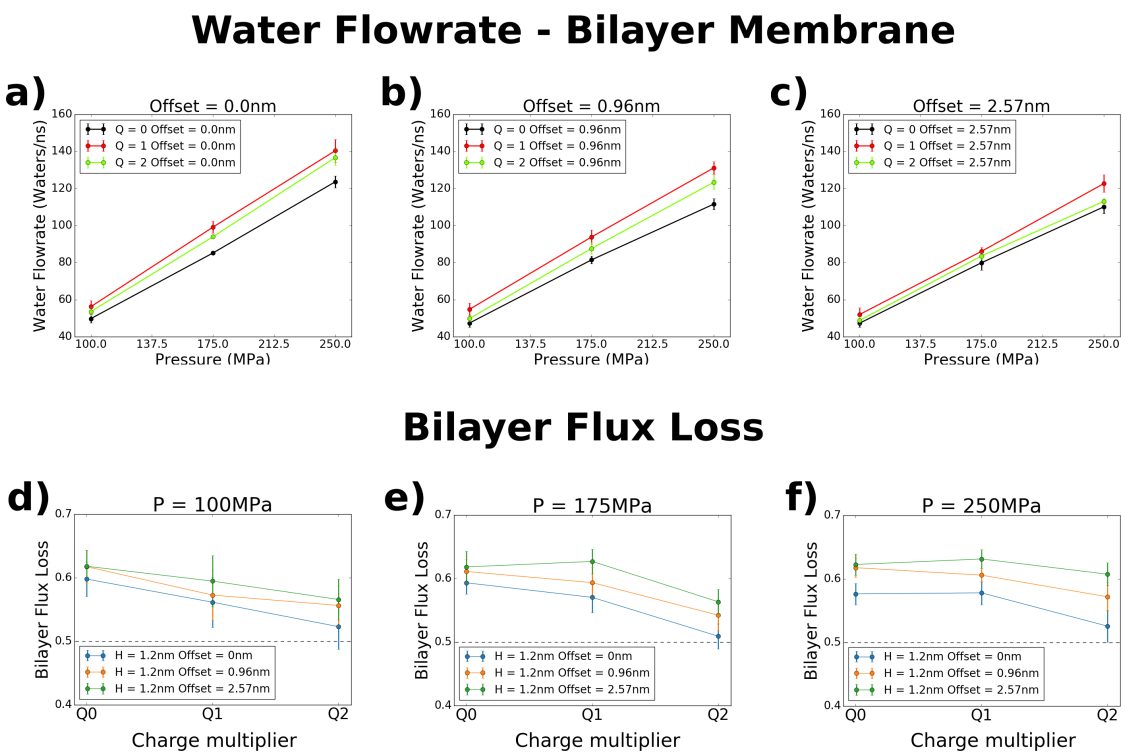

Figure 29: (Top) Water flowrate measured in water molecules per ns as a function of applied pressure for Q0, Q1 and Q2 (black, red and green) and pore offset values of a) 0nm, b) 0.96nm and c) 2.57nm. (Bottom) Bilayer flux loss as a function of charge multiplier for all values of pore offset and d) 100MPa, e) 175MPa and f) 250MPa values of applied pressure. The dashed line indicates a bilayer flux loss of 0.5 as predicted by classical hydrodynamics.

One can gain a better understanding of the dynamics of water in the bilayer system by looking at the water molecules' passing times, which are plotted in Figures 30(a)-(f) in the form of histograms. The passing times here represent the amount of time it takes for a water molecule entering the interlayer region from the feed side to exit it at the permeate side. These measurements were only carried out for an applied pressure of 100MPa. They were measured in picoseconds and the X axis shows them in log scale, each histogram was also normalized to yield an integral of 1. Figures 30(a)-(c) show the distributions at a fixed value of charge multiplier (Q0, Q1 and Q2, respectively) and the blue, orange and green curves represent the passing time statistics for pore offset values of 0.0nm, 0.96nm and 2.57nm respectively. Figures 30(d)-(f) display the same distributions but now at fixed pore offset and charge multipliers of Q0, Q1 and Q2 represented in black, red and green, respectively. Figures 30(g)-(i) provide a comparison between mean water passing times and water flowrate.

In a situation where pore offset is equal to zero, water molecules can cross the membrane without necessarily traveling through the entirety of the interlayer region since both pores are perfectly aligned. As pore ofset increases water molecules are forced to travel a larger path inbetween MoS_2 sheets in order to arrive at the permeate. These two situations give rise to a fast and slow mode, and can be seen clearly in the blue histograms in Figures 30(a)-(c) as two distinct peaks in the passing time distributions. As the offset increases to 0.96nm we see a reduction in the fast mode and an increase in the slow mode and for the larger 2.57nm offset a complete disappearance of the fast mode as now all particles are forced to travel through the interlayer region. That will lead molecules to interact with the MoS_2 walls for longer periods of time and water-MoS_2 interactions

will become more significant.

It is also worth noticing that the charge polarization of MoS_2 sheets seems to play a small role in the distribution of water molecules' passing times, as is confirmed by the similar shapes of the histograms in Figures 30(d)-(f).

A higher mean water passing time does not necessarily mean a lower water flowrate. In their work on bilayer graphene membranes Grossman et al. found that although pore offset caused the disappearance of the fast mode in the histograms, it did not impact the membranes water flowrate [38]. This is likely due to graphene's extremely low friction coefficient. However, this is not the case for our MoS_2 bilayer membrane, even when no charge polarization is present.

Interactions between water molecules and the inner walls of the membrane are likely to play an important role in the dynamics of water in bilayer MoS_2 membranes. The amount of interaction between water molecules crossing the membrane and the inner walls will be directly proportional to the fraction of water molecules belonging to the slow mode. In an ideal case where this were the only mechanism contributing to the bilayer flux loss, we would expect to see a well defined inversely proportional relationship between water flowrate and mean water passing times for all values of charge multiplier. The mean passing times represent the mean value of the passing time histograms.

In Figures 30(g)-(h) we plotted the inverse mean water passing times and the water flowrate, respectively, as functions of the charge multiplier at an applied pressure of 100MPa. Each color represents a value of pore offset, using the same color code as Figures 30(a)-(c). We can see that the mean passing times increase for larger pore offsets. There appears to be a certain degree of correlation between the two graphs, so to better visualize it, in Figure 30(i) we plotted the graph of water flowrate vs the inverse of the mean water passing times. We can see that for the larger offset we have a very good linear correlation between both quantities, and for offset equal to zero the relationship is pretty close to linear as well. This is further indication that something in the interlayer region is causing water molecules to slow down. However, this correlation is far from exact, particularly for the pore offset of 0.96nm we don't see the same linear dependency, as the points corresponding to Q1 and Q2 show nearly identical mean water passing times but values of water flowrate that differ significantly. We can thus conclude that other phenomena besides interaction with the MoS_2 walls are behind the dynamics of water inside bilayer MoS_2 membranes.

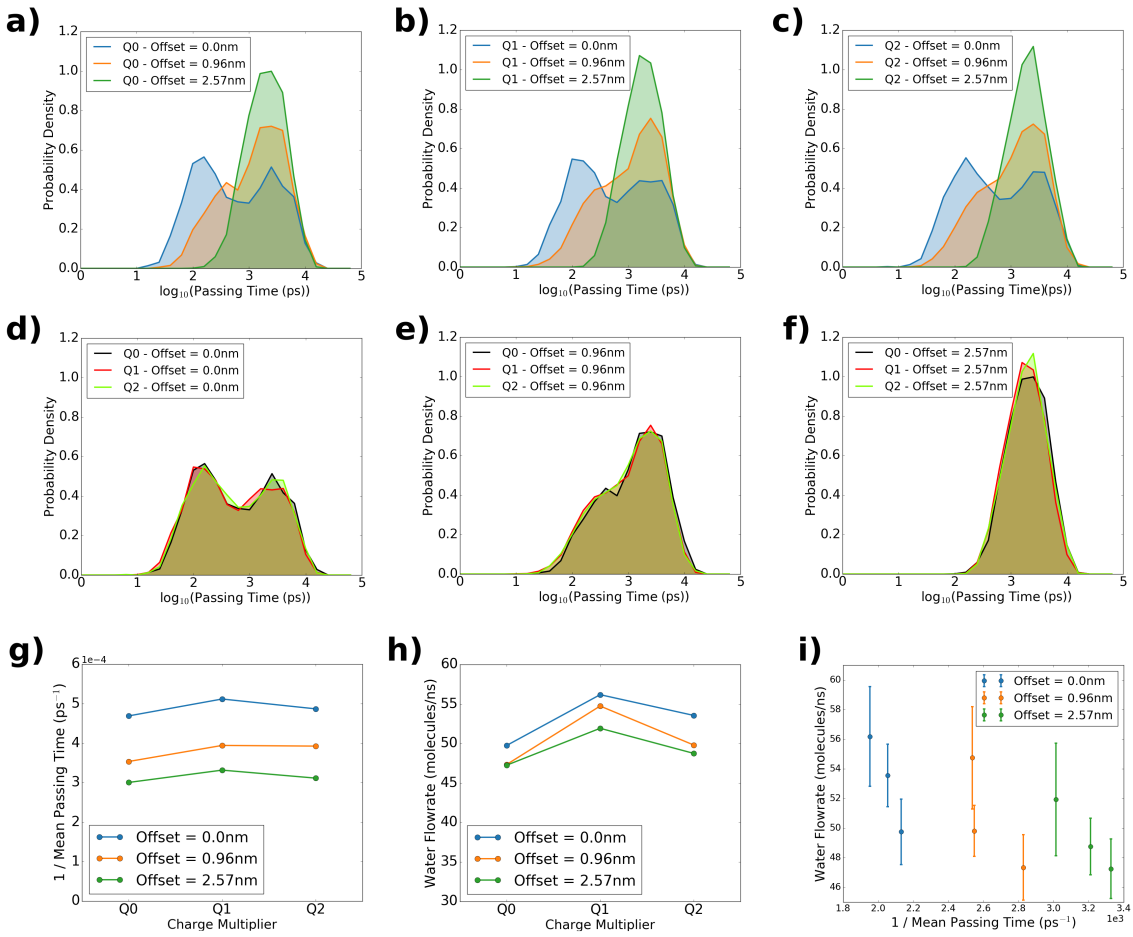

Figure 30: Histograms of water passing times (amount of time water molecules spend in the interlayer region of the membrane). The X axis is given in log_{10} scale and the passing times were measured in picoseconds. The Y axis represents a probability density determined so each histogram integrates to one. (Top) Histograms for different values of pore offset for fixed charge multipliers a) Q0 b) Q1 and c) Q2. (Middle) Histograms for different values of charge multipliers at fixed values of pore offset d) 0.0nm e) 0.96nm and f) 2.57nm. (Bottom) g) Inverse of mean passing times and h) water flowrate, both as function of as function of charge multiplier, measured at P=100MPa. i) Plot of water flowrate as a function of the inverse mean water passing times.

In order to better visualize the spatial configuration of water molecules in the system we plotted the potential of mean force (PMF) curves for water in all nine systems displayed in Figure 31. The Y axis represents the value of the PMF in kcal/mol and the X axis the distance in nanometers from the first pore's central Mo layer. The vertical dotted lines represent the positions of Mo and S atoms, where yellow represents sulfur and purple represents molybdenum. Subplots on the right side were measured at fixed charge multiplier and varying offsets and those on the left at fixed offsets and varying charge multipliers.

Figure 31 allows us to visualize how water molecules organize themselves between the MoS_2 sheets and also how the presence of the second membrane layer impacts the water structure inside each pore. The PMFs show both pores have similar potential energy profiles as those for the monolayer membranes in Figure 19, but they are now separated by a structured bilayer of confined water. We can see that the two minima corresponding to the water layers approach -1 kcal/mol, indicating that they exhibit a considerably higher density than that of bulk water. This kind of structuring is caused by confinement and has been described in nanoslits with separations of $\sim$ 1nm [38, 75]. This causes water molecules to form more hydrogen bonds within each water layer than in between them. That, in turn, creates a large potential energy barrier between the two water layers which needs to be overcome by the molecules so they can flow to the other side.

In Figures 31 (a), (c) and (e) we plotted the PMF curves for membranes with charge multipliers of Q0, Q1 and Q2 respectively. Each subplot shows curves in blue, orange and green which represent

the three values of pore offset, 0.0nm, 0.96nm and 2.57nm, respectively. They carry information regarding the influence of pore offset on the organizaiton of water molecules in a system with equal charge polarization. We also add to thi graph, as dashed curves, the PMF for an equivalent monolayer MoS_2 membrane for comparison purposes. We can see in Figures 31(a) and (c) that for the Q0 and Q1 systems the presence of a pore offset slightly modifies the potential energy barrier of the pores, indicating that interaction with the water bilayer changes the distribution of water inside them. The same, however, does not happen for the Q2 system, likely because electrostatic interactions with the pore are too intense to be disturbed by water molecules in the confined bilayer. For Q0, we observe a modest increase in the potential energy barrier within the pores that is identical for offsets of 0.96nm and 2.57nm. We recall that for Q0, these two values of pore offset exhibited nearly identical water flowrates. These small changes in pore energy profiles indicate that bilayer flux loss does not exclusively represent the contribution of the interlayer region to water transport. We will take such differences in account, but they are small enough so that we can use the bilayer flux loss as a good approximation for the role of the interlayer region in governing water dynamics.

In Figures 31(b), (d) and (f) we plotted the same curves but in a different order. Now each graph represents a fixed value of pore offset (a) 0.0nm, (b) 0.96nm and (c) 2.57nm, and curves with the colors black, red and green represent charge multipliers Q0, Q1 and Q2. These three graphs allow for a comparison between PMF curves of systems with equal geometry but different charge polarizations. We note that in Figure 31(b) all pores have similar heights for their potential energy barriers for a pore offset of 0.0nm, just as observed in monolayer pores. However, once pore offset is present we can see the slight increase in the potential energy barrier of the Q0 nanopore previously identified in Figure 31(a). The energy profile for the interlayer water exhibits a slightly lower amplitude between the minima and the maximum for Q2 than it does for Q0 and Q1, regardless of the pore offset value. This might contribute to the lower bilayer flux loss of Q2, as water molecules can pass from one layer to another more easily. The difference in the energy profile of the confined water bilayer is very small, therefore further investigation on the response of those water molecules to increased electrostatic interactions with the walls will be conducted to confirm it.

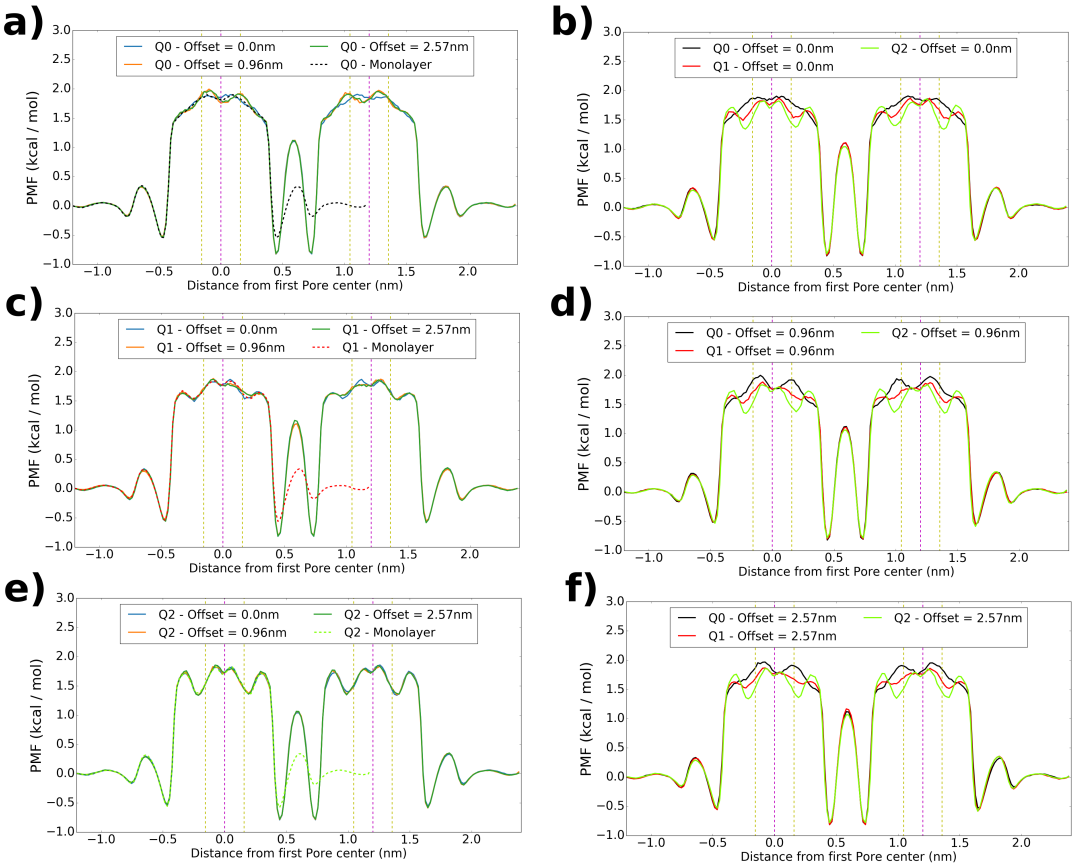

Figure 31: Potential of mean force of water for bilayer MoS_2 membranes. (Left) PMFs at varying pore offsets, 0.0nm (blue), 0.96nm (orange) and 2.57nm (green) at fixed charge multiplier a) Q0, c) Q1 and e) Q2. Monolayer PMFs are shown as dashed curves in a), c) and e) for comparison purposes. (Right) PMFs at varying charge multipliers, Q0 (black), Q1 (red) and Q2 (green) at fixed values of pore offset b) 0.0nm, d) 0.96nm and f)2.57nm. Dashed lines in purple and yellow represent the position of Mo and S atoms respectively.

We have obtained an indication that a higher charge polarization might mitigate the confinement effects brought by the narrow spacing between the MoS_2 sheets, reducing the amplitude of the variations in water density along the interlayer region and bringing it closer to a bulk-like distribution with a flatter profile. In order to test this hypothesis we simulated two extreme cases of charge polarization, using Q3 and Q5 charge multipliers which, as suggested, exhibit charge polarizations 3 and 5 times stronger than that of regular MoS_2. The corresponding PMFs are given in Figure 32(a) for all values of charge multiplier. They were calculated at a pore offset of 2.57nm since pore alignment does not seem to impact the PMF in the interlayer region. The vertical dashed lines in purple and yellow represent Mo and S atoms' positions respectively.

We can clearly see that the lowering of the energy barrier in the interlayer region for Q2 was not coincidental, and is actually caused by increased electrostatic interactions with the MoS_2 walls. Despite the slight increase in the interlayer energy barrier between Q0 and Q1, as we move to higher values of charge polarization a flattening of the interlayer water density distribution occurs. This is also accompanied by an approximation of water molecules to the MoS_2 walls.

We plot in Figures 32(b)-(c) the radial distribution functions between oxygen and molybdenum atoms and oxygen and sulfur atoms, respectively. There is an increase in the value of the RDF at lower values of r for higher values of charge multiplier, particularly in the oxygen-sulfur RDF. That correlates with what was just observed for the PMFs as charge polarization increases. Figure 32(c) in particular indicates that there is a non negligible shift of water molecules towards the membrane's walls for Q2 in comparison to Q1 and Q0, which may be significant in understanding the differences in bilayer flux loss between the three systems.

Our results indicate that stronger electrostatic interactions with inner membrane walls in the MoS_2 bilayer membrane lead to a flattening of water density in the interlayer region. As an isolated factor, this would yield a higher water flow through the membrane and partially explains

the results obtained for the bilayer flux loss in Figures 29(d)-(f). However, changes in the spatial configuration of the confined water bilayer will certainly be accompanied by other changes in the system, therefore further analysis is necessary to confirm this assumption.

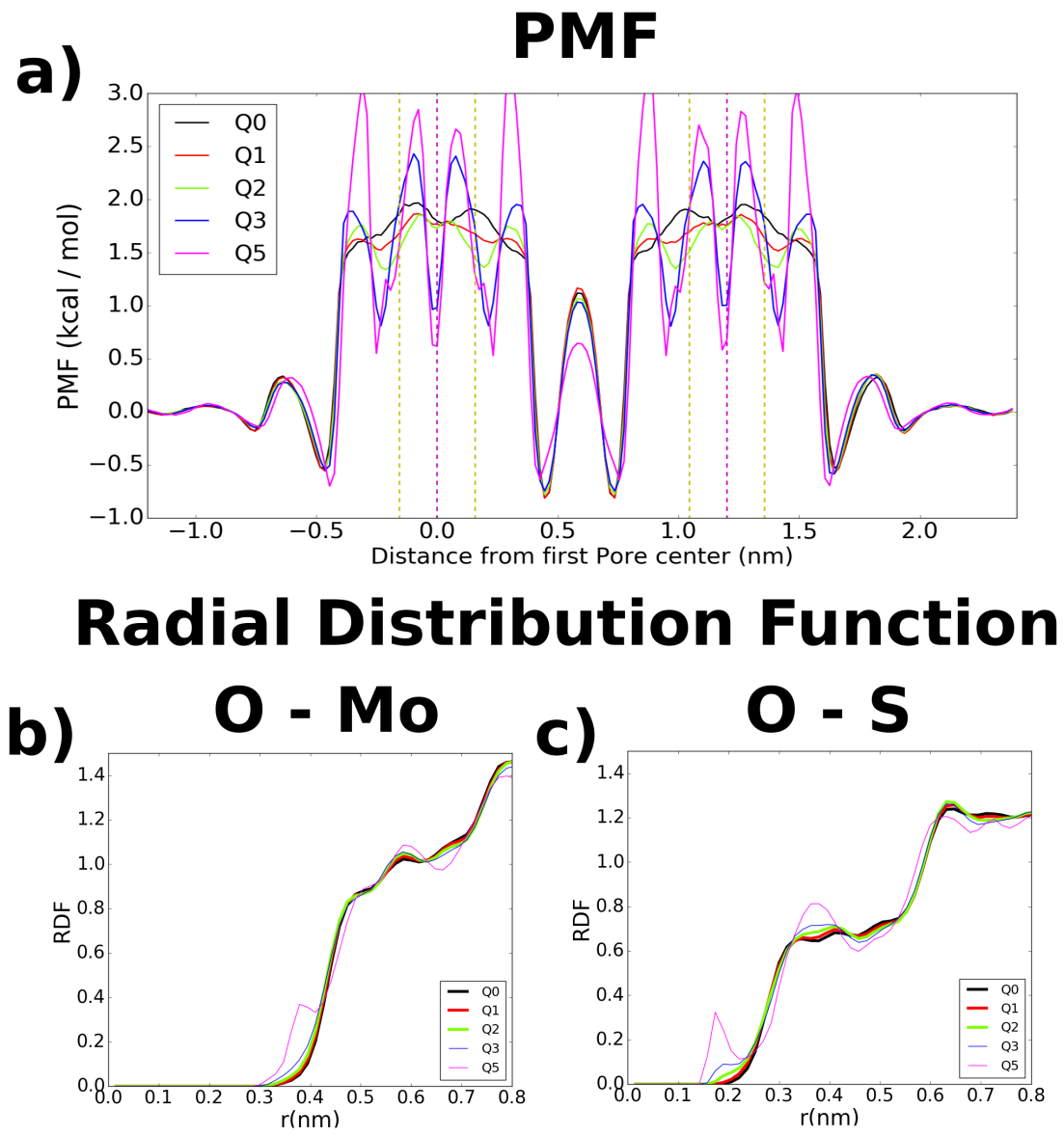

Figure 32: a) PMF at pore offset of 2.57nm for charge multipliers of Q0 (black), Q1 (red), Q2 (green), Q3 (blue), Q5 (pink). The dashed lines in purple and yellow represent the position of Mo and S atoms. Radial distribution functions at different charge multipliers between b) oxygen-molybdenum and c) oxygen-sulfur atoms.

Another property that may also be affected by electrostatic interactions with the MoS_2 walls and the consequent flattening of the water distribution in the interlayer region is the angle of orientation of water molecules. This angle is measured between the water dipole vector and the Z axis. Charge polarization was shown to strongly influence it inside nanopores for monolayer MoS_2 in Figure 18. It is thus natural to expect it to have an effect on the orientation of molecules in the interlayer region.

Figure 33(a) provides a distribution of the orientation of the dipole vectors of water molecules with respect to the Z axis. Dotted lines represent the mean angle of orientation of water molecules in relation to the Z axis, while the shaded regions above and below it represent one standard deviation. The dashed line in black represents the water density in the Q0 system and was introduced to allow for the identification of the water bilayer in the graph, purple and yellow dashed lines represent the positions of Mo and S atoms. We plotted the distributions for the three charge multipliers, Q0, Q1 and Q2 at a fixed offset of 2.57nm. The reason the other offsets are not shown in the graph is that water orientation was shown to be unchanged by the value of pore offset.

The distribution inside the pores was found to be identical to that of monolayer MoS_2 pores (see Figure 18). In quite a surprising result we can see that charge polarization a has negligible influence on the orientations of water molecules in the interlayer region. This indicates that purely geometric effects are responsible for determining the orientation of water molecules in that region.

This can be understood by differences in the structure of pores and membrane walls. In MoS_2 pores both Mo and S atoms are exposed to water molecules, leading to strong electrostatic interactions. However, in the interlayer region only sulfur atoms are exposed. As mentioned before, the partial charges of sulfur atoms have half the magnitude as those of molybdenum. This, combined with screening effects, means the electrostatic interactions between water and MoS_2 in the interlayer are much weaker than inside the pores, and water-water interacion in the interlayer region is significantly stronger.

In order to confirm the predominance of geometric constraints over electrostatic forces we plot in Figure 33(b) the water orientation distributions at charge multiplier Q5, a charge polarization five times stronger than that of regular MoS_2. For comparison we also included the distribution for Q2 and the water density for Q5 is shown as a dashed pink line. We can see that electrostatic interactions between water molecules and the walls have only a mild influence on water orientation even for charge polarizations as strong as Q5. For the water bilayer in the interlayer region, the molecules closer to the walls show a slight change in the angle of its dipole vector, and they now have their hydrogen atoms pointing slightly towards the walls, unlike systems with weaker charge polarizations where they point slightly away from it. These changes, however, do not restrict the movement of water molecules enough to significantly alter water flow as they exhibit a fairly large standard deviation, it may, however, cause the break down of some hydrogen bonds. It is then, very clear that molecules inside the pore are greatly affected by charge polarization while those in the interlayer region retain the same orientation for charge multipiers of Q0, Q1 and Q2 systems, as electrostatic forces are too weak.

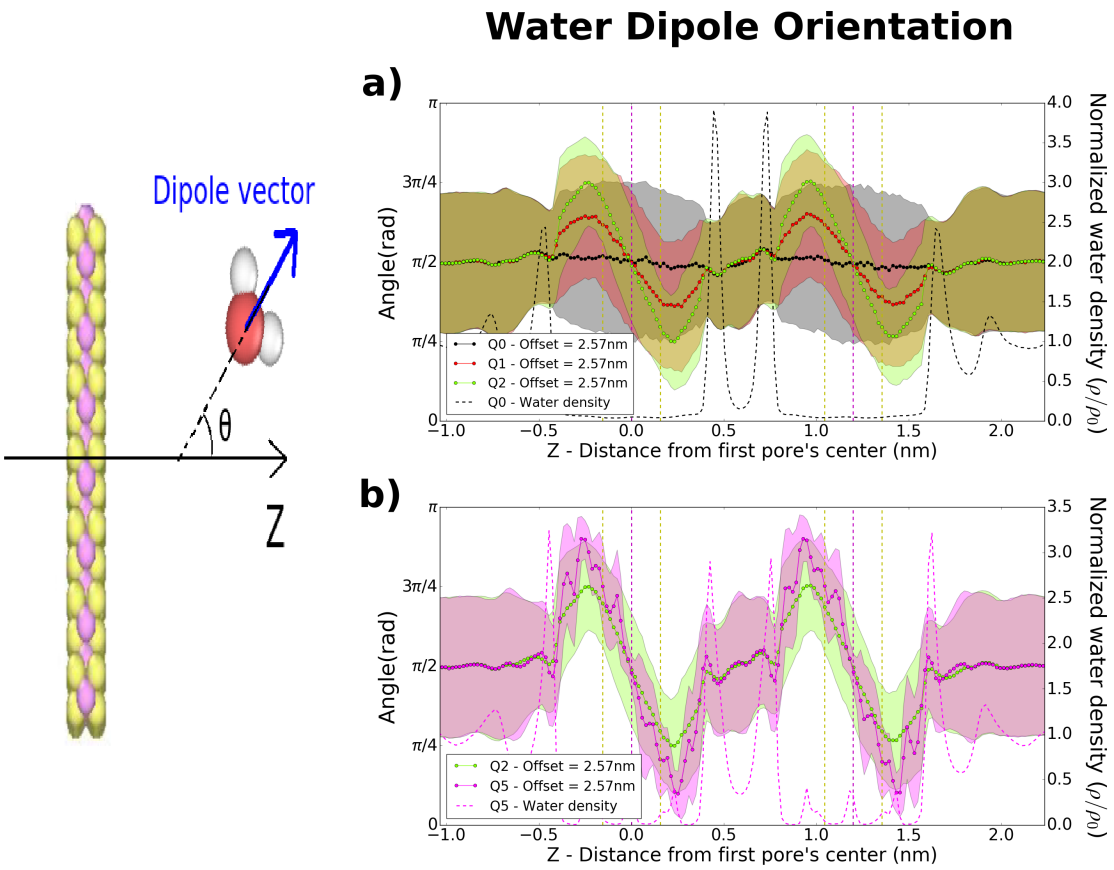

Figure 33: Orientation of the water dipole vectors with respect to the Z axis across the MoS_2 bilayer. Dotted lines indicate the mean angle of orientation and the shaded regions one standard deviation from it. a) Results for charge multipliers of Q0 (black), Q1 (red) and Q2 (green) and b) results for charge multipliers Q2 (green) and Q5 (pink). Dashed lines in purple and yellow represent the position of Mo and s atoms. The dashed curve in black in a) and the dashed curve in pink in b) correspond to the normalized water densities (ρ/ρ_0) for Q0 and Q5 systems respectively.

There is another very important factor not yet considered for bilayer water transport which is the hydrogen bond network in the interlayer region. We showed in section 3.1 that charge polarization heavily disturbs the hydrogen bond network of water inside an MoS_2 nanopore and leads to a decrease or even a complete halt of water flow. Since water is greatly affected by confinement between the MoS_2 sheets, we expect the interlayer hydrogen bond network to differ from that of bulk water, since it has been shown that water confined in nanoslits tends to form hydrogen bonds mostly within the slit's 2D plane and very rarely in the direction perpendicular to the walls [75].

In Figure 34(a) we plotted the average number of hydrogen bonds per water molecule in the interlayer region as a function of charge multiplier. We can see clearly that there is a slight drop in the number of hydrogen bonds when we go from Q1 to Q2, and they continue to decrease for Q3 and Q5. This indicates that electrostatic interactions with the MoS_2 walls might be weakening hydrogen bonds and even breaking a few of them, but that only becomes significant for very high values of Q. Q0 and Q1 membranes, however, exhibit equal average numbers of hydrogen bonds per molecules. It is important to note that the number of hydrogen bonds per molecule that are broken in the interlayer region is much samller than inside the nanopores. Even for Q5, only 0.4 bonds per molecule are broken in the interlayer region, a similar number of broken bonds are observed inside 0.97nm/Q1 monolayer pores in Figure 19(c) with the highest reduction observed for 0.97nm/Q2 pores, where around 1.5 bonds per molecule are destroyed inside the nanopore.

In order to understand in detail the orientation of hydrogen bonds in the interlayer reigon, we plot in Figure 34(b) the histograms of the Z component of the center of mass of hydrogen bonds, schematized in Figure 34(c) and defined by the equation:

$$\mathbf{CM}_z = \frac{z_{Oa} + z_{Od}}{2} \, . \tag{13}$$

where z_{Oa} and z_{Od} represent the Z coordinate of the oxygen atoms of the acceptor and donor molecules and $\mathbf{CM}_z$ represents the Z component of the center of mass of the water molecules involved in the hydrogen bond. The Z direction is the one perpendicular to the MoS_2 sheets. By measuring this for all hydrogen bonds in the interlayer region we obtain the distributions in Figure 34(b), where the X axis represents the distance in the Z axis from the center of the central Mo layer of the first nanopore and the Y axis the probability density of observing a hydrogen bond with said Z component of center of mass. All distributions were normalized to yield an integral of one. We show results for charge multipliers ranging from Q0 to Q5 and results are only shown here for the largest value of pore offset since it showed to not affect the results.

This measurement gives us an idea of the orientation of hydrogen bonds, we expect most of them to form in between molecules belonging to the same water layer, yielding a center of mass located within the Z-range of that water layer. However, some molecules form hydrogen bonds with waters in the opposite water layer, and those represent the central peak in the histogram located between both layers. The histogram shows that an increase in the value of the charge multiplier decreases the height of the three peaks and flattens the curve. In this case the difference between Q0/Q1 histograms and that of Q2 is more visible and as we move to stronger charge polarizations we see a further flattening of the distribution. This is consistent with the observation made for the PMF in Figure 32(a) which indicates that a higher charge multiplier leads to a more bulk-like water distribution, where hydrogen bonds are more homogeneously distributed in space. This flattening is followed by a slight dilation of the curves, caused by water molecules getting closer to the MoS_2 inner walls.

Hydrogen Bonds - Interlayer Region

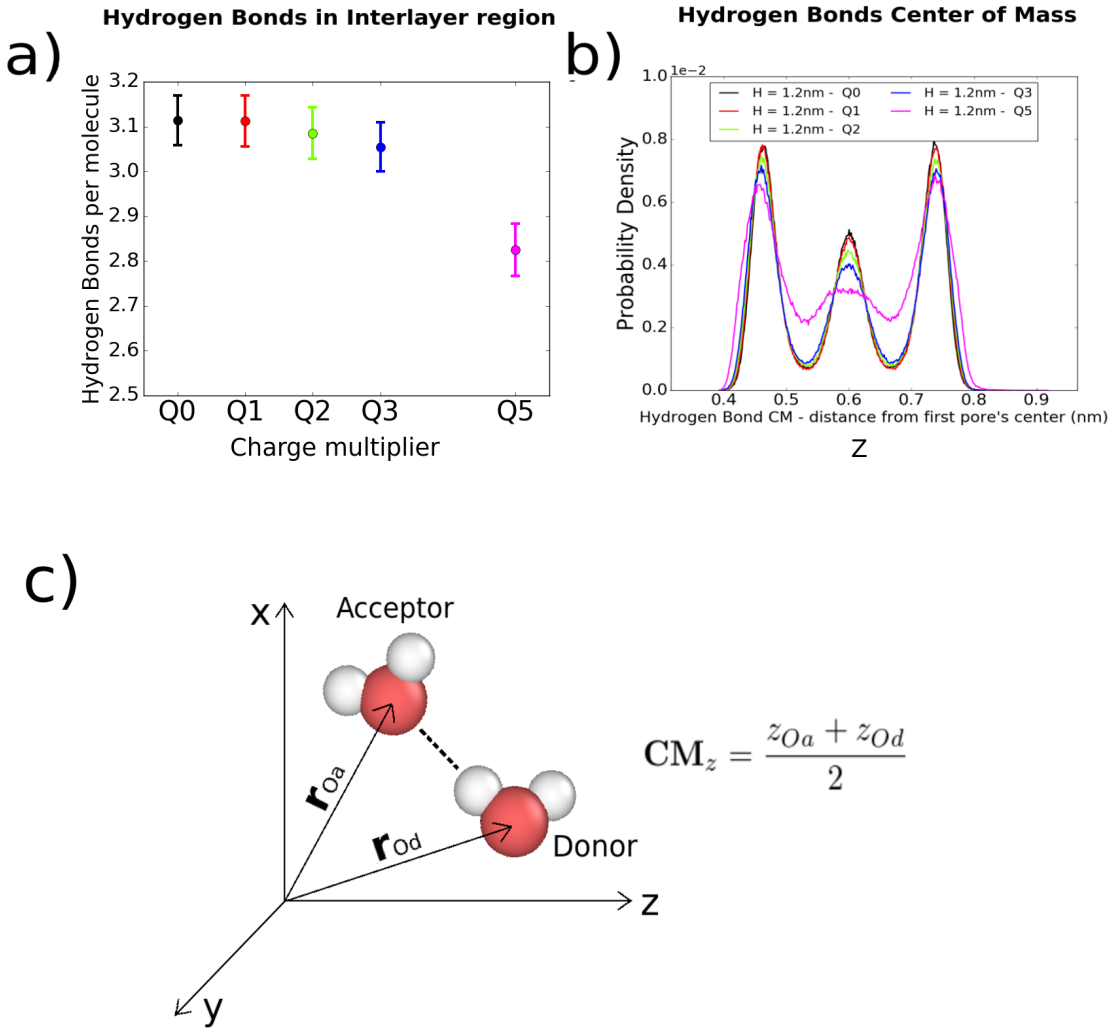

Figure 34: a) Average number of hydrogen bonds formed by water molecules in the interlayer region as a function of charge multipier. b) Histogram of the position of the hydrogen bonds' center of mass in the Z direction for water in the intelayer region. c) Illustration of the calculation of the center of mass in the Z direction..

We have just shown that electrostatic interactions with MoS_2 walls lead to a disorganization of water in the interlayer region in the direction perpendicular to the MoS_2 sheets (Z direction). It is, however, equally important to characterize the changes in water distribution in the 2D plane parallel to the walls (XY-plane). To visualize the organization of water molecules inside the interlayer region in the XY plane we provide in Figure 35 the oxygen density maps of one of the two water layers forming the confined water bilayer. Brighter colors correspond to higher oxygen densities, represented in g/cm^3, and the X and Y axis are given in nm. Figures 35(a)-(e) correspond to charge multipliers Q0, Q1, Q2, Q3 and Q5 respectively. All maps were made at a fixed offset of 2.57nm and at zero applied pressure as both parameters were shown not to significantly influence results.

In all maps we can see the pore represented as a bright spot on the lower left. We can see that the pore has limited effect on water distribution around it, except for its most immediate vicinity. We note that the second pore has a small effect on water distribution and it can be seen as a slightly darker spot near the top right of the plots. We can see that water molecules organize themselves in different ways depending on the charge polarization of the MoS_2 walls. For Q0 (Figure 35(a)), they form a clear honeycomb structure with hexagons with sides roughly the size of the distance between two consecutive Mo atoms. As the charge multiplier increases water molecules become increasingly disorganized to the point that at Q2 (Figure 35(c)) they are smoothly distributed along the XY plane. This is a clear indication that the disorder induced on water's spatial distribution in the interlayer region by electrostatic forces is not restricted to the Z axis but is in fact more pronounced in the XY plane.

We chose to include higher values of charge multiplier as they clarify what is happening to water molecules in the interlayer region as charge polarization increases. We can see that for Q3 (Figure 35(d)) water molecules are still smoothly distributed in space, but as we increase the charge polarization of MoS_2 five-fold, as in Q5 (Figure 35(e)), we can see that a new arrangement of molecules has been formed. The density map now displays a pattern analogous to a triangular lattice, where the bright dots are actually located precisely at the center of the hexagons observed for Q0, indicating that in Q5 the water distribution is actually the inverse of that of Q0. That indicates that water molecules tend to accomodate around different sites of the MoS_2 walls depending on the strength of its charge distribution.

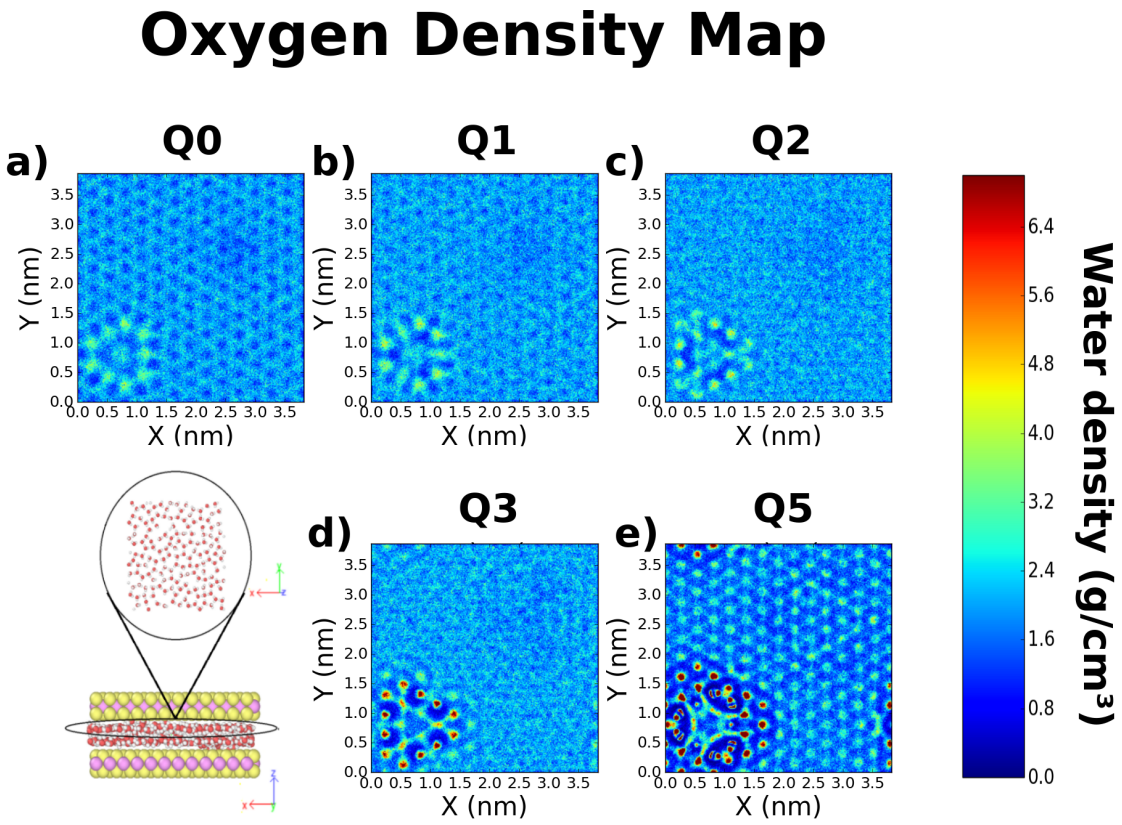

Figure 35: Oxygen density maps in the XY plane for a single water layer composing the water bilayer in the interlayer region. Brighter colors indicate higher water densitites. Maps calculated at pore offset of 2.57nm and zero applied pressure for charge multipliers of a) Q0, b) Q1, c) Q2, d) Q3 and e) Q5.

A clearer visualization of what happens to water molecules near the walls of MoS_2 sheets as the charge multiplier increases can be seen in Figure 36. In Figure 36(a) we plot the 2D radial distribution function in the XY plane between oxygen and Mo atoms and in Figure 36(b) for oxygen and S atoms. Details on the calculation of 2D RDFs are given in section 2.6, it is essentially the same procedure used for the 3D one but the Z direction is not taken into account. The XY plane corresponds to the plane parallel to the MoS_2 sheets. Unlike the 3D RDF in Figures 32(b)-(c), the 2D RDF only takes into account the X and Y coordinates of atoms, therefore it does not tell us the distance between oxygen and Mo/S atoms since if disregards the Z direction, the one orthogonal to the MoS_2 planes. It does, however, tell us what sites in the MoS_2 walls water molecules prefer to occupy. We define two kinds of sites, the Mo-sites, located above Mo atoms, and the S-sites, located above S atoms, as is shown in the illustration at the bottom of Figure 36. We include all five charge multipliers again, represented by the usual color code. The X-axis is given in nm and the vertical dashed lines in each graph represent the distance from the nearest opposite type atom (Mo or S).

There is a clear shift in the preferred sites for the localization of oxygen atoms in MoS_2. Since this is a 2D RDF it is important to clarify that the Mo site does not mean the oxygen atoms stay closer to Mo atoms than to S atoms, in fact water molecules in the interlayer region are always closer to an S atom than to an Mo atom, given that the walls are made up of a sulfur layer. The Mo-sites refer to sites with equal XY coordinates to an Mo atom, which in MoS_2 corresponds to a central point between three neighboring sulfur atoms, an S-site on the other hand indicates an

oxygen atom directly above an S atom.

For the system with no charge polarization (Q0) water molecules exhibit a slight preference for Mo-sites over S-sites, which manifests in the 2D RDF as an oscillatory pattern with maxima near Mo-sites and minima at S-sites. As charge polarization increases more oxygen atoms previously located at Mo-sites move away from it and towards S sites. For Q2, we observe a nearly flat profile for the 2D RDF, indicating a more disorganized water layer in the XY plane. In fact, for Q1 and Q2 there is a shift of the maximum of the 2D RDF, now located in between Mo and S sites. If we turn our attention to the more extreme cases of charge polarization represented by Q3 and Q5 we observe an inversion in the pattern observed in the 2D RDF for Q0 systems, with maxima now located at or near S sites. For Q5 there is a very tall peak for the oxygen-sulfur RDF located at r=0nm with an amplitude of 2.0 that is cut out of the graph due to its scale, indicating a very high preference of oxygen atoms for S-sites.

These results indicate a competition between geometric and electrostatic effects governing the spatial distribution of water molecules on the XY plane. For an MoS_2 wall with no charge polarization (Q0) water molecules stay preferably at Mo sites, located in between three neighboring sulfur atoms. As charge polarization is introduced into the system oxygen atoms move away from Mo sites towards S sites but a large fraction of them tend to stay in between both sites. There is already a significant shift between Q0 and Q1 and it becomes more pronounced as the charge multiplier increases, going through a highly disordered distribution for Q2 and Q3 until most water molecules are located at S-sites as in Q5. It might seem contradictory for oxygen atoms to migrate closer to highly negatively charged sulfur atoms, however one should keep in mind that many other competing factors are present, such as hydrogen bonds, electrostatic interaction with hydrogen atoms and geometric constraints coming from MoS_2's geometry which define the overall distribution of water molecules next to MoS_2 walls.

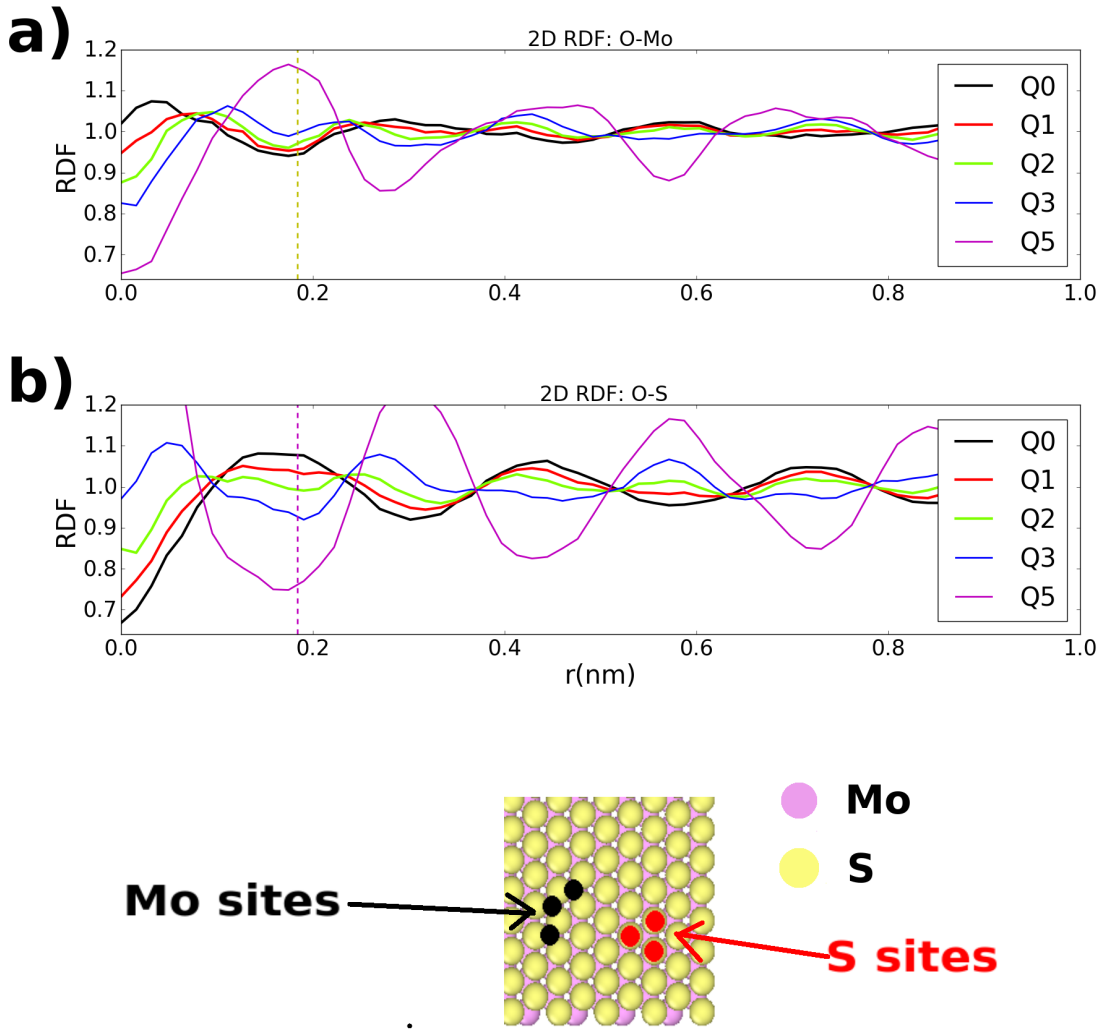

Figure 36: 2D radial distribution function calculated for one single water layer forming the water bilayer in the interlayer region, calculated at pore offset of 2.57nm at zero applied pressure. RDFs obtained between a) oxygen-molybdenum atoms and b) oxygen-sulfur atoms at different values of charge multiplier. Dashed lines in purple and yellow represent the distance from the nearest opposite type atom, Mo and S respectively.

We have just established in Figures 34, 35 and 36 that the charge distribution of the MoS_2 membrane tends to disorganize water molecules in the interlayer region in all directions. Water between two Q0 MoS_2 walls is therefore more organized than in Q1, which, in turn, is more organized than Q2. We have also seen that increased charge polarization leads to stronger electrostatic interactions between water and MoS_2, which causes a slight breakdown of hydrogen bonds in the interlayer region (Figure 34(a)), while also inducing a flattening in the distribution of hydrogen bonds' center of mass in the Z direction (Figure 34b).

The PMFs in Figure 31 have shown that water molecules have a hard time moving in the direction perpendicular to the MoS_2 sheets - the Z direction - due to the height of the potential energy barrier between both water layers. The same can be said of the hydrogen bonds' center of mass distributions in Figure 34(b), where increased charge polarization leads to a lower bias towards certain values as all peaks in the distribution decreased in height.

We propose this decrease in anisotropy as the mechanism explaining the overall trend of decreasing bilayer flux loss as a function of charge multiplier in Figures 29(d)-(f). As the system becomes more isotropic it approaches the structure of bulk water, however, if coulombic interaction become too strong the breakdown of hydrogen bonds and coulombic attraction towards the inner walls slows down water flow again.

Our results, however, do not explore a wide range of change in the aforementioned properties since most differences in anisotropy in the interlayer region of the system are mild when we compare

Q0 and Q2 systems. The rest of this chapter is dedicated to studying more extreme examples than the ones obtained so far in order to test the proposed mechanism. One may be tempted to simulate the systems Q3 and Q5, however the flattening of the PMF in the Z direction is accompanied by the emergence of a new kind of water structuring in the XY plane as seen in the 2D RDFs in Figure 36. On top of that, high values of charge polarization lead to extremely low water flowrates due to intense electrostatic interactions inside the nanopores (see section 3.1), which would make simulations extremely computationally demanding.

A different way to obtain a more disorganized system in the interlayer region is by increasing the membrane's separation. We have so far only worked with a fixed membrane separation of 1.2nm, measured from the center of Mo atoms in both MoS_2 sheets. Therefore, we introduce two new systems, consisting of membranes with layer separations of 1.28nm and 1.35nm. We chose the letter H to represent the layer separation and this symbol will be used throughout the text.

A good visualization of what happens to water in the new systems is given in Figure 37 where we plot the PMFs for the new wider membranes. Each subplot displays PMFs for Q0, Q1 and Q2 membranes. The full lines represent the PMF at a fixed value of layer separation and pore offset, while the dashed lines represent the PMF of the original membrane with H=1.20nm, which are shown for comparison purposes. The vertical dashed lines in purple and yellow represent the new positions of Mo and S atoms for the new value of H. Figures 37(a)-(b) depict PMFs for the membrane with layer separation of 1.28nm for the three values of charge multiplier, Q0, Q1 and Q2 and pore offsets of 0.0nm and 2.57nm respectively, while Figures 37(c)-(d) display the same thing but for a layer separation of 1.35nm.

The most striking difference between membranes with different layer separations is in the extrema of the PMF in the interlayer region. For a layer separation of 1.28nm we see that the water bilayer maintains a similar profile to the 1.2nm separation one, however the potential energy barrier between both layers has become lower and both layers have widened a bit. This is a clear sign of disorganization of the water bilayer in the Z direction, similar to the one caused by electrostatic forces in Figure 32 but considerably more intense, indicating a possible shift to a more bulk-like water distribution. For the wider 1.35nm layer separation we see a striking difference for the potential energy profile in the interlayer region. We still observe a water bilayer structure, however, the potential energy barrier between layers has diminshed significantly and the shape of the layers is now different, indicating the possible emergence of a third layer if both MoS_2 sheets are separated further, something that has been reported in literature [75]. We also observe in these systems a decrease in the potential energy barrier between both water layers caused by an increase in the charge multiplier.

Figure 31 also indicates the PMF inside the pores is not completely insensitive to changes in the confined water bilayer. Slight changes to the pore's potential energy profile are caused by the increase of layer separation and pore offset in Q1 and Q0 systems, but are most intense for Q0. It is interesting to note though, that in Figure 37(b), for the H=1.28nm membrane at pore offset equal to 2.57nm, the energy profile for the Q0 pore has become much smoother than at any other system. Other changes can be identified but there does not appear to be an easily recognizable pattern in the changes of the pore PMFs and we will not discuss this phenomenon further. The interaction between waters in the pore and waters in the interlayer region could very well be an important factor in understanding water transport in bilayer MoS_2 membranes, however from now on we will only focus on the confined water bilayer.

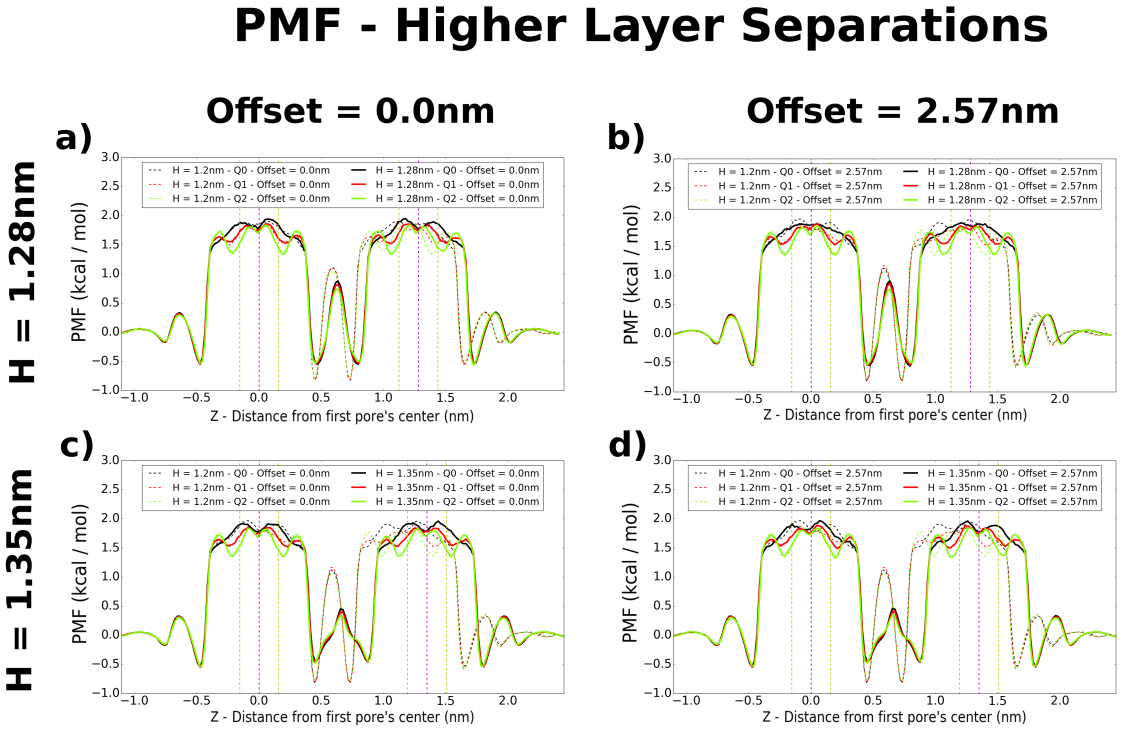

Figure 37: Potential of mean force at different values of charge multiplier, Q0 (black), Q1 (red) and Q2 (green) for membranes with higher layer separations. (Top) PMFs for membrane with layer separation of 1.28nm for pore offsets of a) 0.0nm and b)2.57nm. (Bottom) PMFs for membrane with layer separation of 1.35nm for pore offsets of a) 0.0nm and b)2.57nm. Dashed curves represent the PMF for the original membrane with layer separation of 1.20nm and the vertical dashed lines in purple and yellow represent the positions of Mo and S atoms respectively.

We now have a better understanding of how water organizes itself inside the interlayer region as its width is increased. We will now analyze its effect on the hydrogen bond network and see how it compares to the H=1.2nm system. Figure 38(a) shows the average number of hydrogen bonds per water molecule as a function of the membrane's layer separation. Different colors represent the three values of charge multiplier considered. All measurements come from simulations performed without applied pressure and a fixed pore offset of 2.57nm, as both factors showed little influence on the results. We see that increasing layer separation has a minimal effect on the number of hydrogen bonds that each water molecule forms. This indicates that the breakdown of hydrogen bonds is predominatly caused by electrostatic forces.

The number of hydrogen bonds per molecules may not have shown a big dependency on layer separation, it does, however, have a significant impact in its orientation. Figures 38 (b), (c) and (d) show plots of the distribution of the hydrogen bonds' center of mass in the Z direction for layer separations of 1.20nm, 1.28nm and 1.35nm respectively. Each subplot shows the histograms for the simulated values of charge multiplier at a fixed pore offset of 2.57nm, since this quantity showed negligible influence on the distribution. These simulations were also performed at zero applied pressure since it showed negligible effect on it as well.

The effect of increasing layer separation is very noticeable, causing the histograms to become flatter, confirming that it does indeed diminish the influence of confinement effects, allowing for the formation of more hydrogen bonds between water molecules at various distances from each other in the Z direction. This leads, as mentioned previously, to a more bulk-like state that shows less bias towards certain orientations of hydrogen bonds. We can also see on all three graphs that increasing the charge polarization of MoS_2 still has a flattening effect of the distribution but at a much more modest intensity than increasing layer separation does.

We also include in Figures 38(e)-(g) the 2D RDFs at different values of layer separations. The RDFs on top are between oxygen and molybdenum and the ones at the bottom between oxygen and sulfur. Each of the three subplots represents a fixed value of charge polarization and different values of layer separation are represented by different colors. These curves show us that an increased layer separation has minimal effect on the organization of water molecules in the plane parallel to the MoS_2 sheets and its preference for Mo or S-sites.

We can conclude from the results that water configuration in the XY plane is controlled almost exclusively by electrostatic forces between water and MoS_2 and its surface geometry, being roughly

independent from layer separation. On the other hand, the organization of water molecules and its hydrogen bond network in the direction orthogonal to the MoS_2 planes is more strongly affected by the membrane's layer separation, but still suffers non negligible contributions from MoS_2 electrostatic forces.

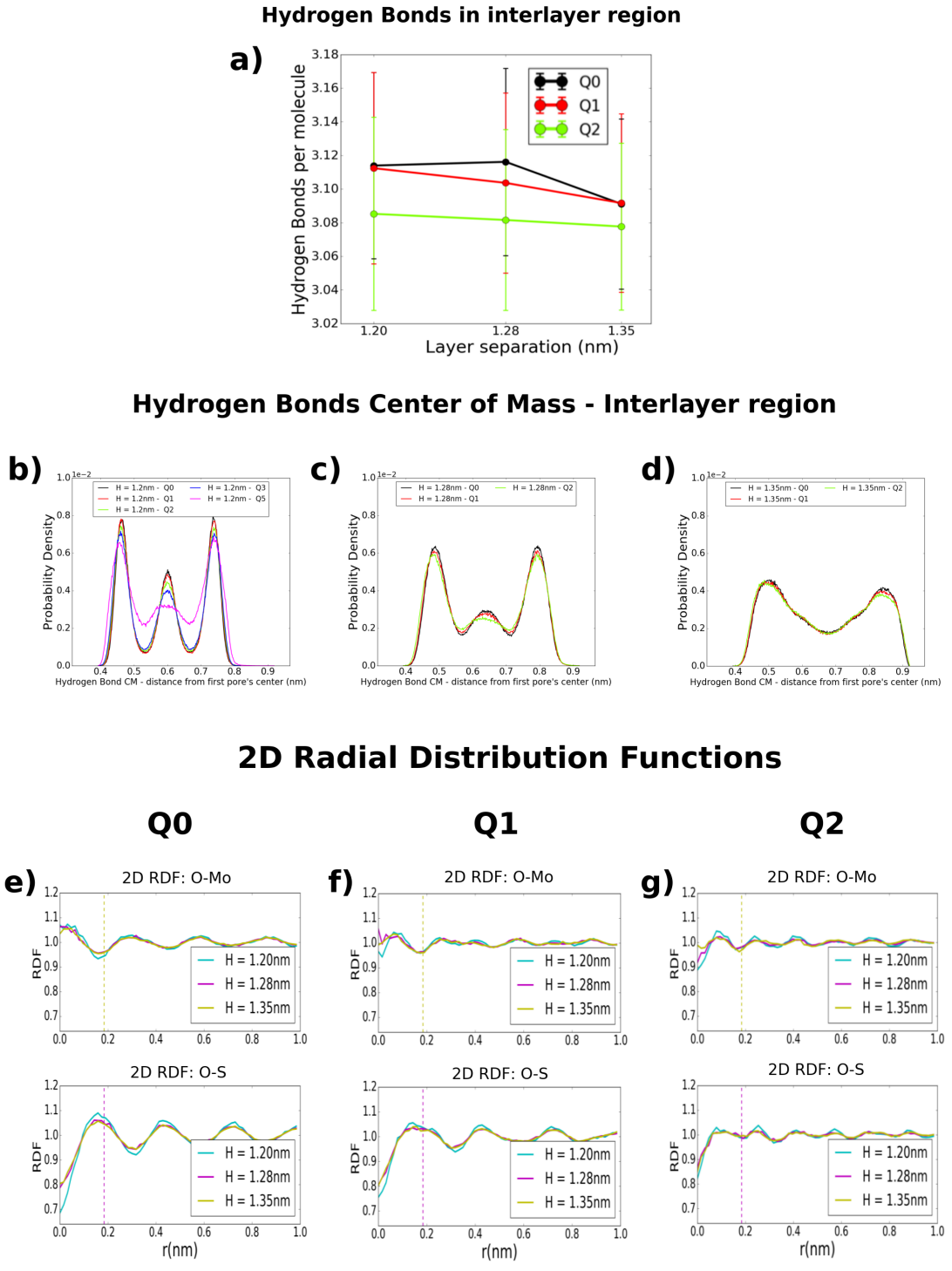

Figure 38: (Top) a) Average number of hydrogen bonds formed by water molecules in the interlayer region as a function of layer separation for charge multipliers of Q0 (black), Q1 (red) and Q2 (green). (Middle) Histograms for the center of mass in the Z direction of the hydrogen bonds formed in the interlayer region at different values of charge multiplier: Q0 (black), Q1 (red), Q2 (green), Q3 (blue) and Q5 (pink) for membranes with layer separations of a) 1.20nm, b) 1.28nm and c) 1.35 nm. (Bottom) 2D radial distribution functions for different layer separations 1.20nm (cyan), 1.28nm (purple) and 1.35nm (yellow) at e) Q0, f) Q1 and g) Q2 charge multipliers. Vertical dashed lines in purple and yellow represent the distance from the nearest opposite type atom, Mo and S respectively.

We have established that even minor increases in layer separation lead to a significant degree of disorganization in the water bilayer confined between two MoS_2 sheets and brings it closer to a bulk-like state. If our proposed mechanism for water flow within the bilayer membrane is correct, the wider membranes should exhibit higher water fluxes and therefore a lower bilayer flux loss. In order to confirm this we carried out reverse osmosis simulations of the H = 1.28nm and H = 1.35 nm membranes, with pore offsets of 0.0nm and 2.57nm at an applied pressure of 250MPa. Only one production run by system was considered, but it was nonetheless enough to produce interesting results.

The bilayer flux loss was plotted in Figure 39 as a function of layer separation. Each subplot in Figures 39(a), (b) and (c) corresponds to a fixed value of charge multiplier, Q0, Q1 and Q2 respectively, and blue and green lines represent pore offsets of 0.0nm and 2.57nm. We can clearly see that for all values of charge multiplier and pore offset, an increase in layer separation from H=1.2nm to H=1.28 or H=1.35nm was accompanied by an increase in water flowrate, bringing the bilayer flux loss closer to the value of 0.5 predicted by classical hydrodynamics. These results are obviously not the most accurate since only one production run was carried out per system, but it confirms an overall trend for the system. As layer separation increases the water bilayer between the MoS_2 walls becomes more disorganized, rendering water molecules freer to form hydrogen bonds with other water molecules at any positions along the Z dimension. This, in turn, lowers the potential barrier within the interlayer region and allows for a higher number of water molecules to reach the permeate reservoir, leading to a higher water flowrate.

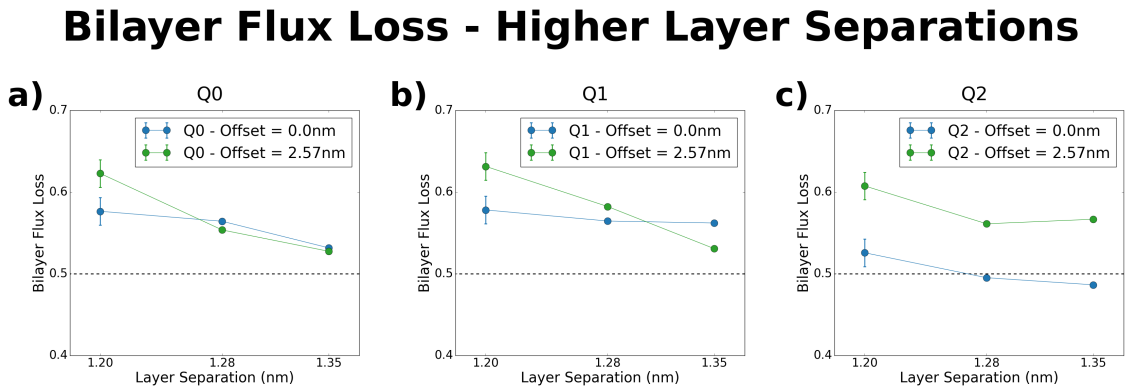

Figure 39: Bilayer flux loss as a function of layer separation at charge multiplers of a) Q0, b) Q1 and c) Q2. Blue and green lines represent 0.0nm and 2.57nm pore offsets respectively and the dashed line represents the result predicted by classical hydrodynamics.

4.2 Summary

In this chapter we provided an extensive analysis of phenomena governing water transport across bilayer MoS_2 membranes. In our simulations we altered the charge distribution of MoS_2 in order to generate hypothetical membranes with no charge polarization (Q0) or doubled charge polarization (Q2). We saw that Q1 membranes have higher water flowrates than Q2 membranes, which in turn have higher flowrates than Q0 (Figure 29(a)-(c)). This is a different order than the one observed for the monolayer membranes in section 3.1. Pore offset was also shown to decrease water flowrate in all cases.

By dividing the flowrate of bilayer membranes by its corresponding monolayer version, we calculated the bilayer flux loss. This quantity indicated that all bilayer membranes considered exhibit a reduction in the flow of water superior to 50%, the value predicted by classical hydrodynamics. The only system approaching 50% reduction was the Q2 membrane with zero pore offset. The graphs of bilayer flux loss as a function of charge multiplier (Figure 29(d)-(f)) indicate a decreasing pattern as Q increases, particularly when we move from Q1 to Q2.

We showed that increasing pore offset forces water molecules to travel longer paths within the bilayer region. There is also a significant correlation between the mean water passing times and water flowrate, as shown in Figure 30(i), which suggests interactions with MoS_2's inner walls may be behind the differences in bilayer flux loss.

PMFs for water (Figure 31) indicate little changes in the potential energy barriers inside the pores, except for small variations in Q0 for pore offsets 0.96nm and 2.57nm. A water bilayer forms in between both MoS_2 sheets, separated by a high potential energy barrier. There is a hint of a lowering in the potential energy barrier when charge polarization is doubled (Q2), but

the energy profile in the interlayer system remains mostly unchanged. Figure 32 showed that - by including more extreme charge polarizations of Q3 and Q5 - electrostatic interactions between water molecules and the MoS_2 inner walls attract water towards the walls and flattens the potential energy profile in the interlayer region. The orientation of water molecules with respect to the Z axis, however, remains mostly unchanged unless a very high charge multiplier (Q5) is introduced (Figure 33).

In Figure 34 we show that electrostatic interactions disturb the hydrogen bond network of water, breaking up a few hydrogen bonds and allowing for the formation of more bonds with less orientational restriction. Figure 35 and Figure 36 show the disorganizing effect charge polarization has on water organization on the plane parallel to MoS_2 sheets. This is caused by increased attraction of oxygen atoms towards S-sites in MoS_2, away from Mo-sites. While for Q5 water molecules have fully moved from Mo to S-sites, Q2 appears to be exactly in between both cases, suggesting water is more disorganized than in Q0 and Q1 membranes not only in the Z direction but also in the XY plane. These are signs of increased isotropy in the interlayer region as the charge multiplier increases from Q0 to Q2, and therefore a more bulk-like configuration. This leads to the proposition of a mechanism to explain the dependency of water flow in the interlayer region on charge multiplier: decreased anisotropy in the interlayer region allows for the formation of more hydrogen bonds along the direction perpendicular to MoS_2 planes - the direction of water flow - which in turn lowers the potential energy barrier between the two water layers and increases the water flowrate.

In order to confirm the mechanism we simulate membranes with larger values of layer separation, 1.28nm and 1.35nm, in contrast to the original layer separation of 1.2nm. Widening the interlayer region decreases anisotropy of the water density in the Z direction (Figure 37), as well as on the distribution of the hydrogen bonds' center of mass in the same direction 38(b)-(d). Increased layer separation did not, however, lead to higher isotropy in the distribution of water molecules at the MoS_2 walls as evidenced by the 2D RDFs in Figures 38(e)-(g).

Finally, we showed in Figure 39 that the bilayer flux loss decreases with layer separation in all systems. This indicates that the proposed mechanism is consistent, at least in the statement that increased isotropy in the direction perpendicular to MoS_2 planes leads to a more bulk-like water in the interlayer region and increases water flow across the membrane. Our results do not confirm that higher isotropy of water distribution in the plane parallel to MoS_2 actually affects water transport, but also does not disprove it. Further analysis would be necessary to either add or discard this contribution to our proposed mechanism.

We conclude that results in Figure 29 can be explained as follows: stronger electrostatic interactions with the inner walls of the bilayer MoS_2 membrane lead to less restriction to the orientation of hydrogen bonds in the Z direction, which causes an increasing isotropy of the configuration of water in the interlayer region. This leads to a lower bilayer flux loss as charge polarization in the membrane increases. This allows water molecules to flow more easily between the two layers of water in the interlayer region which allows for higher water flowrates that are close to those predicted for classical membranes.

5 Conclusion

In this work we shed some light on the influence of pore geometry and chemistry on water and ion transport across nanoporous MoS_2 monolayer membranes and water transport for bilayer MoS_2 nanoporous membranes. By varying pore geometry and its charge distribution we were able to decouple the electrostatic and geometric contributions regulating the membranes' salt rejection and water permeability. We wanted to understand which phenomena are determining of MoS_2's performance as a RO desalination membrane.

The nanopores we studied do not present the best overall performance as desalination devices, and perform roughly an order of magnitude worse than the most efficient MoS_2 nanopores in literature [36, 37]. It is, however, important to understand transport phenomena across different kinds of MoS_2 pores, as fabrication of nanopores with specific geometries can be tricky, and undesired pore shapes may appear. Pore functionality has also been shown to increase ion selectivity [10], so these kinds of pores could play a role in separating monovalent and divalent ions for example. On top of that, many other applications for MoS_2 nanopores are being considered, such as DNA sequencing [76] and molecule separation [77], for which such pores may show to be useful.

By varying MoS_2's charge distribution in our simulations we were effectively simulating hypothetical materials that do not exist in nature. This approach was justified as it provided valuable information on how electrostatic forces influence water and ion transport across the nanopores. There is, nonetheless, a real world significance to such altering in MoS_2's charge distribution. MoS_2 belongs to a family of materials called transition-metal dichalcogenides (TMD). These materials have a chemical formula of the form MX_2, where M represents a transition-metal atom and X a chalcogen atom. Materials such as as $MoSe_2$, $MoTe_2$, WS_2 and WSe_2 also belong to the TMD family. TMDs form layer stacked geometries similar to MoS_2 and graphene and can therefore be made into monolayers relatively easily, either by exfoliation [27] or by actually growing a monolayer using techniques like chemical vapor deposition (CVD) [28].

Charge distributions on TMDs arise from differences in electronegativity between both atom types. This means that different TMD materials will exhibit nearly identical geometries with varying strengths of charge polarization. This is a real life analogous to the manipulation of the charge multiplier Q of MoS_2 in our simulations.

Our approach not only provides fundamental insights on physical mechanisms behind transport phenomena inside MoS_2 nanopores, it also allows for the determination of the optimal charge distribution on a TMD monolayer and the potential identification of more efficient TMD nanopores for water desalination. It has been suggested by the findings made by Shen, et al that $MoSe_2$ nanopores may outperform MoS_2, exhibiting around 70% higher water fluxes while maintaining 100% salt rejection [78]. The difference in electronegativity in $MoSe_2$ is slightly higher than in MoS_2, meaning that $MoSe_2$ nanopores are equivalent to an MoS_2 nanopore with charge multiplier $Q > 1$. These results have, however, been contested by Farimani et al [37]. It is important to remember that although TMDs exhibit very similar geometries, when carrying out molecular dynamics simulations they will posses different Lennard-Jones parameters, reflecting their differing atomic radii. The geometry is therefore not perfectly conserved as we change from one TMD to another. Aluru et. al actually provided a brief analysis on the influence of LJ parameters of MoS_2 on desalination performance while preserving its charge distribution. Their results suggest that the type of transition-metal chosen for the TMD plays a bigger role on its desalination performance than the material's chalcogen atoms, due, exclusively, to geometric effects [36].

Most literature conducted on TMD nanopores is focused on MoS_2, however some studies have been carried out for other materials such as $MoSe_2$ [37, 78] and WS_2 [79, 80]. It is important to perform more computational and experimental research on other TMDs in order to identify the best possible candidates for water desalination membranes.

Our simulations demonstrated that a competition between water-MoS_2 electrostatic interactions and the water-water hydrogen bond network can acurately describe water transport across MoS_2 nanopores of diameter 0.97nm and 1.33nm, which is in accordance with the work done by Abal et. al [62]. We showed how coulombic interactions with MoS_2 affect water molecules' distribution and arrangement inside the nanopores, and how that led to higher pore hydrophilicity but also to geometrical constraints which limit the formation of hydrogen bonds, which are highly dependent on molecular distances and orientation angles. Hydrogen bonds are necessary in order to balance out electrostatic attraction of water's oxygen atoms towards Mo terminations in the nanopores. Increased charge polarization in the pores simultaneously increases such attractive forces and breaks down hydrogen bonds. Our results suggest that regular MoS_2 (Q1) actually balances out the contributions from pore hydrophilicity and the breakdown of hydrogen bonds to yield a high water flux, higher than for hydrophobic MoS_2 pores (Q0) or doubly charged ones (Q2). The knowledge of such underlying phenomena allows for a smart design of nanoporous materials in order to maximize water flow. Hydrophobic MoS_2 pores exhibit a water flowrate with

a lower slope with regards to pressure than hydrophilic MoS_2, we have no explanation for why that is, however, it may impact the extrapolation that is made from our results at high pressures to predict water flow at realistic pressures of ∼10MPa. It is possible that at such pressures water flows faster for Q0 pores than for regular MoS_2, but further simulations would be necessary in order to elucidate this question.

We also showed how salt ions compete with water molecules for space inside the nanopores and how that leads to a decrease in water flux. As the pore becomes more hydrophilic, more ions tend to occupy its interior, leading to a reduction in the mean number of water molecules inside it. In the case of MoS_2 pores, this led to hydrophobic pores (Q0) now exhibiting higher water fluxes than regular MoS_2 (Q1). Water molecules in charged nanopores were shown to prefer to occupy sites in the pore which are also energetically favorable for Cl^- ions, which further decreased water flux as regular MoS_2 (Q1) and Q2 nanopores have high affinity for such ions. The impact of salt ions on water flux across nanopores is sometimes overlooked, it introduces a third component to the competition of factors found to regulate water transport across the nanopore in pure water systems. Understanding how ion transport across the pores influences water transport is key in designing more efficient nanopores for desalination applications.

Concluding the study of monolayer MoS_2 nanopores we provided an analysis of how pore geometry and charge distribution impact ion transport across the pores. We observed that the smaller, 0.97nm diameter, pores exhibit 100% salt rejection at low pressures, however, the hydrophobic MoS_2 pore (Q0) exhibited a higher water flowrate, due to the decrease in the number of ions that are attracted to the pore and block water passage. For the 1.33nm diameter pore salt rejection is not at 100% and fluctuates around 70% for 100MPa. We also showed how regular MoS_2 (Q1) actually exists in the transition between two different ion transport regimes. One of them, characteristic of hydrophobic pores (Q0) where ions have a hard time entering the pore but once they do they leave it very quickly, and the other, observed in very hydrophilic pores (Q2), where ions are strongly attracted to the inside of the pores and remain there for long periods of time. In either case, whichever phenomenon dominates leads to an increase in salt rejection as it keeps salt ions from reaching the output reservoir of the reverse osmosis setup. In regular MoS_2 (Q1), however, the height of the potential energy barrier keeping ions from entering the pore and the coulombic attraction towards Mo atoms keeping them from exiting it combine in such a way that yields a reduced salt rejection. Results for water flux and salt rejection obtained in this work suggest that a more efficient nanopore may exist, with charge polarization between regular MoS_2 (Q1) and hydrophobic MoS_2 (Q0).

The concept of different TMD nanopores was also briefly explored by Yao et al. where they simulated nanopores with identical geometries and charge multipliers of Q1, Q0.9 and Q0.8 in the presence of salt for 0.97nm pores and showed a slight increase in water flow as the charge multiplier decreased [65] and an insignificant change in salt rejection. This result suggests that the performance of MoS_2 nanopores as desalination devices may be improved by manipulating the way charge is distributed across it, either by selecting different TMDs or by modifying them to induce different charge polarizations on the nanopores.

Figure 40 provides a comparison between the desalination performance of the nanopores simulated in this work and other nanopores simulated in literature. MoS_2 pores shown here were taken from [36, 37, 40, 65], graphene pores from [10, 36] and commercial polymeric seawater RO, brackish water RO and nanofiltration from [81]. The 0.97nm diameter pores simulated by us exhibit nearly identical performance to the one simulated by Abal et. al in [40, 63], where equal water, salt and MoS_2 force fields were utilized, as well as identical pore geometries. The result obtained by Yao et. al in [65] for the 0.97nm diameter pore are similar, with their pore not exhibiting 100% salt rejection but a slightly higher water flux. Such differences are likely caused by the different force fields utilized in both studies. Our hypothetical hydrophobic (Q0) 0.97nm diameter pore performs quite well, exhibiting higher water flux than its regular MoS_2 equivalent (Q1), while still maintaining 100% salt rejection. Mo-terminated MoS_2 nanopores studied by Aluru et al. perform the best among MoS_2 pores, wih the mixed termination MoS_2 pore from Farimani et al. [37] not too far behind.

The best performing nanopore in Figure 29 is the hydroxylated graphene nanopore reported by Grossman et. al [10]. Aluru et. al, however, also simulated graphene nanopores in their work [36] and reported a water flux 70% lower than for its Mo-terminated MoS_2 nanopore. They argue this different is caused by a discrepancy in the membrane porosities used in the simulations, indicating that Mo-terminated MoS_2 nanopores may be more efficient than graphene ones. Such distortions are common and should be taken into account when comparing results in literature.

Results for our 0.97nm diameter pores still outperform commercial RO desalination membranes by about two orders of magnitude, with increases up to 3 orders of magnitude being reported in literature. This is very encouraging and indicates that the application of 2D materials to water desalination is expected to bring massive reduction in energy consumption.

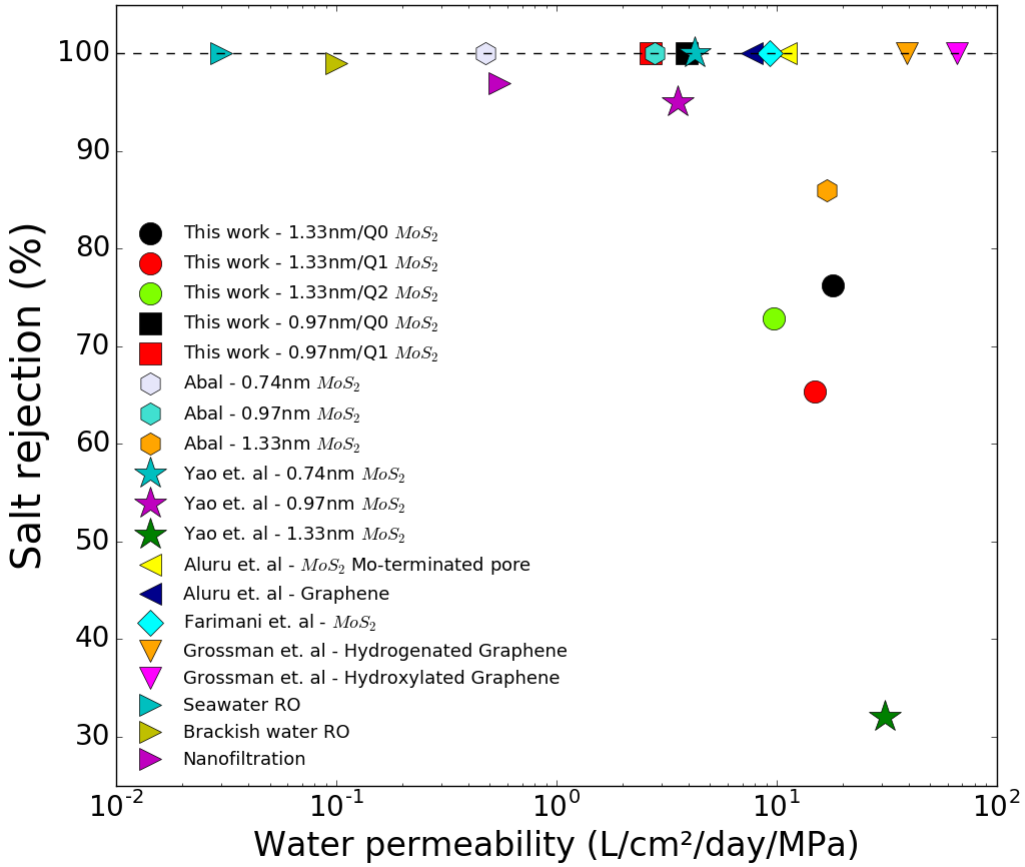

Figure 40: Performance of different desalination membranes, salt rejection is given as a percentage in the Y axis and water permeability in $L/cm^2/day/MPa$ in the X axis.

The larger nanopores studied by us in this work yield water fluxes about five times higher than for the smaller ones. Their application to desalination is, however, compromised by its lower salt rejection. There is, however, a way of getting around this issue, by introducing additional layers of MoS_2 to the membrane. If separated by distances larger than a few nanometers, this system will be governed by classical membrane theory and will lead to a 50% reduction in water flux. The second layer introduced will also significantly increase salt rejection, a membrane with salt rejection of 70% - which was observed for 1.33nm pores - will be expected to reject 91% of salt ions when a second layer is added [38]. This is still below the threshold for seawater desalination, but is high enough for other less demanding applications. A loss of half the water flux in the 1.33nm pore is still equivalent to an increase of $\sim$ 2.5 times in water flux, indicating that bilayer and multilayer desalination membranes are strong candidates for the next generation of RO membrane technology.

This motivated our study of bilayer MoS_2 membranes. While we were unable to carry out an analysis of ion transport across such membranes, we provided a detailed analysis on the mechanisms governing water transport across such structures. Our hope is that such membranes, containing 1.33nm diameter pores, may yield a high flux RO membrane with higher salt rejection than its monolayer version.

We considered membranes with very low layer separation (1.2nm), which are small enough to move into nano territory and make predictions from classical hydrodynamics inaccurate. The choice for such narrow spacing in the membrane was made in the hope that the nanochannel formed between both sheets acts as an additional nanopore and further increases ion exclusion, as it allows for a free spacing of roughly 0.9nm [27], which is smaller than the diameter of the hydration shell of salt ions. This layer spacing is also observed in nature for hydrated MoS_2 and was shown to be highly stable [27].

We showed that the reduction in water flux in bilayer MoS_2 nanoporous membranes was always higher than 50%, but that it was dependent on MoS_2's charge distribution and the alignment between the two nanopores. We showed how weak electrostatic interactions with the membrane's

inner walls in between MoS_2 layers determines the degree of anisotropy in the spatial configuration of water molecules. Hydrophobic MoS_2 exhibited a higher degree of organization of water molecules in the interlayer region, which led to higher spatial anisotropy of the hydrogen bond network in the direction perpendicular to MoS_2 sheets, which appears to slow down water flux. As charge polarization becomes present, this organization is slightly disturbed and water molecules are capable of forming more hydrogen bonds in directions not parallel to the MoS_2 sheets, leading to a more bulk-like water organization and higher water fluxes. This phenomenon was more pronounced in the highly hydrophilic MoS_2 membrane (Q2). This indicates a competition between MoS_2's geometry and charge distribution regulates water flux in bilayer MoS_2 membranes, on top or in-pore phenomena observed for single layer systems. Weak electrostatic interaction with the inner S layer of MoS_2 creates a more isotropic liquid in the interlayer region and allows for higher water flux due to the increased number of hydrogen bonds formed in directions not parallel to MoS_2 sheets. Increased charge polarizations were also shown increase isotropy in the distribution of water molecules in the XY plane. Oxygen atoms are usually accommodated at Mo-sites for Q0-MoS_2, however, as charge polarization grows, molecules move away from Mo-sites towards S-sites, leading to a smooth water density in the XY plane for Q2-MoS_2. We were, however, unable to relate this phenomenon to a mechanism regulating water transport, therefore it remains only as a correlation effect, not a cause for increased water flux brought by an increase in spatial isotropy of water density. Further analysis is necessary to confirm or discard this contribution.

The Q2 bilayer MoS_2 membrane exhibits lower bilayer flux loss than regular MoS_2 (Q1) in this case, indicating it leads to more efficient water transport in the interlayer region. As mentioned beforehand, charge polarization can be tuned by selecting a different TMD material for the membrane, with little changes to its geometry. While that is a potential source of improvement to water flow on bilayer MoS_2 membranes, there is no guarantee such materials will behave in the same way as MoS_2 when exposed to water or salt ions. In their work, Wanunu et al. produced multilayer nanoporous MoS_2 membranes using ultrasound-assisted exfoliation and probe sonication. They also covered the MoS_2 walls with cationic and anionic peptides, which altered the charge distribution if MoS_2 walls. This peptide decoration of the MoS_2 sheets led to a very high salt rejection, over 99%, and water flow [82]. Such system is a real life analog to the approach followed in this work of artificially tuning the strength of charge polarization in our simulations. The coating of the MoS_2 walls will certainly lead to changes in geometry, so this is not a perfect parallel, but our results provide clues for smarter design of bilayer MoS_2 membranes for water filtration.

Our results also indicate that increasing layer separation to values slightly above 1.2nm can greatly increase water transport, by making the interlayer water more bulk-like. Layer separation is something that can be tuned by intercalating nanoparticles in between sheets, as was demonstrated in literature [67, 68, 69, 70, 71]. This indicates that water flux across bilayer MoS_2 membranes can be increased by making the two MoS_2 layers further apart. Of course, it remains to be seen if such systems would be stable in water, otherwise their application to desalination would be compromised.

Our results also indicate that pore misalignement leads to a decrease in water transport across the membrane. Grossman et al. reported in their work that such a thing was not observed for bilayer graphene membranes used for water desalination. Their simulations suggest that despite changes in the way water flows across membranes when pores are aligned or heavily misaligned, this does not appear to alter its water flowrate, but it greatly increases salt rejction [38]. This may be caused by graphene's extremely low friction coefficient, and it could be that MoS_2 presents higher friction due to its rougher surface, this is however beyond the scope of this work.

The lack of results for ion transport across bilayer MoS_2 membranes makes our analysis rather incomplete. Different charge distributions and layer spacings will certainly impact the membranes salt rejection. Our analysis, nonetheless, provides an understanding on how water flows across such systems, and that may certainly be helpful when designing nanoporous MoS_2 membranes for desalination or other applications.

In conclusion, our results support previous findings in literature regarding the high performance of 2D materials and nanopores as powerful desalination devices. Our analysis provide a guide for the design of future RO membranes by elucidating some of the fundamental mechanisms behind water and salt transport. Further research, both experimental and theoretical/computational, is needed in order to make large scale fabrication of highly efficient 2D nanoporous membranes for water desalination a reality. Our current knowledge indicates that we may be very close to a revolution in this field, which should greatly increase humanity's access to clean drinking water.

6 References

[1] https://www.worldwildlife.org/threats/water scarcity. Wwf, water scarcity. 2020.

[2] E. HAMEETEMAN. Future water (in)security: Facts, figures, and predictions. *Global Water Institute*, 2013.

[3] UNESCO. The united nations world water development report. *United Nations Educational, Scientific and Cultural Organization*, 2016.

[4] Hosny K. Khordagui. *Desalination*, pages 124–125. Springer Netherlands, Dordrecht, 1999.

[5] Muhammad Qasim, Mohamed Badrelzaman, Noora N. Darwish, Naif A. Darwish, and Nidal Hilal. Reverse osmosis desalination: A state-of-the-art review. *Desalination*, 459:59–104, 2019.

[6] M.A.Al-Obaidi C.Kara-Zaitri I.M.Mujtaba. Scope and limitations of the irreversible thermodynamics and the solution diffusion models for the separation of binary and multi-component systems in reverse osmosis process. *Computer Chemical Engineering*, 100:48–79, 2017.

[7] Al-Zubaidy S. Vaclavikova M. et al Boretti, A. Outlook for graphene-based desalination membranes. *npj Clean Water*, 1:5, 2018.

[8] Guo dong Kang and Yi ming Cao. Development of antifouling reverse osmosis membranes for water treatment: A review. *Water Research*, 46(3):584–600, 2012.

[9] et. al Sumedh P. Surwade. Water desalination using nanoporous single-layer graphene. *Nature Nanotechnology*, 2015.

[10] David Cohen-Tanugi and Jeffrey C. Grossman. Water desalination across nanoporous graphene. *Nano Letters*, 2012.

[11] R Andrews B. J. Hinds M. Majumder, N. Chopra. Enhanced flow in carbon nanotubes. *Nature*, 2005.

[12] Y. M. Wang M. Stadermann A. B. Artyukhin C. P. Grigoropulos A. Noy J. K. Holt, H. G. Park and O. Bakajin. Fast mass transport through sub-2-nanometer carbon nanotubes. *Science*, 312(5776):1034–1037, 2006.

[13] L. Cagnon M. Whitby, M. T., and Nano-letters N. Quirke. Enhanced fluid flow through nanoscale carbon pipes. *Nano Letters*, 8(9):2632–2637, 2008.

[14] Y. Zhao S. Xie X. Qin, Q. Yuan and Z. Liu. Measurement of the rate of water translocation through carbon nanotubes. *Nano Letters*, 11(5):2173–2177, 2011.

[15] J. C. Rasaiah G. Hummer and J. P. Noworytra. Water conduction through the hydrophobic channel of a carbon nanotube. *Nature*, 414(6860):188–190, 2001.

[16] A. Diehl J. R. Bordin and M. C. Barbosa. Relation between flow enhancement factor and structure for core-softened fluids inside nanotubes. *J. Phys. Chem. B*, 117(23):7047–7056, 2013.

[17] A. Diehl J. R. Bordin, J. S. Andrade Jr. and M. C. Barbosa. Enhanced flow of core-softened fluids through narrow nanotubes. *J. Phys. Chem. B*, 140:7047–7056, 2014.

[18] Leo B.F. Murphy F. Das, R. The toxic truth about carbon nanotubes in water purification: a perspective view. *Nanoscale Res Lett*, 13:183, 2018.

[19] Arul Prakash Francis and Thiyagarajan Devasena. Toxicity of carbon nanotubes: A review. *Toxicology and Industrial Health*, 34(3):200–210, 2018. PMID: 29506458.

[20] Ihsanullah. Carbon nanotube membranes for water purification: Developments, challenges, and prospects for the future. *Separation and Purification Technology*, 209:307–337, 2019.

[21] Revathy Rajan. https://www.slideshare.net/revethyy/revathyyy. Accessed: 2022-02-01.

[22] Changgu Lee, Xiaoding Wei, Jeffrey W. Kysar, and James Hone. Measurement of the Elastic Properties and Intrinsic Strength of Monolayer Graphene. *Science*, 321(5887):385, July 2008.

[23] Ke Cao, Shizhe Feng, Ying Han, Libo Gao, Thuc Hue Ly, Zhiping Xu, and Yang Lu. Elastic straining of free-standing monolayer graphene. *Nature Communications*, 11:284, January 2020.

[24] A. K. Geim and K. S. Novoselov. The rise of graphene, 2007.

[25] Joseph Imbrogno, John J. Keating, James Kilduff, and Georges Belfort. Critical aspects of ro desalination: A combination strategy. *Desalination*, 401:68–87, 2017. 50th anniversary of Desalination.

[26] Philip C. H. Mitchell, Tim Outteridge, Ken Kloska, Steve McMahon, Yakov Epshteyn, Roger F. Sebenik (Retired), A. Richard Burkin (Retired), Robert R. Dorfler, John M. Laferty (Retired), Gerhard Leichtfried, Hartmut Meyer-Grünow, and Mark S. Vukasovich (deceased). *Molybdenum and Molybdenum Compounds*, pages 1–63. John Wiley Sons, Ltd, 2020.

[27] Zhongying Wang, Qingsong Tu, Sunxiang Zheng, Jeffrey J. Urban, Shaofan Li, and Baoxia Mi. Understanding the aqueous stability and filtration capability of mos2 membranes. *Nano Letters*, 17(12):7289–7298, 2017. PMID: 29160714.

[28] Pradeep Waduge, Ismail Bilgin, Joseph Larkin, Robert Y. Henley, Kenneth Goodfellow, Adam C. Graham, David C. Bell, Nick Vamivakas, Swastik Kar, and Meni Wanunu. Direct and scalable deposition of atomically thin low-noise mos2 membranes on apertures. *ACS Nano*, 9(7):7352–7359, 2015. PMID: 26111109.

[29] Nihit Saigal. Aspects of electronic structure of bulk and monolayer mos2studied using optical spectroscopy. Master's thesis, Tata Institute of Fundamental Research, 2016.

[30] https://www.ossila.com/pages/molybdenum-disulfide-mos2. Accessed: 2022-02-05.

[31] Simone Bertolazzi, Jacopo Brivio, and Andras Kis. Stretching and breaking of ultrathin mos2. *ACS Nano*, 5(12):9703–9709, 2011. PMID: 22087740.

[32] Qing Hua Wang, Kourosh Kalantar-Zadeh, Andras Kis, Jonathan N. Coleman, and Michael S. Strano. Electronics and optoelectronics of two-dimensional transition metal dichalcogenides. *Nature Nanotechnology*, 7(11):14. 699–712, 2012.

[33] Rudren Ganatra and Qing Zhang. Few-layer mos2: A promising layered semiconductor. *ACS Nano*, 8(5):4074–4099, 2014. PMID: 24660756.

[34] Kyaw Sint, Boyang Wang, and Petr Král. Selective ion passage through functionalized graphene nanopores. *Journal of the American Chemical Society*, 130(49):16448–16449, 2008. PMID: 19554715.

[35] Qing Tang, Zhen Zhou, and Zhongfang Chen. Graphene-related nanomaterials: tuning properties by functionalization. *Nanoscale*, 5:4541–4583, 2013.

[36] Farimani A. Aluru N. Heiranian, M. N. water desalination with a single-layer mos2 nanopore. *Nat Commun*, 6:8616, 2015.

[37] Zhonglin Cao, Vincent Liu, and Amir Barati Farimani. Why is single-layer mos2 a more energy efficient membrane for water desalination? *ACS Energy Letters*, 5(7):2217–2222, 2020.

[38] Li-Chiang Lin David Cohen-Tanugi and Jeffrey C. Grossman. Multilayer nanoporous graphene membranes for water desalination. *Nano letters*, 16:1027–1033, 2016.

[39] Zhongqiang Zhang, Fujian Zhang, Zhen Liu, Guanggui Cheng, Xiaodong Wang, and Jianning Ding. Molecular dynamics study on the reverse osmosis using multilayer porous graphene membranes. *Nanomaterials*, 8(10), 2018.

[40] J. P. K. Abal. Water desalination by mos2 nanoporous membrane: a molecular dynamics analysis. Master's thesis, UFRGS, 2020.

[41] Martin Chaplin. https://water.lsbu.ac.uk/water/water_anomalies.html. Accessed: 2022-02-03.

[42] Pettersson L. Nilsson, A. The structural origin of anomalous properties of liquid water. *Nat Commun*, 6:8998, 2015.

[43] Martin Chaplin. https://water.lsbu.ac.uk/water/water_hydrogen_bonding.htm. Accessed: 2022-02-03.

[44] Michael Evans. https://www.metallacycle.com/chemistry/aqueous-solutions/water-chemistry/. Accessed: 2022-02-01.

[45] Zhang Pan, Jing Chen, Gang Lü, Yi-Zhao Geng, Hui Zhang, and Qing Ji. An ab initio molecular dynamics study on hydrogen bonds between water molecules. *The Journal of Chemical Physics*, 136(16):164313, 2012.

[46] Daan Frenkel and Berend Smit. In *Understanding Molecular Simulation*. Academic Press, San Diego, second edition, 2002.

[47] Raúl Fuentes-Azcatl and Marcia C. Barbosa. Thermodynamic and dynamic anomalous behavior in the tip4p/ water model. *Physica A: Statistical Mechanics and its Applications*, 444:86–94, 2016.

[48] Raúl Fuentes-Azcatl and Marcia C. Barbosa. Sodium chloride, nacl/: New force field. *The Journal of Physical Chemistry B*, 120(9):2460–2470, 2016. PMID: 26890321.

[49] Eugene S. Kadantsev and Pawel Hawrylak. Electronic structure of a single mos2 monolayer. *Solid State Communications*, 152(10):909–913, 2012.

[50] Rasaiah J. Noworyta J. Hummer, G. Water conduction through the hydrophobic channel of a carbon nanotube. *Nature*, 414:188–190, 2001.

[51] Abdulnour Y. Toukmaji and John A. Board. Ewald summation techniques in perspective: a survey. *Computer Physics Communications*, 95(2):73–92, 1996.

[52] H. A. Lorentz. Ueber die anwendung des satzes vom virial in der kinetischen theorie der gase. *Annalen der Physik*, 248(1):127–136, 1881.

[53] Jean-Paul Ryckaert, Giovanni Ciccotti, and Herman J.C Berendsen. Numerical integration of the cartesian equations of motion of a system with constraints: molecular dynamics of n-alkanes. *Journal of Computational Physics*, 23(3):327–341, 1977.

[54] G. Ciccotti and J.P. Ryckaert. Molecular dynamics simulation of rigid molecules. *Computer Physics Reports*, 4(6):346–392, 1986.

[55] Frank J. Millero, Rainer Feistel, Daniel G. Wright, and Trevor J. McDougall. The composition of standard seawater and the definition of the reference-composition salinity scale. *Deep Sea Research Part I: Oceanographic Research Papers*, 55(1):50–72, 2008.

[56] Philippe Schwaller Davide Campi Andrius Merkys Antimo Marrazzo Thibault Sohier Ivano E. Castelli Andrea Cepellotti Giovanni Pizzi Nicola Marzari Nicolas Mounet, Marco Gibertini. Two-dimensional materials from high-throughput computational exfoliation of experimentally known compounds. *Materials Cloud Archive*, 2020.158, 2020.

[57] William Humphrey, Andrew Dalke, and Klaus Schulten. Vmd: Visual molecular dynamics. *Journal of Molecular Graphics*, 14(1):33–38, 1996.

[58] David Cohen-Tanugi and Jeffrey C. Grossman. Water permeability of nanoporous graphene at realistic pressures for reverse osmosis desalination. *The Journal of Chemical Physics*, 141(7):074704, 2014.

[59] *Gmelin Handbook of inorganic and organometallic chemistry. System number 59. Fe–Iron.* Springer-Verlag, Berlin ;, 8th ed. edition, 1929.

[60] H. H. Huang, Xiaofeng Fan, David J. Singh, Hong Chen, Q. Jiang, and W. T. Zheng. Controlling phase transition for single-layer mte2 (m = mo and w): modulation of the potential barrier under strain. *Phys. Chem. Chem. Phys.*, 18:4086–4094, 2016.

[61] João P. K. Abal, Rodrigo F. Dillenburg, Mateus H. Köhler, and Marcia C. Barbosa. Molecular dynamics simulations of water anchored in multilayered nanoporous mos2 membranes: Implications for desalination. *ACS Applied Nano Materials*, 4(10):10467–10476, 2021.

[62] João P. K. Abal and Marcia C. Barbosa. Water mobility in mos2 nanopores: effects of the dipole–dipole interaction on the physics of fluid transport. *Phys. Chem. Chem. Phys.*, 23:12075–12081, 2021.

[63] João P. K. Abal, José Rafael Bordin, and Marcia C. Barbosa. Salt parameterization can drastically affect the results from classical atomistic simulations of water desalination by mos2 nanopores. *Phys. Chem. Chem. Phys.*, 22:11053–11061, 2020.

[64] Weifeng Li, Yanmei Yang, Jeffrey K. Weber, Gang Zhang, and Ruhong Zhou. Tunable, strain-controlled nanoporous mos2 filter for water desalination. *ACS Nano*, 10(2):1829–1835, 2016. PMID: 26800095.

[65] Jianlong Kou, Jun Yao, Lili Wu, Xiaoyan Zhou, Hangjun Lu, Fengmin Wu, and Jintu Fan. Nanoporous two-dimensional mos2 membranes for fast saline solution purification. *Phys. Chem. Chem. Phys.*, 18:22210–22216, 2016.

[66] Mateus Henrique Köhler, José Rafael Bordin, and Marcia C. Barbosa. 2d nanoporous membrane for cation removal from water: Effects of ionic valence, membrane hydrophobicity, and pore size. *The Journal of Chemical Physics*, 148(22):222804, 2018.

[67] Huishuang Dong, Yang Xu, Chenglin Zhang, Yuhan Wu, Min Zhou, Long Liu, Yulian Dong, Qun Fu, Minghong Wu, and Yong Lei. Mos2 nanosheets with expanded interlayer spacing for enhanced sodium storage. *Inorg. Chem. Front.*, 5:3099–3105, 2018.

[68] Chengquan Chu, Cen-Feng Fu, Pengpeng Zhang, Ting Pan, Xinyu Ai, Yuying Wu, Peng Cui, Qiang Huang, and Jin Ran. Precise ångström controlling the interlayer channel of mos2 membranes by cation intercalation. *Journal of Membrane Science*, 615:118520, 2020.

[69] Jun Xu, Junjun Zhang, Wenjun Zhang, and Chun-Sing Lee. Interlayer nanoarchitectonics of two-dimensional transition-metal dichalcogenides nanosheets for energy storage and conversion applications. *Advanced Energy Materials*, 7(23):1700571, 2017.

[70] Ting Xiang, Qi Fang, Hui Xie, Chuanqiang Wu, Changda Wang, Yu Zhou, Daobin Liu, Shuangming Chen, Adnan Khalil, Shi Tao, Qin Liu, and Li Song. Vertical 1t-mos2 nanosheets with expanded interlayer spacing edged on a graphene frame for high rate lithium-ion batteries. *Nanoscale*, 9:6975–6983, 2017.

[71] Kelong Ai, Changping Ruan, Mengxia Shen, and Lehui Lu. Mos2 nanosheets with widened interlayer spacing for high-efficiency removal of mercury in aquatic systems. *Advanced Functional Materials*, 26(30):5542–5549, 2016.

[72] Steve Plimpton. Fast parallel algorithms for short-range molecular dynamics. *Journal of Computational Physics*, 117(1):1–19, 1995.

[73] Qingyin Zhang, Xin Wang, Jipeng Li, Sumin Lu, and Diannan Lu. How pressure affects confine water inside different nanoslits. *RSC Adv.*, 9:19086–19094, 2019.

[74] Jinfeng Liu, Xiao He, John Z. H. Zhang, and Lian-Wen Qi. Hydrogen-bond structure dynamics in bulk water: insights from ab initio simulations with coupled cluster theory. *Chem. Sci.*, 9:2065–2073, 2018.

[75] Kijeong Kwac, In Kim, Tod A. Pascal, William A. Goddard, Hyung Gyu Park, and Yousung Jung. Multilayer two-dimensional water structure confined in mos2. *The Journal of Physical Chemistry C*, 121(29):16021–16028, 2017.

[76] Amir Barati Farimani, Kyoungmin Min, and Narayana R. Aluru. Dna base detection using a single-layer mos2. *ACS Nano*, 8(8):7914–7922, 2014. PMID: 25007098.

[77] Kedi Yin, Shengxi Huang, Xiaofei Chen, Xinwei Wang, Jing Kong, Yan Chen, and Jianming Xue. Generating sub-nanometer pores in single-layer mos2 by heavy-ion bombardment for gas separation: A theoretical perspective. *ACS Applied Materials & Interfaces*, 10(34):28909–28917, 2018. PMID: 30062872.

[78] Jia-Wei Shen, Jiachen Li, Fei Liu, Li Zhang, Lijun Liang, Hongbo Wang, and Jian-Yang Wu. A molecular dynamics study on water desalination using single-layer mose2 nanopore. *Journal of Membrane Science*, 595:117611, 2020.

[79] Pan Jia, Qi Wen, Dan Liu, Min Zhou, Xiaoyan Jin, Liping Ding, Huanli Dong, Diannan Lu, Lei Jiang, and Wei Guo. Highly efficient ionic photocurrent generation through ws2-based 2d nanofluidic channels. *Small*, 15(50):1905355.

[80] Jiao-Jiao Han, Qiu-Yue Zhang, Min-Yue Huang, Yan Chen, Xi Yan, and Wan-Zhong Lang. Two-dimensional ws2 membranes constructed on different substrates for efficient dye desalination. *Desalination*, 480:114380, 2020.

[81] Greg Guillen and Eric M.V. Hoek. Modeling the impacts of feed spacer geometry on reverse osmosis and nanofiltration processes. *Chemical Engineering Journal*, 149(1):221–231, 2009.

[82] Liang W. VahidMohammadi A. et al. Sapkota, B. High permeability sub-nanometre sieve composite mos2 membranes. *Nature communications*, 11:247, 2020.